Next-to-Leading Order QCD Corrections to Vector Boson Pair Production in Association with two Jets at the LHC

Zur Erlangung des akademischen Grades eines

DOKTORS DER NATURWISSENSCHAFTEN

von der Fakultät für Physik des

Karlsruher Instituts für Technologie (KIT)

genehmigte

DISSERTATION

von

Dipl.-Phys. Matthias Kerner

aus Landau in der Pfalz

Tag der mündlichen Prüfung: 18. Juli 2014

Referent: Prof. Dr. Dieter Zeppenfeld

Korreferent: Prof. Dr. Matthias Steinhauser

Abstract

Pair production of electroweak (EW) vector bosons in association with two jets constitutes an important set of processes at the CERN Large Hadron Collider. Besides their contribution as a background to various searches for physics beyond the Standard Model, these processes allow one to probe the mechanism of EW symmetry breaking, since they include vector boson scattering and they are sensitive to triple and quartic gauge couplings.
In this thesis, the QCD-induced contributions to $W^{\pm}W^{\pm}jj$, $W^{\pm}Zjj$, $W^{\pm}\gamma jj$ and $ZZjj$ production are studied. The next-to-leading order (NLO) QCD corrections to the production cross sections, including leptonic decays of the massive vector bosons, have been implemented into the flexible Monte Carlo program VBFNLO. The corrections lead to a significant reduction of the scale uncertainty and show a non-trivial phase space dependence: While in most phase space regions, corrections of 10-20% are obtained, they can reach up to a factor of two if the separation or the invariant mass of the two tagging jets is large. This phase space region is of particular interest for studying vector boson scattering. Using different choices for the factorization and renormalization scales, we show that these large corrections are due to the large scale uncertainty of the leading order results. The effect of the NLO corrections on various differential cross sections is discussed in detail.

Zusammenfassung

Paarproduktion elektroschwacher Eichbosonen in Assoziation mit zwei Jets bildet eine wichtige Klasse von Prozessen für die Experimente am Large Hadron Collider am CERN. Neben ihrem Beitrag als Untergrund bei der Suche nach Physik jenseits des Standardmodells lässt sich mit diesen Prozessen der Mechanismus der elektroschwachen Symmetriebrechung untersuchen, da sie sowohl Vektorboson-Streuung als auch Dreier- und Viererkopplungen der elektroschwachen Eichbosonen beinhalten.
In dieser Arbeit werden die QCD-induzierten Beiträge zur Produktion von $W^{\pm}W^{\pm}jj$, $W^{\pm}Zjj$, $W^{\pm}\gamma jj$ und $ZZjj$ untersucht. Diese wurden in nächst-führenden Ordnung in QCD in das flexible Monte Carlo Programm VBFNLO implementiert, wobei leptonische Zerfälle der massiven Eichbosonen berücksichtigt wurden. Die Korrekturen führen zu einer signifikanten Reduktion der Skalenunsicherheit und weisen eine nicht-triviale Abhängigkeit vom Phasenraum auf: Während die Korrekturen in den meisten Phasenraumbereichen geringer als 20% sind, können diese bei großer Separation oder hoher invarianter Masse der Jets auf bis zu einen Faktor zwei anwachsen. Für das Studium der Vektorboson-Streuung ist diese Phasenraumregion von besonderem Interesse. Wir zeigen, dass die großen Korrekturen auf die große Skalenunsicherheit der führenden Ordnung zurückzuführen sind, indem die Wirkungsquerschnitte für verschiedene Wahlen der Renormierungs- und Faktorisierungsskala berechnet werden. Die Effekte der nächst-führenden Ordnung auf verschiedene differentielle Verteilungen werden ausführlich untersucht.

Contents

CHAPTER 1

Introduction

In July 2012, the experiments ATLAS and CMS at the CERN Large Hadron Collider (LHC) reported the discovery of a new boson with a mass of about 126 GeV [1, 2]. Its spin is different from one [3–5] and the production and decay rates resemble the properties of the Standard Model (SM) Higgs boson. If the SM hypothesis is confirmed in the next round of data taken at the LHC, this discovery would add another milestone to a long path of success representing the SM. Except for gravitation, all known interactions between the fundamental particles are described by this model. The strong interaction of quarks and gluons is described by Quantum Chromodynamics (QCD) [6–8], which exhibits the two characteristic features of confinement and asymptotic freedom. As a consequence, the quarks and gluons become weakly interacting at high energies, allowing for perturbative calculations, while in the low energy regime, a large spectrum of hadrons arises, which are bound states of these. The electromagnetic and weak interactions are included in the Glashow-Weinberg-Salam theory [9–11], giving rise to the electroweak (EW) sector of the SM. Via the Higgs mechanism [12–14], the EW symmetry is spontaneously broken, which allows one to consistently introduce mass terms to fermions and weak bosons. Besides the discoveries of the W and Z bosons [15, 16] as well as of the top quark [17], which have been predicted by the SM, further milestones along the path of success of the SM are, e.g., the excellent agreement of the magnetic moment of the electron with its theoretical prediction [18], or the prediction of the rare decay $B_s^0 \to \mu^+\mu^-$ [19].

Despite the great success of the SM, it cannot explain all phenomena observed in nature. The gravitational force is described by general relativity, which leads to conceptual problems because at energies close to the Planck scale of $\mathcal{O}(10^{19}\,\text{GeV})$, a unified description of quantum theory and gravity is required. In addition, there exist some observations that cannot be explained within the SM or general relativity: The observed rotational velocity of galaxies indicates the existence of dark matter which, besides its influence on the gravitational force, has not shown any interactions with the SM particles, yet. Also the abundance of matter compared to antimatter in the universe cannot be accounted for by the CP violating mechanism existing in the SM. Furthermore, the SM does not provide a satisfactory explanation for the large differences in the masses of the elementary particles. Hence, at some point the path of the SM will fork, opening up a way for a new theory. A first hint towards physics beyond the Standard Model (BSM) might appear in the self interactions of the EW gauge bosons, which in the SM are determined by the gauge group and the mechanism of EW symmetry breaking.

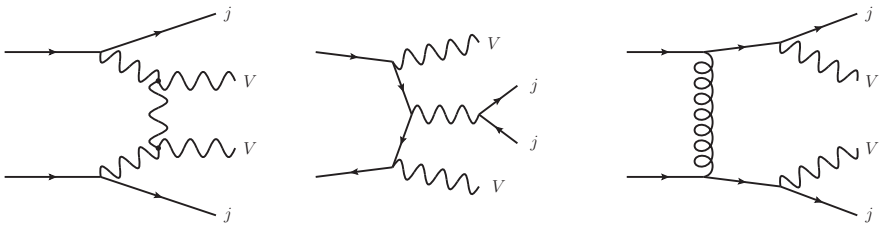

Figure 1.1.: Feynman diagrams representing the three mechanisms for production of electroweak vector boson pairs in association with two jets.

At the LHC, these self interactions can be studied in the production of EW vector boson pairs in association with two jets. These processes not only allow one to scrutinize the mechanism of electroweak symmetry breaking, but they also serve as a background in various searches for BSM physics.
$VVjj$ production can be classified into three contributions as illustrated in Fig. 1.1: The first and second diagram represent EW contributions of $\mathcal{O}(\alpha^4)$, which can be further classified into vector boson fusion (VBF) and triboson production with one vector boson decaying hadronically. Since these contributions include triple and quartic gauge couplings, they can be used to probe the structure of the EW sector of the standard model. In particular, the VBF contributions are of high interest, since they produce characteristic detector signals with relatively small backgrounds and they are sensitive to vector boson scattering, which in the SM is unitarized by contributions of the Higgs boson. First experimental evidence for the EW production of $W^{\pm}W^{\pm}jj$ via VBF has recently been reported [20], showing that the experimental study of vector boson scattering just started. The QCD-induced contributions of $\mathcal{O}(\alpha_s^2\alpha^2)$, which are the subject of this thesis, are represented by the third diagram. In addition to the contribution shown in Fig. 1.1, with a gluon being exchanged between two quark lines, there are additional subprocesses with external gluons attached to one quark line. Due to the appearance of gluon-induced subprocesses and the larger value of α_s compared to α, the QCD-induced processes typically have larger cross sections than the EW ones and lead to softer events.

Studying $VVjj$ production not only requires precise measurements, but also precise theoretical predictions of the cross sections – for the EW processes as well as for the QCD-induced backgrounds – and the calculation of the next-to-leading order (NLO) QCD corrections to these processes is mandatory. Therefore, these procesees have been listed in the NLO wishlist [21], formulated at the Les Houches workshop in 2005. While the NLO QCD corrections to the EW contributions have been known for a few years [22–40], NLO calculations of the more challenging QCD-induced contributions have become available only recently [41–51]. They involve virtual corrections with up to hexagon one-loop integrals of rank five, which are not only computing intensive, but their numerical evaluation can also lead to instabilities. Furthermore, the cross section calculation requires the evaluation of many subprocesses, each consisting of a large number of Feynman diagrams.

Many NLO calculations of similar complexity heavily rely on automated tools for the generation of the virtual amplitudes (see e.g. [52–54]) and for performing the phase space integration (see e.g. [54, 55]), and they typically require the use of a computer cluster. In this work, a different approach is chosen, aiming for a fast and numerically stable implementation of the considered processes. The QCD-induced contributions to $W^{\pm}W^{\pm}jj$, $W^{\pm}Zjj$, $W^{\pm}\gamma jj$ and $ZZjj$ production are implemented at NLO QCD into the flexible Monte Carlo program VBFNLO [56–58], including full leptonic decays of the massive vector bosons. We explicitly exploit the specific features of the individual processes to obtain a highly optimized program, allowing for cross section calculations within a few hours on a single computer core.

This thesis is organized as follows: Chapter 2 gives a brief introduction to the SM and presents the basic principles for calculating cross sections in hadron-hadron collisions with NLO accuracy. Chapter 3 is devoted to the implementation of QCD-induced $VVjj$ production into the Monte Carlo program VBFNLO. The implementation of the amplitudes and the subtraction terms, needed to handle infrared singularities, is described in detail. In addition, checks that have been used to validate the implementation are presented and the performance of the program is shown. In Chapter 4, the phenomenology of the processes is discussed. The scale dependence of the leading order (LO) and NLO cross sections for various choices of the factorization- and renormalization-scale is given and the effect of the NLO corrections on differential distributions is described in detail. Finally, Chapter 5 summarizes the work presented here.

CHAPTER 2

Theoretical Foundations

2.1. The Standard Model

In this section, a brief introduction to the Standard Model of particle physics is presented, which is a relativistic quantum field theory based on the gauge symmetry group $SU(3)_C \times SU(2)_L \times U(1)_Y$. Quantum chromodynamics [6–8], which describes the strong interactions between quarks and gluons, is determined by the group $SU(3)_C$. The electroweak interactions are given by the $SU(2)_L \times U(1)_Y$ symmetry of the Glashow-Weinberg-Salam theory [9–11], which is spontaneously broken via the Higgs mechanism [12–14]. The SM therefore allows to describe all known fundamental interactions of particles, except for the gravitational force. Detailed discussions of the SM are found in many textbooks about quantum field theory (see e.g. [59–61]).

Electroweak sector

The fermions of the SM can be classified into quarks and leptons, which are grouped into three generations as shown in Table 2.1. While the left-handed fermions form doublets, transforming under the fundamental representation of the $SU(2)_L$ group, the right-handed ones are singlets. The quantum numbers related to the gauge group $SU(2)_L \times U(1)_Y$ are the weak isospin T^3 and the hypercharge Y. From these, the electric charge Q is given by

$$Q = T^3 + \frac{Y}{2}. \tag{2.1}$$

To obtain local gauge invariance, the introduction of the four vector fields W^i_μ and B_μ is required, which transform under the adjoint representation of the corresponding symmetry group. The interactions of these gauge fields with the fermions is described by the Lagrangian

$$\mathcal{L}_{EW} = \sum_{i \in \text{fermions}} \overline{\Psi}_i i \not{D} \Psi_i - \frac{1}{4} W^a_{\mu\nu} W^{a,\mu\nu} - \frac{1}{4} B_{\mu\nu} B^{\mu\nu}, \tag{2.2}$$

with

$$W^a_{\mu\nu} = \partial_\mu W^a_\nu - \partial_\nu W^a_\mu - g_2 \epsilon^{abc} W^b_\mu W^c_\nu, \tag{2.3}$$

$$B_{\mu\nu} = \partial_\mu B_\nu - \partial_\nu B_\mu. \tag{2.4}$$

				T^3	Y	Q
quarks	$\begin{pmatrix} u \\ d \end{pmatrix}_L$	$\begin{pmatrix} c \\ s \end{pmatrix}_L$	$\begin{pmatrix} t \\ b \end{pmatrix}_L$	$+1/2$ $-1/2$	$+1/3$	$+2/3$ $-1/3$
	u_R	c_R	t_R	0	$+4/3$	$+2/3$
	d_R	s_R	b_R	0	$-2/3$	$-1/3$
leptons	$\begin{pmatrix} \nu_e \\ e^- \end{pmatrix}_L$	$\begin{pmatrix} \nu_\mu \\ \mu^- \end{pmatrix}_L$	$\begin{pmatrix} \nu_\tau \\ \tau \end{pmatrix}_L$	$+1/2$ $-1/2$	-1	0 -1
	e_R^-	μ_R^-	τ_R^-	0	-2	-1

Table 2.1.: Fermions of the Standard Model and their quantum numbers related to the gauge group $SU(2)_L \times U(1)_Y$.

and the covariant derivative

$$D_\mu = \partial_\mu + ig_2 W_\mu^a T^a + ig_1 B_\mu \frac{Y}{2}. \tag{2.5}$$

The generators of the weak isospin are $T^a = \frac{\sigma^a}{2}$ if they act on the doublet fields of the left handed fermions, while they are $T^a = 0$ when acting on right-handed fermions. g_2 and g_1 are the coupling constants corresponding to the gauge groups $SU(2)_L$ and $U(1)_Y$, respectively.

So far, all particles appearing in the Lagrangian of Eq. (2.2) are massless and the introduction of mass terms of the form

$$-m_f \overline{\Psi}\Psi = -m_f \left(\overline{\Psi}_L \Psi_R + \overline{\Psi}_R \Psi_L\right) \tag{2.6}$$

or $\frac{1}{2}M_V^2 V_\mu V^\mu$ would explicitly break gauge invariance, since these terms are not invariant under $SU(2)_L$ transformations. In the SM, the masses are generated via the Higgs mechanism, which introduces a $SU(2)_L$ doublet of complex scalar fields

$$\Phi = \begin{pmatrix} \phi^+ \\ \phi^0 \end{pmatrix} \tag{2.7}$$

with hypercharge $Y = 1$. The Lagrangian of this doublet field reads

$$\mathcal{L}_H = D_\mu \Phi^\dagger D^\mu \Phi \underbrace{+\mu^2 \Phi^\dagger \Phi - \lambda (\Phi^\dagger \Phi)^2}_{-V(\Phi^\dagger \Phi)}. \tag{2.8}$$

For $\mu, \lambda > 0$, the potential $V(\Phi^\dagger\Phi)$ has the shape of a mexican hat and features a minimum at $\langle \Phi^\dagger \Phi \rangle = \frac{\mu^2}{2\lambda} = v^2$. Due to the non-zero vacuum expectation value and the $SU(2)_L$ symmetry of the Lagrangian, the ground state is not unique and by selecting one of these, the gauge symmetry is spontaneously broken. The doublet Φ can then be parameterized by an expansion around the vacuum expectation value. In this parameterization, only one physical field, the Higgs field H, is obtained, while the other three degrees of freedom vanish, if the unitary gauge with

$$\Phi = \frac{1}{\sqrt{2}} \begin{pmatrix} 0 \\ v + H \end{pmatrix} \tag{2.9}$$

is used. The kinetic term of Eq. (2.8) includes the contribution

$$\Delta\mathcal{L} = \frac{1}{2} \begin{pmatrix} 0 & v \end{pmatrix} \left(g_2 W_\mu^a \frac{\sigma^a}{2} + \frac{1}{2} g_1 B_\mu \right) \left(g_2 W^{\mu b} \frac{\sigma^b}{2} + \frac{1}{2} g_1 B^\mu \right) \begin{pmatrix} 0 \\ v \end{pmatrix} \tag{2.10}$$

$$= \frac{1}{2} M_W^2 (W_\mu^- W^{+\mu} + W_\mu^+ W^{-\mu}) + \frac{1}{2} M_Z^2 Z_\mu Z^\mu, \tag{2.11}$$

which are the mass terms of the physical fields

$$W_\mu^\pm = \frac{1}{\sqrt{2}} \left(W_\mu^1 \mp i W_\mu^2 \right), \tag{2.12}$$

$$Z_\mu = \frac{1}{\sqrt{g_1^2 + g_2^2}} \left(g_2 W_\mu^3 - g_1 B_\mu \right), \tag{2.13}$$

$$A_\mu = \frac{1}{\sqrt{g_1^2 + g_2^2}} \left(g_1 W_\mu^3 + g_2 B_\mu \right) \tag{2.14}$$

with masses

$$M_W = g_2 \frac{v}{2}, \qquad M_Z = \sqrt{g_1^2 + g_2^2}\, \frac{v}{2} \qquad \text{and} \qquad M_A = 0. \tag{2.15}$$

Hence, the Higgs mechanism generates masses of the weak bosons $W^\pm$ and Z, while the photon remains massless. It also allows the introduction of fermion masses via Yukawa couplings of the fermions with the Higgs doublet. The corresponding Lagrangian reads

$$\mathcal{L}_{m_f} = \sum_{i,j \in \text{generations}} -\lambda_l^{ij}\, \overline{L}^i\, \Phi\, e_R^j - \lambda_d^{ij}\, \overline{Q}^i\, \Phi\, d^j - \lambda_u^{ij}\, \overline{Q}^i i\sigma^2 \Phi^* u^j + h.c., \tag{2.16}$$

where Q and L represent the quark and lepton doublets, respectively. The matrices λ can be diagonalized to obtain the mass eigenstates of the fermions.

Quantum chromodynamics

The fermions of the SM also have specific transformation properties according to the color group $SU(3)_C$. While the leptons are singlets and do not contribute to the strong interaction, each quark comes as a triplet with three different color charges. The gauge interactions are mediated by the eight gluon fields G_μ^a. Using an R_ξ gauge, the QCD Lagrangian reads

$$\mathcal{L}_{QCD} = \sum_q \overline{q}(i\not{D} - m_q)q - \frac{1}{4} G_{\mu\nu}^a G^{a,\mu\nu} + \frac{1}{2\xi} \left(\partial_\mu G^\mu \right)^2 - \overline{c}^a \partial^\mu D_\mu^{ab} c^b \tag{2.17}$$

with

$$D_\mu = \partial_\mu + i g_s G_\mu^a t^a, \tag{2.18}$$

$$G_{\mu\nu}^a = \partial_\mu G_\nu^a - \partial_\nu G_\mu^a - g_s f^{abc} G_\mu^b G_\nu^c. \tag{2.19}$$

Hence, the strong interactions are determined by the strong coupling constant g_s, as well as the generators t^a of the fundamental representation and the structure constants f^{abc}, which are related by

$$[t^a, t^b] = i f^{abc} t^c. \tag{2.20}$$

Important constants for QCD calculations are the quadratic Casimir invariants $C_F = \frac{4}{3}$ and $C_A = 3$ of the fundamental and adjoint representation, respectively, as well as the Dynkin index $T_R = \frac{1}{2}$, which are defined by

$$t^a t^a = C_F\, \mathbb{1}, \qquad f^{acd} f^{bcd} = C_A\, \delta^{ab}, \qquad \text{Tr}(t^a t^b) = T_R \delta^{ab}. \tag{2.21}$$

The last term of Eq. (2.17) contains the anticommuting ghost fields that are needed to remove the two unphysical degrees of freedom of the gluon field.
In Section 2.2.3, it will be discussed that the non-abelian structure of the QCD interactions leads to asymptotic freedom and confinement of the quarks and gluons.

2.2. Cross Sections at Next-to-Leading Order in α_s

2.2.1. Perturbative Expansion

The theoretical tool to obtain cross section predictions for collider experiments is perturbation theory, improved by the application of renormalization group equations. At hadron colliders, the parton model is used to describe the collisions of the hadrons as a scattering of quarks and gluons, which carry a fraction x_i of the hadron momenta P_i. Using the factorization theorem (see e.g. Ref. [62]), the cross section for the collision of two hadrons H_i producing a final state observable X can be written in terms of parton-parton interactions as

$$\sigma(H_1\,H_2 \to X) = \sum_{a,b} \int_0^1 \mathrm{d}x_a \mathrm{d}x_b\, f_{a/H_1}(x_a, \mu_F^2) f_{b/H_2}(x_b, \mu_F^2)\, \sigma_{ab}(ab \to X; \mu_F^2), \tag{2.22}$$

where μ_F is called factorization scale. The process-independent parton distribution functions (pdfs) f have to be determined experimentally since the particle content of the hadrons cannot be described perturbatively. At leading order (LO), they can be interpreted as probability densities for finding a parton i with momentum fraction x_i in the hadron. When considering higher order corrections, this interpretation does not hold since collinear radiations off the partons a and b lead to a more involved convolution of the hard process σ_{ab} with the pdfs. These initial state splittings involve logarithmic contributions $\alpha_s^n \ln^n(\mu_F^2/m_{ij}^2)$ of the invariant parton masses m_{ij} appearing in the hard process and the factorization scale μ_F, that has been introduced in the above equation. To avoid large contributions of these logarithms, which can spoil the convergence of the perturbative expansion, a characteristic energy scale of the hard process should be used as factorization scale. The corresponding shifts of the factorization scale from μ_F to a scale μ_F' lead to the logarithms $\alpha_s^n \ln^n(\mu_F'^2/\mu_F^2)$, which can be resummed to all orders in α_s into the parton distribution functions. This introduces a μ_F dependence of the pdfs, which is determined by the Dokshitzer-Gribov-Lipatov-Altarelli-Parisi (DGLAP) equations [63–65]. Since the cross section cannot depend on the, in principle, arbitrary scale μ_F, the dependence of a fixed order calculation on this parameter can be used to estimate the size of the neglected higher order terms.

In general, the final state observable X does not determine a specific final state configuration with a fixed number of particles. In particular, it must not depend on soft or collinear parton radiation. Such splittings cannot be resolved experimentally and lead to the appearance of divergences in the cross section calculation. According to the Kinoshita-Lee-Nauenberg (KLN) theorem [66, 67], those divergences cancel for sufficiently inclusive observables X after the inclusion of various final state multiplicities. Including the integration over the phase space for n final state particles, represented by $\mathrm{d}\Phi_n$, the partonic cross section can therefore be written as

$$\sigma_{ab}(ab \to X) = \frac{1}{4p_a p_b} \sum_n \sum_{\{f_n\}} \int \mathrm{d}\Phi_n(p_a, p_b; p_{f_1}, \ldots, p_{f_n}) \mathrm{d}\sigma_{ab}(ab \to f_1 \ldots f_n) \cdot F_n(X; \{f_n\}), \tag{2.23}$$

where $F_n(X, \{f_n\})$ includes a jet definition function, as well as phase space cuts which specify if the final state matches the observable X. For the KLN theorem to hold, the observable X has to be infrared-safe, meaning that for any parton pair i, j, one obtains

$$F_n(X; p_{f_1}, \ldots, p_{f_i}, \ldots, p_{f_j}, \ldots, p_{f_n}) \xrightarrow{p_i \cdot p_j \to 0} F_{n-1}(X; p_{f_1}, \ldots, p_{f_i} + p_{f_j}, \ldots, p_{f_n}). \tag{2.24}$$

The partonic subprocesses, $\mathrm{d}\sigma_{ab}$, are given by the corresponding scattering amplitudes and can be calculated perturbatively.

At LO, Eq. (2.22) can be written as

$$\sigma^{LO} = \sum_{a,b} \int_0^1 \mathrm{d}x_a \mathrm{d}x_b \, f_a^{LO}(x_a, \mu_F^2) f_b^{LO}(x_b, \mu_F^2) \, \sigma_{ab}^B, \tag{2.25}$$

where σ^B is given by the Born-level contribution to the amplitude. The corresponding next-to-leading order (NLO) cross section reads

$$\sigma^{NLO} = \sum_{a,b} \int_0^1 \mathrm{d}x_a \mathrm{d}x_b \, f_a^{NLO}(x_a, \mu_F^2) f_b^{NLO}(x_b, \mu_F^2) \, \left[\sigma^B + \sigma^V + \sigma^R + \sigma^C\right]_{ab}. \tag{2.26}$$

The virtual corrections σ^V contain the interferences of the one-loop diagrams with the Born contribution, $\mathrm{d}\sigma^V = 2\,\mathrm{Re}(\mathcal{M}^*_{1-\mathrm{loop}} \cdot \mathcal{M}_B)$. The real emission $\mathrm{d}\sigma^R$ includes all tree-level processes with an additional parton in the final state. In contrast to the other contributions, it therefore has to be integrated over the phase space of $n+1$ particles. The collinear counter term $\mathrm{d}\sigma^C$, acting as a pdf counter term, absorbs the remaining divergences of collinear initial state parton splittings from $(\sigma^V + \sigma^R)$.

2.2.2. Infrared Singularities and Dipole Subtraction

While the KLN theorem guarantees finite results for the total cross section, the individual contributions on the right hand side of Eq. (2.26), with exception of σ^B, are divergent. Besides the ultraviolet (UV) singularities, appearing in the calculation of σ^V and discussed in Section 2.2.3, the contributions involve infrared (IR) divergences, stemming from soft or collinear parton splittings.

The common procedure to handle these divergences is dimensional regularization, where the phase space integration over the four-dimensional momenta is replaced by a $d = 4 - 2\varepsilon$ dimensional integration,

$$\int \mathrm{d}^4 p \quad \longrightarrow \quad \mu^{2\varepsilon} \int \mathrm{d}^d p. \tag{2.27}$$

Here, an arbitrary mass parameter μ has been introduced to keep the overall mass dimension of the results. The divergences then manifest as poles in ε and the limit $d \to 4$ has to be applied after those poles cancel in the sum of all contributions.

This regularization procedure, however, leads to technical difficulties, since the d-dimensional integrals cannot be calculated using Monte Carlo techniques. A method to overcome these difficulties is the use of subtraction algorithms: Since the divergent parts of the individual contributions in Eq. (2.26) factorize in the IR limit and are proportional to the Born-level contribution, the cross section can be written as [68]

$$\sigma^{NLO} = \sigma^B + \int_{n+1} \left[\left(\mathrm{d}\sigma^R\right)_{\varepsilon=0} - \left(\mathrm{d}\sigma^A\right)_{\varepsilon=0}\right] + \int_n \left[\mathrm{d}\sigma^V + \mathrm{d}\sigma^C + \int_1 \mathrm{d}\sigma^A\right]_{\varepsilon=0}. \tag{2.28}$$

The subtraction term $\mathrm{d}\sigma^A$ has to be chosen such that it approaches the contribution $\mathrm{d}\sigma^R$ in the phase space regions with soft or collinear parton splittings. Furthermore, it has to be partly* analytically integrable over the phase space of the additional parton emission. This integration leads to a contribution proportional to the Born-level matrix elements and contains poles in ε that exactly cancel the poles appearing in $\mathrm{d}\sigma^V$ and $\mathrm{d}\sigma^C$. After that, the limit $\varepsilon \to 0$ can be applied and the phase space integrals in Eq. (2.28) over the n and $n+1$ final state particles can be evaluated separately in four space-time dimensions using Monte Carlo integration.

*d-independent integrations, such as the x integration of dipoles [68] involving initial state particles, can be done numerically.

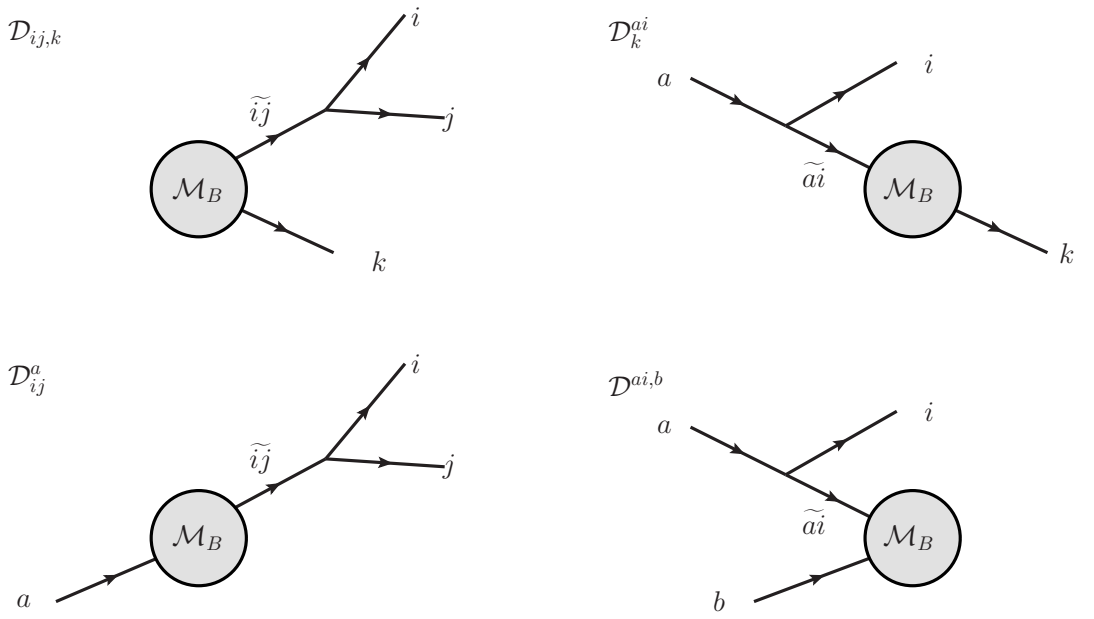

Figure 2.1.: Classification of the dipoles according to the position of the emitter pair and the spectator parton. The momentum flow is indicated by the arrows.

Catani-Seymour Dipole Subtraction

In this thesis, the Catani-Seymour dipole subtraction [68] algorithm is used and will be explained in the following. Within this algorithm, the subtraction term is constructed as a sum of dipoles[†]

$$\mathrm{d}\sigma^A = \sum_{\substack{\text{pairs}\\ i,j}} \left(\sum_{k\neq i,j} \mathcal{D}_{ij,k} + \sum_a \mathcal{D}_{ij}^a \right) + \sum_{\substack{\text{pairs}\\ a,i}} \left(\sum_{k\neq i} \mathcal{D}_k^{ai} + \sum_{b\neq a} \mathcal{D}^{ai,b} \right), \tag{2.29}$$

where for each emitter pair i, j or a, i, the corresponding term in the brackets reproduces the singular behavior of $\mathrm{d}\sigma^R$ in the limit $p_i \cdot p_j \to 0$ or $p_a \cdot p_i \to 0$, respectively. The dipoles appearing in the first bracket therefore describe soft and collinear final-state splittings, whereas the contributions in the second bracket include all initial-state singularities.

Each dipole can symbolically be written as

$$\mathcal{D} = \mathbf{V} \otimes |\mathcal{M}_B|^2, \tag{2.30}$$

where the operator $\mathbf{V}$ acts on the spin and color indices of the corresponding Born-level process, which is obtained by combining the emitter pair to one parent parton. The kinematics of the Born-level process are obtained from the full real-emission kinematics by combining the momenta of the emitter particles and shifting a part of this momentum to another parton, which is called the spectator parton, to fulfill the on-shell condition of all partons. Since the spectator parton can either be in the initial or in the final state of the process, one obtains a further classification of the dipoles as illustrated by Fig. 2.1.

The dipole formulas for the various configurations can be found in Ref. [68]. In the following, the dipoles will be explained taking the dipoles for final state splittings with final

[†]Following the notation of Ref. [68], the indices i, j and k correspond to final state partons, whereas the partons a and b are in the initial state. The sum $\sum_{b\neq a}$ therefore only includes one dipole term.

state spectator, $\mathcal{D}_{ij,k}$, as an example. These dipoles can be written as

$$\mathcal{D}_{ij,k} = -\frac{1}{2p_i \cdot p_j} \cdot \langle \widetilde{ij}, \widetilde{k}, \dots | \frac{\mathbf{T}_{ij}\mathbf{T}_k}{\mathbf{T}_{ij}^2} \mathbf{V}_{ij,k} | \widetilde{ij}, \widetilde{k}, \dots \rangle, \tag{2.31}$$

where the bra-ket notation is used to represent the Born-level matrix element and its complex conjugate of the underlying process. The momenta of the emitter parton $\widetilde{ij}$ and of the spectator $\widetilde{k}$ are given by [68]

$$\widetilde{p}_{ij}^{\,\mu} = p_i + p_j - \frac{1}{1-y_{ij,k}}\, p_k^\mu \qquad \text{and} \qquad \widetilde{p}_k^{\,\mu} = \frac{1}{1-y_{ij,k}}\, p_k^\mu, \tag{2.32}$$

with

$$y_{ij,k} = \frac{p_i p_j}{p_i p_j + p_j p_k + p_k p_i}, \tag{2.33}$$

while the momenta of all other particles involved in the process are not modified. With this definition of the momenta $\widetilde{p}_{ij}$ and $\widetilde{p}_k$, the four momentum in the Born-level process is conserved, since

$$p_i^\mu + p_j^\mu + p_k^\mu = \widetilde{p}_{ij}^{\,\mu} + \widetilde{p}_k^{\,\mu}, \tag{2.34}$$

and the emitter and spectator partons are on-shell, $\widetilde{p}_{ij}^{\,2} = \widetilde{p}_k^{\,2} = 0$.

The Lorentz-structure of the splitting $\widetilde{ij} \to i, j$ is contained in the matrices $\mathbf{V}_{ij,k}$, which introduce a correlation between the Born-level matrix element and its complex conjugate in the spin of the emitter parton. In the following, the Born-level matrix elements are specified by the spin of the emitter particle, with s or s' denoting the spin of quarks and μ, ν being the spin indices of gluons. With this convention, the matrices $\mathbf{V}_{ij,k}$ for $\overset{(-)}{q} \to \overset{(-)}{q}\, g$, $g \to q\bar{q}$ and $g \to gg$ splitting read [68]

$$\begin{aligned}
\langle s|\mathbf{V}_{q_i g_j,k}|s'\rangle &= 8\pi\alpha_s C_F \delta_{ss'} \left[\frac{2}{1-z_i(1-y_{ij,k})} - (1+z_i)\right] + \mathcal{O}(\varepsilon), \\
\langle \mu|\mathbf{V}_{q_i \bar{q}_j,k}|\nu\rangle &= 8\pi\alpha_s T_R \left[-g^{\mu\nu} - \frac{2}{p_i p_j}(z_i p_i^\mu - z_j p_j^\mu)(z_i p_i^\nu - z_j p_j^\nu)\right] + \mathcal{O}(\varepsilon), \\
\langle \mu|\mathbf{V}_{g_i g_j,k}|\nu\rangle &= 16\pi\alpha_s C_A \Bigg[- g^{\mu\nu} \left(\frac{1}{1-z_i(1-y_{ij,k})} + \frac{1}{1-z_j(1-y_{ij,k})} - 2\right) \\
&\qquad + \frac{1}{p_i p_j}(z_i p_i^\mu - z_j p_j^\mu)(z_i p_i^\nu - z_j p_j^\nu)\Bigg] + \mathcal{O}(\varepsilon),
\end{aligned} \tag{2.35}$$

with

$$z_i = \frac{p_i p_k}{(p_i + p_j)\, p_k}, \qquad z_j = \frac{p_j p_k}{(p_i + p_j)\, p_k}. \tag{2.36}$$

In the collinear limit of the particles i and j, the splitting kernels defined in Eq. (2.35) become proportional to the Altarelli-Parisi splitting functions [64] and they therefore reproduce the correct asymptotic behavior in this phase space region.

The correct treatment of soft gluon radiation requires the introduction of color correlations between the Born-level matrix elements since the gluon can be emitted from any external parton involved in the process. This color correlation is given by the operators $\mathbf{T}_{ij}\mathbf{T}_k$ appearing in Eq. (2.31), which contain the additional generators of the SU(3) group for gluon exchange between the particles $\widetilde{ij}$ and $\widetilde{k}$. Hence, the factor $\mathbf{T}_{ij}^2$ appearing in Eq. (2.31) is

the quadratic Casimir invariant in the representation given by the particle $\widetilde{ij}$. Since color conservation guaranties

$$\sum_{j\neq i} \mathbf{T}_i \mathbf{T}_j = -\mathbf{T}_i^2, \tag{2.37}$$

the color factors in Eq. (2.31) do not modify the behavior of the subtraction term in the collinear regions and lead to the correct asymptotic behavior in the soft limit [68]. The color correlated matrix elements that are needed for the processes under consideration are given in Appendix A and the implementation of the dipoles is presented in Section 3.2.

Integrated dipoles

The analytical integration of the dipoles over the phase space of the real parton radiation in d space-time dimensions is presented in Ref. [68] and the resulting contributions can be added to $\mathrm{d}\sigma^V$ and $\mathrm{d}\sigma^C$. The collinear counter term $\mathrm{d}\sigma^C$ absorbs some of the divergences resulting from collinear initial state splittings into a redefinition of the pdfs. These divergences appear because the pdfs of the initial state partons are evaluated at different momentum fractions for the real emission contribution and the underlying Born-process. In the $\overline{MS}$ scheme, $\mathrm{d}\sigma^C$ reads [68]

$$\begin{aligned}\mathrm{d}\sigma^C_{ab}(p_a,p_b) = &-\frac{\alpha_s}{2\pi}\frac{1}{\Gamma(1-\varepsilon)}\sum_{c,d}\int_0^1 \mathrm{d}z_a z_b \mathrm{d}\sigma^B_{cd}(z_a p_a, z_b p_b)\\ &\cdot\left\{-\delta_{bd}\delta(1-z_b)\frac{1}{\varepsilon}\left(\frac{4\pi\mu^2}{\mu_F^2}\right)^{\varepsilon} P^{ac}(z_a) - \delta_{ac}\delta(1-z_a)\frac{1}{\varepsilon}\left(\frac{4\pi\mu^2}{\mu_F^2}\right)^{\varepsilon} P^{bd}(z_b)\right\},\end{aligned} \tag{2.38}$$

where $P^{ab}(z)$ are the Altarelli-Parisi splitting functions [64] for collinear parton splittings $a(p) \to b(zp) + b'(p - zp)$.

The sum of the integrated dipoles and the pdf counter term is

$$\mathrm{d}\sigma^C + \int_1 \mathrm{d}\sigma^A = \mathrm{d}\sigma^B \otimes \left[\mathbf{I} + \int_0^1 \mathrm{d}x \left(\mathbf{P}(x,\mu_F) + \mathbf{K}(x)\right)\right], \tag{2.39}$$

where $\otimes$ stands for appropriate color correlations of the operators $\mathbf{I}$, $\mathbf{P}$ and $\mathbf{K}$ with the Born-level contribution $\mathrm{d}\sigma^B$. The endpoint function $\mathbf{I}$ cancels the infrared singularities of the virtual contribution $\mathrm{d}\sigma^V$ (see Section 3.3), whereas the operators $\mathbf{P}$ and $\mathbf{K}$ are the finite remnants of the collinear initial state splittings, which will be discussed in Section 3.4.

2.2.3. Virtual Corrections, Renormalization and Running Coupling

The one-loop integrals appearing in the virtual amplitude are of the general form

$$\mathcal{T}_n^{\mu_1,\ldots,\mu_m} = \frac{(2\pi\mu)^{2\varepsilon}}{\mathrm{i}\pi^2}\int \mathrm{d}^d l\, \frac{l^{\mu_1}\cdots l^{\mu_m}}{D_0\cdots D_{n-1}}, \quad \text{with} \quad D_i = \left(l + \sum_{j=1}^{i} p_j\right)^2 - m_i^2 + \mathrm{i}0, \tag{2.40}$$

where the momenta of the external particles p_i are defined as flowing in and dimensional regularization is used as defined by Eq. (2.27). If some of the masses m_i appearing in the loop are zero, the integration over the loop momentum l includes regions where the integrand is singular because some of the denominators D get zero. This leads to the appearance of mass singularities [66], which exactly correspond to the infrared divergences of the real emission contribution. These divergences cancel in the sum of the one-loop amplitude and the endpoint function $\mathbf{I}$ (see Section 2.2.2).

In addition, the integral in Eq. (2.40) might diverge for $n \leq 4$ since the integral includes the limit $|\mathbf{l}| \to \infty$. These singularities of ultraviolet origin can be absorbed into a renormalization of the fields and coupling constants as described in many quantum field theory text books (see e.g. [59–61]). Using multiplicative renormalization, the bare quantities, as given by the Lagrangian, are replaced by renormalized ones according to

$$\Psi^0 = Z_\Psi^{1/2}\Psi^r, \qquad A_\mu^0 = Z_A^{1/2}A_\mu^r, \qquad g_s^0 = \mu^\varepsilon Z_g g_s^r, \tag{2.41}$$

where in the renormalization of the coupling constant g_s, a factor of μ^ε has been included to obtain a dimensionless renormalized coupling[‡]. The last equation also shows that the renormalized coupling has to be scale dependent, since the right hand side of the equation depends on the mass scale μ whereas g_s^0 is scale independent.

The renormalization constants can be written as a series expansion in α_s and they are fixed by the specification of renormalization conditions. Using on-shell renormalization of the fields, the renormalization constants of the massless quark and gluon fields are given by[§] [69]

$$Z_\Psi = 1 + \delta_\Psi = 1 - \frac{\alpha_s}{4\pi} C_F \left(\Delta^{\mathrm{UV}}(\mu) - \Delta^{\mathrm{IR}}(\mu)\right), \tag{2.42}$$

$$\begin{aligned} Z_A &= 1 + \delta_A \\ &= 1 - \frac{\alpha_s}{4\pi}\left[\left(\frac{4}{3}N_F T_R - \frac{5}{3}C_A\right)\left(\Delta^{\mathrm{UV}}(\mu) - \Delta^{\mathrm{IR}}(\mu)\right) + \frac{4}{3}T_R\left(\Delta^{\mathrm{UV}}(\mu) + \ln\frac{M^2}{m_t^2}\right)\right], \end{aligned} \tag{2.43}$$

where $N_F = 5$ quark flavors are considered to be massless. The Casimir invariants C_F, C_A and the Dynkin index T_R are given in Eq. (2.21) and the IR and UV poles are comprised in

$$\Delta(\mu) = \left(\frac{4\pi\mu^2}{M^2}\right)^\varepsilon \Gamma(1+\varepsilon)\frac{1}{\varepsilon}, \tag{2.44}$$

with an arbitrary mass parameter M.

The renormalization of the coupling constant is fixed by applying a renormalization condition that determines the three point function at a renormalization scale μ_R. This scale does not have to coincide with μ, leading to additional logarithms $\ln(\mu^2/\mu_R^2)$ due to factors of $(\mu^2/\mu_R^2)^\varepsilon$ multiplying the UV pole. At any order in perturbation theory, the results must not depend on the scale μ, which can serve as a check of the calculation. In the $\overline{\mathrm{MS}}$ scheme, the renormalization constant reads[§] [69]

$$\begin{aligned} Z_g &= 1 + \delta_g \\ &= 1 - \frac{\alpha_s}{4\pi}\left[\left(\frac{2}{3}N_F T_R - \frac{11}{6}C_A\right)\left(\Delta^{\mathrm{UV}}(\mu) - \ln\frac{\mu_R^2}{M^2}\right) + \frac{2}{3}T_R\left(\Delta^{\mathrm{UV}}(\mu) + \ln\frac{M^2}{m_t^2}\right)\right]. \end{aligned} \tag{2.45}$$

The relation of the bare and renormalized coupling constant in Eq. (2.41) leads to a connection between the μ_R dependence of the renormalized coupling and the renormalization constant Z_g. Since g_s^0 does not depend on the scale, we obtain the β function of QCD

$$\begin{aligned} \beta(g_s) &= \frac{\partial}{\partial \ln\mu_R} g_s = -\frac{g_s}{Z_g}\frac{\partial}{\partial \ln\mu_R} Z_g = -\frac{g_s}{Z_g}\frac{\partial}{\partial \ln\mu_R}\delta_g \\ &= -\frac{g_s^3}{16\pi^2}\beta_0 - \frac{g_s^5}{(16\pi^2)^2}\beta_1 + \mathcal{O}(g_s^7), \end{aligned} \tag{2.46}$$

[‡]The mass parameter μ appearing in the renormalization of g_s motivates the appearance of $\mu^{2\varepsilon}$ in Eqs. (2.27) and (2.40).

[§]The renormalization constants given here differ from the usual ones by terms of $\mathcal{O}(\varepsilon)$, which do not contribute at NLO.

with the coefficients [8, 70]

$$\beta_0 = \frac{11}{3}C_A - \frac{4}{3}N_F T_R = 11 - \frac{2}{3}N_F, \tag{2.47}$$

$$\beta_1 = \frac{34}{3}C_A^2 - \frac{20}{3}C_A N_F T_R - 4C_F N_F T_R = 102 - \frac{38}{3}N_F. \tag{2.48}$$

In contrast to quantum electrodynamics, the β function of QCD is negative for $N_F < 16$, leading to vanishing couplings in the limit $Q^2 \to \infty$, which is known as asymptotic freedom [8].

The scale dependence of $\alpha_s = \frac{g_s^2}{4\pi}$ is obtained by solving the differential equation (2.46). Including only the one-loop contribution β_0, it is

$$\alpha_s(Q^2) = \frac{\alpha_s(\mu_R^2)}{1 + \frac{\alpha_s(\mu_R^2)}{4\pi}\beta_0 \ln\frac{Q^2}{\mu_R^2}}. \tag{2.49}$$

Hence, $\alpha_s(Q^2)$ becomes large at small energy scales Q and diverges at

$$\Lambda_{\mathrm{QCD}} = \mu_R \exp\left(\frac{-2\pi}{\beta_0\,\alpha_s(\mu_R^2)}\right), \tag{2.50}$$

leading to a hadronization of the strongly interacting partons at low energy scales.

Using the scale Λ_{QCD}, the one-loop running of α_s, Eq. (2.49) can be rewritten as

$$\alpha_s(Q^2) = \frac{4\pi}{\beta_0 \ln(Q^2/\Lambda_{\mathrm{QCD}}^2)}. \tag{2.51}$$

Similarly, including the two-loop coefficient β_1, the scale dependence is

$$\alpha_s(Q^2) = \frac{4\pi}{\beta_0 \ln(Q^2/\Lambda_{\mathrm{QCD}}^2)}\left(1 - \frac{2\beta_1}{\beta_0}\frac{\ln\left[\ln(Q^2/\Lambda_{\mathrm{QCD}}^2)\right]}{\ln(Q^2/\Lambda_{\mathrm{QCD}}^2)}\right), \tag{2.52}$$

which is used for cross section calculations with NLO accuracy. In Eq. (2.52), the parameter Λ_{QCD} has to be fixed by the value of α_s at an arbitrary scale.

By solving the differential equation Eq. (2.46) to obtain the scale dependence of α_s, the leading logarithms $\ln^n(Q^2/\mu_R^2)$ are resummed to all orders in α_s. In perturbation theory, the cross section is written as an expansion in α_s,

$$\sigma = \sum_n \alpha_s^n(\mu_R^2)\sigma_n(\mu_R^2), \tag{2.53}$$

which is independent on the value of μ_R if all orders are included and a change of the renormalization scale therefore only corresponds to a reordering of this perturbative expansion. Truncating the perturbative expansion at a fixed order, however, leads to an artificial scale dependence, which shows the influence of the leading logarithmic terms of the neglected contributions.

2.2.4. Monte Carlo Integration and Phase Space Generation

Cross section calculations require the evaluation of the phase space integral as well as an integration over the momentum fractions of the two initial state partons. For a $2 \to n$ process, these are $3n - 3$ nontrivial integrals, which are usually evaluated using Monte

Carlo techniques with importance sampling. Since the convergence of Monte Carlo integrations is independent of the dimensionality of the integrals (see Eq. (2.56)), this method is predestined for multidimensional integrations. Furthermore, nontrivial phase space cuts can be applied and one can obtain arbitrary differential distributions without separated runs of the program.

Within Monte Carlo algorithms, the integral I of a n-dimensional function f is expressed as

$$I = \int \mathrm{d}^n x f(\vec{x}) = \int \mathrm{d}^n x \, \frac{f(\vec{x})}{g(\vec{x})} \, g(\vec{x}) \approx I_N = \frac{V}{N} \sum_{j=1}^{N} \frac{f(\vec{x}_j)}{g(\vec{x}_j)}, \tag{2.54}$$

where V is the volume of the integration region and the estimate I_N of the integral I is obtained by evaluating the function $f(\vec{x})$ at N sample points, which are randomly chosen according to the probability density $g(\vec{x})$. The sequence I_N is guaranteed to converge to I in the limit $N \to \infty$ and an estimate of the deviation of I_N from I can be obtained by calculating the variance of I_N, [71]

$$\mathrm{Var}(I_N) = (\Delta I_N)^2 = \frac{V^2}{N} \mathrm{Var}\left(\frac{f}{g}\right). \tag{2.55}$$

Therefore, the relative accuracy of the estimate behaves as

$$\frac{\Delta I_N}{I_N} \propto \frac{1}{\sqrt{N}} \sqrt{\mathrm{Var}\left(\frac{f}{g}\right)} \tag{2.56}$$

and hence does not depend on the dimension n of the integration. To improve the convergence of the integral, one can try to minimize the variance of f/g. In principle, this minimum is obtained if $g \propto |f|$. This is the basis of importance sampling algorithms, where the function g is modeled such that it approximates the function f.

In the VEGAS algorithm [71], the sampling points are generated considering all dimensions of the integration domain as independent. The function $g(\vec{x})$ can therefore be written in a factorized form

$$g(\vec{x}) = \prod_{i=1}^{n} g_i(x_i). \tag{2.57}$$

The generation of sampling points is split into multiple iterations, which allows to adjust the functions g_i after each iteration to improve its approximation of the integrand, starting with a uniform distribution for g in the first iteration. The functions g_i are implemented as step functions with M steps of different widths and the same number of sampling points is generated for all of the M regions. After each iteration the boundaries of the regions are adjusted such that each region gives the same contribution to the integral.

The calculation presented in this thesis is done within the VBFNLO [56–58] framework, where a modified version of the VEGAS algorithm, called MONACO, is implemented. After each iteration, the boundaries of the various regions are written into *grid-files*, which can be used as input for further program executions to start the integration with previously adjusted functions g_i.

The program VBFNLO also provides various routines that allow to construct phase space generators for an efficient mapping of the sampling points $\vec{x}$ to the momenta p_i^μ of the particles. This mapping is crucial to further reduce the variance appearing in Eq. (2.56). In particular, the resonances appearing due to s-channel contributions of heavy particles should be mapped with an appropriately chosen Breit-Wigner distribution.

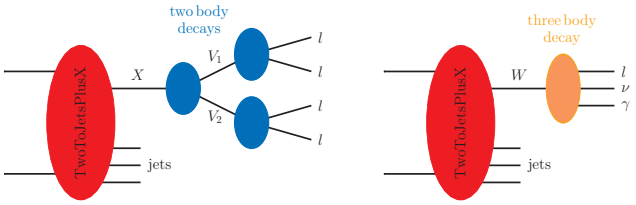

Figure 2.2.: Schematic representation of the phase space generation for $VVjj$ production. On the left, the momenta of the four final state leptons are generated by subsequent two body decays $X \to VV \to 4l$. The $W^{\pm}\gamma jj$ production peaks in two distinct phase space regions and requires the application of both depicted phase space generators as explained in the text.

The phase space for $VVjj$ production with leptonic decay of the vector boson can be generated as depicted in the left hand side of Fig. 2.2, using subsequent two body decays of a pseudo particle X, which is produced in association with the massless partons. This method allows to directly map the invariant mass of the two vector bosons, $m_{VV} = m_X$, to one of the components of the sampling points $\vec{x}$. The invariant masses of the two lepton pairs can be generated according to Breit-Wigner distributions corresponding to the mass and width of the corresponding vector boson V_i.

The calculation of $W\gamma jj$ production requires more attention since the amplitude peaks in two distinct regions of the phase space: The process includes $W\gamma jj$ production with the two body decay $W \to l\nu$ as well as Wjj production with the radiative decay $W \to l\nu\gamma$. An appropriate phase space mapping of the first contribution can be achieved by removing the two body decay of V_2 from the general process V_1V_2jj and setting $m_{V2} = 0$ in the phase space generator for the production of two massive vector bosons. In the phase space regions where the radiative decay is dominating, a phase space generator as shown in the right hand side of Fig. 2.2 should be used.

The phase space integration for $W^{\pm}\gamma jj$ production can therefore be split into two integrations if an additional cut is applied, which separates the two phase space regions. The appropriate phase space generator can efficiently be chosen by testing which of the invariant masses $m_{l\nu}$ and $m_{l\nu\gamma}$ is closest to m_W.

2.2.5. Photon Isolation

A further subtlety arises in the NLO calculation of $W^{\pm}\gamma jj$ production, since the splitting $q \to q\gamma$ diverges in the collinear limit. These divergences can in principle be mended by absorbing these divergences into a photon fragmentation function [72–74], which has to be determined experimentally. This procedure is similar to the factorization of collinear initial state splittings into the pdfs of the hadrons.

In this thesis, the singularities stemming from collinear quark-photon splittings are circumvented by applying an appropriate separation cut. At LO, these divergences can be removed by a cut on the R-separation of the photon and the jets, with

$$R_{j\gamma} = \sqrt{(\Delta y_{j\gamma})^2 + (\Delta \eta_{j\gamma})^2}. \tag{2.58}$$

However, applying this cut on the photon-jet separation does not remove all collinear divergences appearing in the NLO calculation since one has to use inclusive observables, where not all quarks have to be clustered into jets. In addition, a simple separation cut applied to all photon-parton pairs would spoil the cancellation of infrared singularities due to the restriction of the phase space for soft gluon radiation.

An IR-safe method to isolate the photon was proposed by S. Frixione [75], where in a smooth cone around the photon, collinear particle splittings are removed while keeping the full phase space for soft emissions. This can be achieved by requiring

$$\sum_{i\in\text{partons}} p_{T,i}\theta(R - R_{\gamma i}) \leq p_{T,\gamma}\frac{1-\cos R}{1-\cos\delta_0} \quad \forall R < \delta_0, \tag{2.59}$$

such that the allowed partonic energy increases with the distance to the photon. Parton radiations with the separation to the photon being larger than δ_0 are not restricted.

The results for $W^{\pm}\gamma jj$ production presented in Section 4.6 are obtained using this cut.

CHAPTER 3

Implementation

To study vector boson pair production in association with two jets, the QCD-induced contributions to the processes

$$\begin{aligned} pp &\to e^+\nu_e\,\mu^+\mu^-\,jj\,+X, \\ pp &\to e^-\bar{\nu}_e\,\mu^+\mu^-\,jj\,+X, \end{aligned} \tag{3.1a}$$

$$\begin{aligned} pp &\to e^+\nu_e\,\gamma\,jj\,+X, \\ pp &\to e^-\bar{\nu}_e\,\gamma\,jj\,+X, \end{aligned} \tag{3.1b}$$

$$\begin{aligned} pp &\to e^+\nu_e\,\mu^+\nu_\mu\,jj\,+X, \\ pp &\to e^-\bar{\nu}_e\,\mu^-\bar{\nu}_\mu\,jj\,+X \end{aligned} \tag{3.1c}$$

and

$$pp \to e^+e^-\,\mu^+\mu^-\,jj\,+X \tag{3.1d}$$

have been implemented into the flexible parton level Monte Carlo program VBFNLO [56–58] at next-to-leading order in the strong coupling constant, including all spin correlations and off-shell effects. For simplicity, the processes (3.1) are referred to as $W^\pm Zjj$, $W^\pm\gamma jj$, $W^\pm W^\pm jj$ and $ZZjj$ production, respectively. The calculation of above processes can be used to obtain the cross sections of the corresponding processes with leptons of the same generation in the final state, as well. In this case, an additional symmetry factor of $\frac{1}{2}$ has to be included for $W^\pm W^\pm jj$ and $ZZjj$ production*. The implementation of the processes $Z\gamma jj$ and W^+W^-jj is left for future work.

The focus of this chapter will be on the implementation of the amplitudes and subtraction terms (see Section 2.2.2). The other ingredients of the calculation, including an efficient phase space generator for the Monte Carlo integration, are already included in VBFNLO. Details of the implementation are presented taking $ZZjj$ production as an example, which is the most challenging process under consideration. It involves the summation over many spin configurations of the external particles and the virtual amplitudes include, besides hexagon diagrams appearing in all processes, closed quark loops with up to rank-five pentagon integrals. The implementation of the other processes is similar to $ZZjj$ production and the major differences will be pointed out in the text.

*The neglected interferences due to identical leptons are expected to be small (see e.g. [34]).

This chapter is organized as follows. In Section 3.1, the implementation of the processes at LO is described and general methods are presented, which are used for the other contributions as well. In Sections 3.2 and 3.3 the real emission contribution and virtual corrections are considered. The finite collinear subtraction term is discussed in Section 3.4. Finally, in Sections 3.5 and 3.6 some additional checks and optimizations are presented. Furthermore, the runtime of individual contributions is studied.

3.1. Born Contributions

The partonic subprocesses contributing to the processes under consideration can be classified into two groups, namely

$$qq \to qq + V_1\,V_2 \quad \text{and} \quad qg \to qg + V_1\,V_2, \tag{3.2}$$

which are referred to as 4-quark and 2-quark-2-gluon subprocesses in the following and also include crossing related contributions. Due to electric charge conservation, only the 4-quark subprocesses contribute to $W^\pm W^\pm jj$ production.

To evaluate the contributions of the individual subprocesses, the corresponding squared matrix elements have to be implemented, which is done using the helicity method of Ref. [76]. The processes W^+Zjj, W^-Zjj, $W^+\gamma jj$ and $W^-\gamma jj$ are very similar and therefore the same routines to evaluate the matrix elements are used, which internally take into account the minor differences of the four processes. Similarly, the processes W^+W^+jj and W^-W^-jj share the same implementation.

For a given process, the leptonic decay of the EW vector bosons is the same for all subprocesses and can be classified into two contributions. Either two vector bosons are emitted from the quark lines and each of them decays into a lepton pair, e.g. for $ZZjj$ production $V_1 \to e^+e^-$ and $V_2 \to \mu^+\mu^-$, or one vector boson couples to the quarks and decays into four leptons, $\tilde{V} \to e^+e^-\,\mu^+\mu^-$. Besides the contributions with V_i and $\tilde{V}$ being Z bosons, off-shell photons have to be taken into account to preserve gauge invariance. Hence, for each of the 4 spin configurations of the leptons, the decay currents Z_i^μ, A_i^μ, $\tilde{Z}^\mu$ and $\tilde{A}^\mu$, which are illustrated in Fig. 3.1 have to be calculated, which is done using HELAS routines [77]. Furthermore, it can be advantageous to combine the corresponding Z and photon currents to an effective current including the coupling constants to a quark of type $f \in \{u, d\}$ and helicity τ,

$$V^\mu_{i,q_f\tau} = g^{\gamma ff} \cdot A_i^\mu + g^{Zff}_\tau \cdot Z_i^\mu \tag{3.3}$$

and correspondingly for $\tilde{V}_{q_f\tau}$. This method allows to reduce the computing time of various contributions by a factor of two as shown later.

Using crossing symmetry, all subprocesses of $ZZjj$ production can be obtained using an implementation of the matrix elements for the subprocesses

$$q_1q_2 \to q_3q_4\,e^+e^-\,\mu^+\mu^- \quad \text{and} \quad q_1g_2 \to q_3g_4\,e^+e^-\,\mu^+\mu^-\,. \tag{3.4}$$

The corresponding two routines are called `ME4q` and `ME2q2g` in the following. To obtain a fast program, they evaluate all combinations of external quark flavors at once. If one considers five light quark flavors, this allows to evaluate all 140 subprocesses of the 4-quark type with only four calls to the `ME4q` routine.

First, the implementation of the matrix elements for the 2-quark-2-gluon subprocesses is discussed. The routine `ME2q2g` has the momenta, as they are generated by the phase space generator, and their assignment to the particles q_i and g_i as input parameters. In

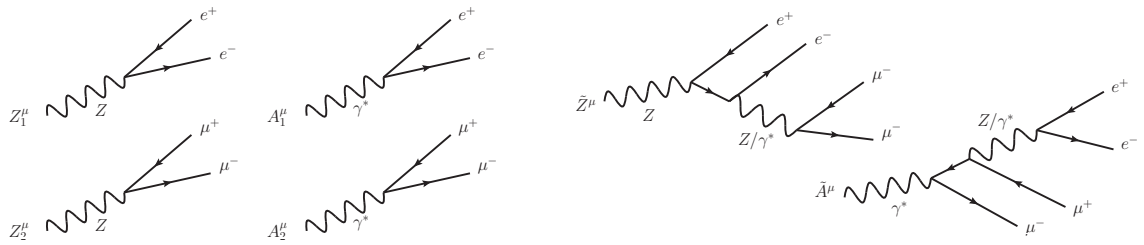

Figure 3.1.: Leptonic decays of the EW bosons for $ZZjj$ production. In the first group, each of the two vector bosons decays into a lepton pair. The decay of one vector boson into 4 leptons with 16 contributing Feynman diagrams is represented by the diagrams on the right hand side.

the following, the momenta p_i are defined as flowing in and the indices correspond to the particles as they appear in the Feynman diagrams. First, the wave functions of the external partons are calculated. Since these are assumed to be massless, two-component Weyl spinors can be used for the quarks, which are calculated for both helicity states τ and are denoted as $|q_1;\tau\rangle$ and $\langle\tau;q_3|$ in the following. Depending on the assignment of the quarks to the phase space momenta, these are spinors for either incoming or outgoing fermions. The wave functions of the gluons $\varepsilon^\mu_{i,\lambda_i}$ can be chosen to be real-valued using a rectangular polarization basis.

The following figure shows a representative Feynman diagram including color indices of the partons, needed when writing the full matrix element.

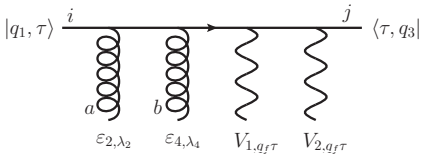

The wave functions can be contracted with each other to obtain off-shell wave functions of internal particles. Following the notation of Ref. [76], the contraction of e.g. the spinor $|q_1;\tau\rangle$ with the current $V_{1,q_f\tau}$ is denoted as $|V_1,q_1;\tau\, f\rangle$. Note that the latter wave function not only has to be calculated for the two possible quark helicities, but also for the two quark types f. Wave functions with a different permutation of the same particles can be combined, resulting in an efficient summation over the contributions of all Feynman diagrams. E.g. the emission of both EW vector bosons from the quark q_1 can be calculated as

$$|V_1V_2q_1;\tau f\rangle = |V_1,V_2,q_1;\tau\, f\rangle + |V_2,V_1,q_1;\tau\, f\rangle + |\tilde{V},q_1;\tau\, f\rangle, \tag{3.5}$$

where the permutation of the vector bosons is fixed for the contributions on the right hand side, whereas all contributions are included on the left. Here, the advantage of the effective currents defined in Eq. (3.3) becomes apparent: Keeping the helicity τ fixed, the above expression only has to be evaluated twice to obtain the contributions for up- and down-type quarks. Without the effective current, the quark flavor would not be fixed in the above expression, but the four combinations of photon and Z contributions would have to be taken into account.

For diagrams involving a triple gluon vertex, the off-shell current

$$g^{*\mu}_{\lambda_2\lambda_4} = \left[\varepsilon_{2,\lambda_2}\cdot\varepsilon_{4,\lambda_4}\,(p_2-p_4)^\mu + 2\,p_4\cdot\varepsilon_{2,\lambda_2}\,\varepsilon^\mu_{4,\lambda_4} - 2\,p_2\cdot\varepsilon_{4,\lambda_4}\,\varepsilon^\mu_{2,\lambda_2}\right]\frac{1}{(p_2+p_4)^2} \tag{3.6}$$

with color factor $\mathrm{i}f^{abc}$ is used.

Using the wave functions defined above, the full matrix elements can be obtained. Thereby, the individual contributions have to be assigned to the two color structures

$$\mathcal{C}_1 = (t^b t^a)_{ji} \quad \text{and} \quad \mathcal{C}_2 = (t^a t^b)_{ji}, \tag{3.7}$$

depending on the order in which the gluons are attached to the quark line. The diagrams with a triple gluon vertex have the color structure $\mathrm{i}f^{abc}t^c_{ji} = \mathcal{C}_2 - \mathcal{C}_1$ and therefore contribute to both structures. For a fixed combination of quark flavor f, helicity τ and gluon polarizations λ_2, λ_4, the full matrix element is

$$\begin{aligned}
\mathcal{M}_{f,\tau\lambda_2\lambda_4} = &\Big(\langle q_3|g^*|V_1V_2q_1\rangle + \langle q_3V_1V_2|g^*|q_1\rangle + \langle q_3V_1|g^*|V_2q_1\rangle + \langle q_3V_2|g^*|V_1q_1\rangle\Big)\cdot(\mathcal{C}_2 - \mathcal{C}_1)\\
&+\Big(\langle q_3V_1g_2|g_4|V_2q_1\rangle + \langle q_3V_2g_2|g_4|V_1q_1\rangle + \langle q_3V_1g_2|V_2|g_4q_1\rangle + \langle q_3V_2g_2|V_1|g_4q_1\rangle\\
&\quad + \langle q_3g_2|g_4|V_1V_2q_1\rangle + \langle q_3g_2|\tilde{V}|g_4q_1\rangle + \langle q_3V_1V_2|g_2|g_4q_1\rangle\Big)\cdot\mathcal{C}_2\\
&+\Big(\langle q_3V_1g_4|g_2|V_2q_1\rangle + \langle q_3V_2g_4|g_2|V_1q_1\rangle + \langle q_3V_1g_4|V_2|g_2q_1\rangle + \langle q_3V_2g_4|V_1|g_2q_1\rangle\\
&\quad + \langle q_3g_4|g_2|V_1V_2q_1\rangle + \langle q_3g_4|\tilde{V}|g_2q_1\rangle + \langle q_3V_1V_2|g_4|g_2q_1\rangle\Big)\cdot\mathcal{C}_1\\
= &\ \mathcal{M}_1\mathcal{C}_1 + \mathcal{M}_2\mathcal{C}_2,
\end{aligned} \tag{3.8}$$

where the flavor and helicity indices have been omitted on the right hand side. This matrix element has to be squared and summed over the colors of the partons, leading to

$$|\mathcal{M}_{f,\tau\lambda_2\lambda_4}|^2 = |\mathcal{M}_1|^2\,\langle\mathcal{C}_1|\mathcal{C}_1\rangle \;+\; |\mathcal{M}_2|^2\,\langle\mathcal{C}_2|\mathcal{C}_2\rangle \;+\; 2\,\mathrm{Re}(\mathcal{M}_1^*\mathcal{M}_2)\langle\mathcal{C}_1|\mathcal{C}_2\rangle. \tag{3.9}$$

The calculation of the color factors

$$\langle\mathcal{C}_1|\mathcal{C}_1\rangle = \langle\mathcal{C}_2|\mathcal{C}_2\rangle = N\cdot C_F = \frac{16}{3}, \tag{3.10}$$

$$\langle\mathcal{C}_1|\mathcal{C}_2\rangle = N\cdot C_F\cdot\left(C_F - \frac{C_A}{2}\right) = -\frac{2}{3} \tag{3.11}$$

is presented in Appendix A. Furthermore, the squared matrix element has to be multiplied with the appropriate power of the, so far neglected, strong coupling constant evaluated at the renormalization scale μ_R.

Eqs. (3.8)-(3.11) have to be evaluated for all combinations of the parton spins. Since the (off-shell) wave functions are calculated before the evaluation of the full matrix elements, many contributions can be used for various spin combinations and e.g. the contribution $|g_4q_1\rangle$, which does not depend on f and λ_2, does not has to be evaluated each time. After the summation over the parton spins, the routine returns the squared amplitude for the two distinct quark flavors.

The summation over the lepton helicities is performed using another method. Instead of calculating all spin configurations at each phase space point, a "random helicity summation" is applied. The simplest method would be to randomly choose and evaluate only one of the possible spin configurations at each phase space point. If its contribution is multiplied with the number of spin configurations, one obtains the same results after doing the Monte Carlo integration. The runtime of each phase space point can therefore be significantly reduced, but the Monte Carlo integration has to be done with more points since the fluctuations of the integrand increase. With the above method of random helicity summation, these fluctuations can become large since some phase space regions can

be dominated by a specific spin configuration. Therefore another method is used in this implementation, where all spin configurations contribute with randomly selected phase factors [78]. The spinor of an external fermion can be replaced by

$$u(\phi) = e^{\mathrm{i}\phi} u_+ + e^{-\mathrm{i}\phi} u_-, \tag{3.12}$$

where $u_\pm$ are the two spin states of the particle and ϕ is a random phase. Integrating the squared matrix elements over the random phase, which can be done together with the phase space integration using Monte Carlo techniques, one obtains

$$\int_0^{2\pi} \frac{\mathrm{d}\phi}{2\pi} \, |\mathcal{M} u(\phi)|^2 = \sum_\lambda |\mathcal{M} u_\lambda|^2, \tag{3.13}$$

where the mixed contributions involving the factors $e^{2\mathrm{i}\phi}\, \bar{u}_\pm u_\mp$ vanish due to the integration. For the vector boson pair production processes studied here, one can use two independent phases to get the decay currents

$$V_i^\mu(\phi_i) = \sum_{\tau_i} e^{2\tau_i \,\mathrm{i}\phi_i} \, V_{i,\tau}^\mu \quad \text{and} \quad \tilde{V}^\mu(\phi_1, \phi_2) = \sum_{\tau_1, \tau_2} e^{2\tau_1 \,\mathrm{i}\phi_1} e^{2\tau_2 \,\mathrm{i}\phi_2} \tilde{V}_{\tau_1 \tau_2}^\mu, \tag{3.14}$$

where the helicities τ_i refer to the helicities of the leptons. Random helicity summation could also be used for the summation over parton spins. However, as explained above the full summation can be done very efficiently. Furthermore, the Born amplitudes are needed for the real emission contribution as well, where the use of the full spin sum is advantageous to obtain full information about spin correlations.

The routine to evaluate the squared matrix elements has to be called seven times to obtain all crossing related contributions

$$q_1\, g_2 \;\to q_3\, g_4 \qquad\qquad g_2\, q_1 \;\to q_3\, g_4 \tag{3.15a}$$

$$\bar{q}_3\, g_2 \;\to \bar{q}_1\, g_4 \qquad\qquad g_2\, \bar{q}_3 \;\to \bar{q}_1\, g_4 \tag{3.15b}$$

$$q_1\, \bar{q}_3 \;\to g_2\, g_4 \qquad\qquad \bar{q}_3\, q_1 \;\to g_2\, g_4 \tag{3.15c}$$

and

$$g_2\, g_4 \to \bar{q}_1\, q_3. \tag{3.15d}$$

Using the results of the squared matrix elements for up- and down-type quarks, one can sum over all five light quark flavors of the quark line $q_1 \to q_3$ for each of the above subprocess groups. Thereby, the matrix elements have to be multiplied with the parton density functions of the initial state partons, the factors for averaging over initial state spins and colors, as well as with the symmetry factor of the final state.

The same methods can be used to obtain the Born contributions of the 4-quark subprocesses. The wave functions of the quarks and their contractions with the EW bosons are evaluated using the conventions as shown in the following representative diagram.

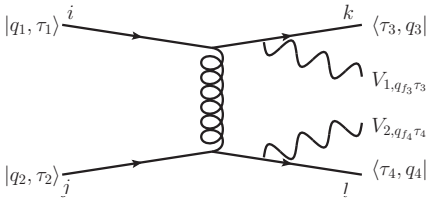

From these, the following currents are calculated ($a \in \{3,4\}$, $b \in \{1,2\}$)

$$\begin{aligned} J^{\mu}_{ab,\tau} =& \langle \tau_a = \tau; q_a|\gamma^\mu|q_b; \tau_b = \tau\rangle \\ J^{\mu}_{aV_ib,f\tau} =& \langle \tau_a = \tau; q_a|\gamma^\mu|V_iq_b; \tau_b = \tau, f\rangle + \langle \tau_a = \tau, f; q_aV_i|\gamma^\mu|q_b; \tau_b = \tau\rangle \\ J^{\mu}_{a\tilde{V}b,f\tau} =& \langle \tau_a = \tau; q_a|\gamma^\mu|V_1V_2q_b; \tau_b = \tau, f\rangle + \langle \tau_a = \tau, f; q_aV_1V_2|\gamma^\mu|q_b; \tau_b = \tau\rangle \\ &+ \langle \tau_a = \tau, f; q_aV_1|\gamma^\mu|V_2q_b; \tau_b = \tau, f\rangle + \langle \tau_a = \tau, f; q_aV_2|\gamma^\mu|V_1q_b; \tau_b = \tau, f\rangle. \end{aligned} \tag{3.16}$$

The full Born matrix elements are then obtained by contracting these currents with the propagator of the exchange gluon. All Feynman diagrams with a t-channel exchange between the two quark lines $q_1 \to q_3$ and $q_2 \to q_4$ with quark flavors f_1, f_2 and helicities τ_1, τ_2 are included in

$$\begin{aligned} &\mathcal{M}_{t,f_1f_2,\tau_1\tau_2} = g_s^2\, \mathcal{C}_t\, g_{\mu\nu} \cdot \\ &\left(\frac{J^{\mu}_{13,\tau_1}\, J^{\nu}_{2\tilde{V}4,f_2\tau_2}}{(p_1+p_3)^2} + \frac{J^{\mu}_{1V_13,f_1\tau_1}\, J^{\nu}_{2V_24,f_2\tau_2}}{(p_1+p_3+p_{V_1})^2} + \frac{J^{\mu}_{1V_23,f_1\tau_1}\, J^{\nu}_{2V_14,f_2\tau_2}}{(p_1+p_3+p_{V_2})^2} + \frac{J^{\mu}_{1\tilde{V}3,\tau_1}\, J^{\nu}_{24,f_2\tau_2}}{(p_2+p_4)^2} \right), \end{aligned} \tag{3.17}$$

with the color factor $\mathcal{C}_t = t^a_{ki}t^a_{lj}$. Furthermore, the corresponding contributions $\mathcal{M}_u$ for gluon exchange between the quark lines $q_1 \to q_4$ and $q_2 \to q_3$ is needed for subprocesses with identical quarks and for further optimizations. The matrix elements can be squared and summed over parton helicities to obtain 10 contributions

$$\begin{aligned} |\mathcal{M}_{t,f_1f_2}|^2 &= \sum_{\tau_1,\tau_2} |\mathcal{M}_{t,f_1f_2,\tau_1\tau_2}|^2, \\ |\mathcal{M}_{u,f_1f_2}|^2 &= \sum_{\tau_1,\tau_2} |\mathcal{M}_{u,f_1f_2,\tau_1\tau_2}|^2, \\ |\mathcal{M}_{tu,f=f_1=f_2}|^2 &= \sum_{\tau} |\mathcal{M}_{t,f,\tau} + \mathcal{M}_{u,f,\tau}|^2 + \sum_{\tau_1\neq\tau_2} |\mathcal{M}_{t,f,\tau_1\tau_2}|^2 + |M_{u,f,\tau_1\tau_2}|^2 \end{aligned} \tag{3.18}$$

for the various combinations of quark flavors. Note the difference between, e.g., $|\mathcal{M}_{t,dd}|^2$ and $|\mathcal{M}_{tu,dd}|^2$, which both only involve down type quarks. The former one has to be used for down-type quarks of different generations while the latter one involves identical quarks of the same generation. The products of the color factors appearing in the squared matrix elements can be found in Appendix A.

It is worth noting the color structure of the corresponding EW vector boson scattering processes, as well. These are $\mathcal{C}_t^{EW} = \delta_{ki}\delta_{lj}$ and $\mathcal{C}_u^{EW} = \delta_{kj}\delta_{li}$. Hence, one obtains for the interferences of the EW and QCD processes $\langle \mathcal{C}_t|\mathcal{C}_t^{EW}\rangle = \langle \mathcal{C}_u|\mathcal{C}_u^{EW}\rangle = 0$ and $\langle \mathcal{C}_t|\mathcal{C}_u^{EW}\rangle = N \cdot C_F = 4$. Interferences are therefore only possible between t-channel diagrams of the QCD and u-channel diagrams of the EW process, or vice versa, leading to a large suppression of the interferences.

Calculating the squared matrix element for the four crossings

$$q_1\, q_2 \to q_3\, q_4, \tag{3.19a}$$

$$\bar{q}_3\, \bar{q}_4 \to \bar{q}_1\, \bar{q}_2, \tag{3.19b}$$

$$q_1\, \bar{q}_3 \to \bar{q}_2\, q_4 \quad \text{and} \quad \bar{q}_3\, q_1 \to \bar{q}_2\, q_4, \tag{3.19c}$$

all 140 subprocesses of the 4-quark type can be obtained. Especially both contributions in the last line of Eq. (3.19) include 45 different subprocesses, as shown in Table 3.1, since the $\mathcal{M}_t$, $\mathcal{M}_u$ and $\mathcal{M}_{tu}$ contributions can be used. For the other two crossings, which involve 25 subprocesses, $\mathcal{M}_t$ and $\mathcal{M}_u$ are the same, so that only one of these has to be used. As for the 2-quark-2-gluon subprocesses, the squared matrix element for each subprocess has

$\mathcal{M}_{tu,uu}$	$u\,\bar{u} \to \bar{u}\,u,\ c\,\bar{c} \to \bar{c}\,c$
$\mathcal{M}_{tu,dd}$	$d\,\bar{d} \to \bar{d}\,d,\ s\,\bar{s} \to \bar{s}\,s,\ b\,\bar{b} \to \bar{b}\,b$
$\mathcal{M}_{t,uu}$	$u\,\bar{u} \to \bar{c}\,c,\ c\,\bar{c} \to \bar{u}\,u$
$\mathcal{M}_{t,ud}$	$u\,\bar{u} \to \bar{d}\,d,\ u\,\bar{u} \to \bar{s}\,s,\ u\,\bar{u} \to \bar{b}\,b,\ c\,\bar{c} \to \bar{d}\,d,\ c\,\bar{c} \to \bar{s}\,s,\ c\,\bar{c} \to \bar{b}\,b$
$\mathcal{M}_{t,du}$	$d\,\bar{d} \to \bar{u}\,u,\ d\,\bar{d} \to \bar{c}\,c,\ s\,\bar{s} \to \bar{u}\,u,\ s\,\bar{s} \to \bar{c}\,c,\ b\,\bar{b} \to \bar{u}\,u,\ b\,\bar{b} \to \bar{c}\,c$
$\mathcal{M}_{t,dd}$	$d\,\bar{d} \to \bar{s}\,s,\ d\,\bar{d} \to \bar{b}\,b,\ s\,\bar{s} \to \bar{d}\,d,\ s\,\bar{s} \to \bar{b}\,b,\ b\,\bar{b} \to \bar{d}\,d,\ b\,\bar{b} \to \bar{s}\,s$
$\mathcal{M}_{u,uu}$	$u\,\bar{c} \to \bar{c}\,u,\ c\,\bar{u} \to \bar{u}\,c$
$\mathcal{M}_{u,ud}$	$u\,\bar{d} \to \bar{d}\,u,\ u\,\bar{s} \to \bar{s}\,u,\ u\,\bar{b} \to \bar{b}\,u,\ c\,\bar{d} \to \bar{d}\,c,\ c\,\bar{s} \to \bar{s}\,c,\ c\,\bar{b} \to \bar{b}\,c$
$\mathcal{M}_{u,du}$	$d\,\bar{u} \to \bar{u}\,d,\ d\,\bar{c} \to \bar{c}\,d,\ s\,\bar{u} \to \bar{u}\,s,\ s\,\bar{c} \to \bar{c}\,s,\ b\,\bar{u} \to \bar{u}\,b,\ b\,\bar{c} \to \bar{c}\,b$
$\mathcal{M}_{u,dd}$	$d\,\bar{s} \to \bar{s}\,d,\ d\,\bar{b} \to \bar{b}\,d,\ s\,\bar{d} \to \bar{d}\,s,\ s\,\bar{b} \to \bar{b}\,s,\ b\,\bar{d} \to \bar{d}\,b,\ b\,\bar{s} \to \bar{s}\,b$

Table 3.1.: Subprocesses of the type $q_1\,\bar{q}_3 \to \bar{q}_2\,q_4\,ZZ$, where the weak bosons are omitted in the table. The matrix elements of all 45 subprocess are evaluated at once with one subroutine call.

to be multiplied with the corresponding parton density functions and the factors to take into account the multiplicity of initial state spins and colors. Furthermore, the symmetry factor of the final state has to be included.

The method described here allows for a very efficient summation over subprocesses and particle spins. For the 4-quark contributions, the calculation of the squared amplitude, which can be used to evaluate up to 45 subprocesses, has a runtime[†] of $7.6\,\mu s$, where one third of the runtime is needed for the evaluation of the EW decay currents. In contrast to this, the runtime of the matrix element $uu \to uu\,e^+e^-\,\mu^+\mu^-$ using `MadGraph` 4 [79], summing over all non-zero helicity configurations, is $520\,\mu s$ and the matrix element can not be used for subprocesses involving down-type quarks[‡]. It should be noted, that `MadGraph` 5 [54] came with a lot of speed improvements, however `MadDipole` [80], which has been used for various NLO calculations, is based on the older `MadGraph` version.

To further speed up the runtime of the cross section calculation, the contributions listed in the individual lines of Eqs. (3.15) and (3.19) are calculated in separate phase space integrations. This allows to evaluate the contributions which contribute less to the cross section with a smaller number of phase space points. This is discussed in more details in Section 3.5.

The implementation of the other processes can be done using the same methods described above. However, they involve other configurations of external quarks. For $W^\pm Zjj$ and $W^\pm\gamma jj$ production, the quark flavors of one quark line is fixed, with e.g. an incoming up-type quark converting into a down-type quark where a W^+ boson is emitted. Since the helicity of this quark line is fixed, only a reduced set of off-shell wave functions has to be calculated. A minor complication occurs during the evaluation of the matrix elements $\mathcal{M}_u$ of the 4-quark subprocesses. Depending on the charge of the W boson and the quark type of the second quark line, either the incoming quarks q_1, q_2 or outgoing quarks q_3, q_4 have to be interchanged to obtain the u-channel contribution. For the same reason, more crossings have to be evaluated to obtain all subprocesses.

For $W^\pm W^\pm jj$ production only processes of the 4-quark type appear due to electric charge

[†]All runtimes shown here are obtained on an Intel i5-3470 computer with one core and using the Intel-ifort version 12.1.0.

[‡]Using the matrix element for up-type quarks of different generations is possible with minor modifications of the code.

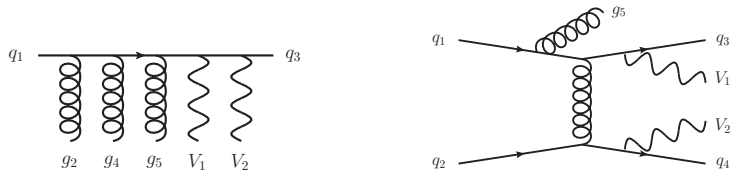

Figure 3.2.: Representative Feynman diagrams of the real emission contribution.

conservation. Since one W boson has to couple to each quark line, all external quark types and helicities are fixed, leading to a significant simplification of the implementation. Except for the quark-types being fixed, the subprocess summation can be done similar to $ZZjj$ production.

3.2. Real Emission

The calculation of the real emission contribution requires the evaluation of a large number of subprocesses with seven final state particles, which can be obtained by adding an additional gluon to the subprocesses of the Born level contribution. This leads to subprocesses with 2 quarks and 3 gluons as external partons as well as subprocesses with 4 quarks and one gluon as shown in Fig 3.2. The additional gluon is either added to the final state of the subprocesses listed in Eqs. (3.15) and (3.19), or it is in the initial state giving rise to subprocesses of the type

$$q_1\, g_5 \to \bar{q}_2\, q_3\, q_4, \qquad g_5\, q_1 \to \bar{q}_2\, q_3\, q_4 \tag{3.20a}$$

and

$$\bar{q}_3\, g_5 \to \bar{q}_1\, \bar{q}_2\, q_4, \qquad g_5\, \bar{q}_3 \to \bar{q}_1\, \bar{q}_2\, q_4. \tag{3.20b}$$

The matrix elements can be calculated using the same methods as for the Born contribution presented in the previous section. However, it involves more color structures and diagrams with four-gluon vertices or multiple triple-gluon vertices, which are handled using the prescription of Ref. [76].

In addition to the squared matrix elements, subtraction terms have to be constructed for each of the subprocesses to obtain a finite phase space integral at NLO. As explained in Section 2.2.2, this can be done following the dipole subtraction algorithm [68], where the subtraction term for each subprocess is expressed as a sum of dipoles. This sum involves up to 27 dipoles, as obtained for subprocesses of the type

$$q_1\, \bar{q}_3 \to g_2\, g_4\, g_5, \tag{3.21}$$

that has 9 emitter pairs and each of these has three possible spectator partons.

Each dipole requires the evaluation of a squared matrix element of the underlying Born process, that has to be calculated using the tilde-kinematics defined in Ref. [68]. These kinematics are obtained right after the generation of the phase space point. Exploiting symmetries of the dipoles, the 27 configurations of emitter pairs and spectator partons require the generation of 15 distinct tilde-kinematics as explained in the following.

For the dipoles with final state emitter and final state spectator, $\mathcal{D}_{ij,k}$, interchanging the phase space positions i and j of the emitter pair leads to the same tilde-kinematic, however, one has to interchange the splitting parameters $\tilde{z}_i$ and $\tilde{z}_j$ as well, which are

related by $\tilde{z}_i + \tilde{z}_j = 1$. Hence, there are three tilde-kinematics for this type of dipoles. The same symmetry can be applied to the dipoles of the *final-initial* type, $\mathcal{D}_{ij}^{a}$, leading to six kinematics. Furthermore, these kinematics are identical with the ones of the *initial-final* dipoles, $\mathcal{D}_{k}^{ai}$. To the *initial-initial* dipoles, $\mathcal{D}^{ai,b}$, no such symmetry can be applied, leading to six tilde-kinematics. Including the real emission phase space, 16 different kinematics appear during the evaluation of one phase space point.

In the implementation, a unique convention for mapping the momenta of the real emission configuration to the phase space positions of the tilde kinematics is used. The tilde-kinematics are, after generation, passed to the routine which evaluates the phase-space cuts and only the kinematics passing these are used in the following calculation of the real emission amplitude including the subtraction terms. Furthermore, the factorization and renormalization scale are evaluated for each of the kinematics.

In contrast to the Born contribution, the evaluation of the individual crossings, which are used to obtain all subprocesses, is not split into separated phase-space integrals. Instead, all subprocesses are evaluated for each phase space point, which allows to pre-calculate contributions, that are the same for various processes. Besides the decay currents of the EW vector bosons, which are common to all subprocesses, the wave functions of the partons are calculated and stored. This is done for gluons as well as (anti)quarks, including the two spin states, and at all phase space positions and for all of the 16 kinematics passing the cuts. Furthermore, the contraction of the quarks with up to two vector bosons is pre-calculated.

For each crossing, the squared matrix element is calculated, making use of the previously calculated wave functions. For the calculation of the dipoles, a process independent routine has been implemented which, in particular, requires the specification of a subroutine for the calculation of the underlying Born level amplitude. Depending on the splitting type and phase space positions of the emitter and spectator, which are further inputs to the routine, the correct dipole formula is selected and calculated according to Ref. [68]. In the following, the utilization of this routine will be explained, taking two subprocesses as examples.

The 2-quark-3-gluon subprocesses, e.g.

$$\bar{q}_3\, g_2 \to \bar{q}_1\, g_4\, g_5, \tag{3.22}$$

require the evaluation of dipoles with quark-gluon, or gluon-gluon splittings. There are six quark-gluon emitter pairs (i,j), with $i \in \{1,3\}$, $j \in \{2,4,5\}$, and three gluon-gluon emitter pairs (i,j), with $i,j \in \{2,4,5\}$ and $i \neq j$. For each of the emitter pairs, and under the condition that at least one of the particles i, j is in the final state, there are three dipoles with the spectators $k \notin \{i,\, j\}$. As an example, the dipole $(1,2)$ with $k = 5$ is considered in the following. Before the routine for evaluating the dipole can be called, the crossing in the corresponding tilde-kinematics has to be specified, which is given by

$$\bar{q}_3\, q_1^e \to g_2^s\, g_4, \tag{3.23}$$

where the superscripts e and s specify the emitter and spectator particles. The assignment of g_2 and not g_4 being the spectator is arbitrary, but the phase space position of each particle is fixed by the conventions used for the calculation of the tilde-kinematics. The various dipole formulas of Ref. [68] have been implemented in a FORTRAN routine `Dipole`, which has to be called for each possible combination of i,j and k. For above example, the corresponding call to this function can symbolically be written as

`Dipole`$(p^{\mu}_{i,kin}, kin,$ 'qg', $3, 2, 5,$ `ColCorrME2q2g`$, (3,1 \to 2,4),\ 1,\ 2,$ results, $N_{\text{results}})$.

The first parameter is an array of all parton momenta in the real emission and the tilde-kinematics. The tilde-kinematics that have to be used for the evaluation of the Born matrix element and the splitting type are specified by the following two parameters. After that, the phase space positions of the emitter pair and spectator are given. The next four parameters specify the calculation of the color- and spin-correlated Born matrix elements. The subroutine `ColCorrME2q2g` will be discussed later. Besides the crossing of the Born matrix element, the diagram indices of the emitter and spectator are given. Similar to the routines that are used to evaluate the squared matrix elements, various configurations of the quarks can be evaluated at once. The dipoles of these configurations only differ by the Born matrix element. Therefore, with N_{results} one can specify the number of contributions that are calculated by the routine `ColCorrME2q2g` and the dipoles are evaluated for each of these.

The routine `ColCorrME2q2g` is used as an interface to the routine `ME2q2g`, which is called with a special entry point. Using this entry point, not only the squared matrix element for the various quark configurations is calculated, but also a minimal set of color- and spin-correlated matrix elements is returned. The spin correlation of dipoles with a quark as emitter parton is trivial, since for massless quarks the dipoles are diagonal in spin space. For gluon emitters, the spin- and color correlated matrix elements are of the form $\langle\mu|\mathbf{T}_e\mathbf{T}_s|\nu\rangle$, where $\langle\mu|$ and $|\nu\rangle$ are the matrix elements $\mathcal{M}^{*\mu}$ and $\mathcal{M}^{\nu}$ with the polarization vector of the emitter gluon being stripped off and $\mathbf{T}_e\mathbf{T}_s$ is the color correlation of the emitter and spectator, that will be treated later. Using a real-valued, rectangular basis of polarization vectors ε_μ^λ, the dipoles can be written in the general form

$$\begin{aligned}\mathcal{D} = D^{\mu\nu}\,\langle\mu|\mathbf{T}_e\mathbf{T}_s|\nu\rangle &= \sum_{\lambda_1,\lambda_2} D^{\mu\nu}\,\varepsilon_\mu^{\lambda_1}\varepsilon_{\mu'}^{\lambda_1}\,\langle\mu'|\mathbf{T}_e\mathbf{T}_s|\nu'\rangle\,\varepsilon_\nu^{\lambda_2}\varepsilon_{\nu'}^{\lambda_2} \\ &= \sum_\lambda \left(D^{\mu\nu}\,\varepsilon_\mu^\lambda\varepsilon_\nu^\lambda\right)\,\langle\lambda|\mathbf{T}_e\mathbf{T}_s|\lambda\rangle + \left(D^{\mu\nu}\,\varepsilon_\mu^1\varepsilon_\nu^2\right)\,\cdot 2\,\mathrm{Re}\,\langle 1|\mathbf{T}_e\mathbf{T}_s|2\rangle,\end{aligned} \tag{3.24}$$

where $\mathcal{D}^{\mu\nu}$ contains the splitting functions $\langle\mu|\mathbf{V}|\nu\rangle$ defined in Ref. [68] (see also Section 2.2.2). Therefore, the Born level matrix elements can be calculated with the usual polarization vectors, however, when squaring the amplitude, the results have to be split into the above distinct configurations of the emitter polarization. The sum over the spins of the other partons can be obtained as usual.

Due to color conservation, there are three independent color correlations, $\mathbf{T}_1\mathbf{T}_i$, with $i \in \{1,2,3\}$. These modify the color factors appearing in Eq. (3.9), where instead the factors $\langle\mathcal{C}_i|\mathbf{T}_1\mathbf{T}_j|\mathcal{C}_j\rangle$ have to be used, which are listed in Appendix A. To allow using the result of the entry point to the `ME2q2g` subroutine for all combinations of emitter and spectator partons, the 9 results $\langle 1|\mathbf{T}_1\mathbf{T}_i|1\rangle$, $\langle 2|\mathbf{T}_1\mathbf{T}_i|2\rangle$ and $2\,\mathrm{Re}\,\langle 1|\mathbf{T}_1\mathbf{T}_i|2\rangle$, with $i \in \{1,2,3\}$, are calculated for both gluons (and for the two configurations of quark flavors). Similarly, the color-correlated matrix elements with the emitter being a quark can be obtained from above results.

One task of the routine `ColCorrME2q2g` is to call the entry point to `ME2q2g` to obtain the color- and spin-correlated matrix element for a given emitter and spectator. However, it also caches the results of the matrix elements to avoid the recalculation of matrix elements appearing in various dipoles. This caching system uses the unique identifier of the tilde-kinematic as well as the phase space positions of the quarks q_1 and q_3 to identify the matrix elements. Bose symmetry can be used to define a unique order of the gluons g_2 and g_4 in terms of phase space positions. However, when interchanging the gluons, one has to take care of this redefinition when calculating the spin- and color-correlated matrix element in case that one of the gluons is the emitter or a spectator parton.

After calculating the squared matrix elements and all possible dipoles for a given crossing with general quark flavor types, the summation over the five light quark flavors can be done. Each subprocess has to be multiplied with the corresponding spin and color averaging factors as well as the parton density functions of the initial state partons. For the dipole contributions, the pdfs and the strong coupling constant have to be evaluated at the factorization and renormalization scales determined by the corresponding tilde-kinematics.

The same strategy can be applied to the subprocesses with four quarks and one gluon, e.g.

$$q_1\, g_5 \to \bar{q}_2\, q_3\, q_4. \tag{3.25}$$

The dipoles with quark-gluon splittings involve the calculation of color-correlated amplitudes of the 4-quark type. This is done by the routine `ColCorrME4q`, similar to `ColCorrME2q2g`, which calls an entry point of the `ME4q` routine. Again, the matrix elements are cached, taking into account that simultaneously changing the quarks q_3 and q_4 as well as $\mathcal{M}_t$ and $\mathcal{M}_u$ reproduces the same results. The dipoles can be calculated by calling the routine `Dipole`. For the quark-gluon splittings, the corresponding Born level process is obtained by removing the gluon from the process and moving the emitter quark to its position. For the above crossing, e.g. the emitter pair $(3, 5)$ leads to the Born level process

$$q_1\, \bar{q}_3^e \to \bar{q}_2\, q_4, \tag{3.26}$$

where the emitter particle is specified by a superscript e and each of the other partons can serve as an spectator. The dipoles are then calculated by calling the routine `Dipole` with the splitting type 'qg' and specifying the routine `ME4q` for the calculation of the Born level matrix element. In addition, dipoles with a gluon splitting into a quark-antiquark pair have to be considered. For processes of the type $\mathcal{M}_t$ (see Table 3.1), the quark pair $(q_1,\, q_3)$ or $(q_2,\, q_4)$ can be replaced by a gluon. The pairs (q_1, q_4) and (q_2, q_3) have to be replaced for the subprocesses of the $\mathcal{M}_u$ process and all four replacements have to be done for the $\mathcal{M}_{tu}$ subprocesses. After this, the corresponding Born level process of the 2-quark-2-gluon type has to be specified, e.g. for the emitter pair (q_2, q_4) in above process, one obtains the Born level process

$$q_1\, g_2 \to g_4^e\, q_3. \tag{3.27}$$

The corresponding dipole can be evaluated by calling the `Dipole` routine with the splitting type 'qq' and the routine `ME2q2g` as arguments.

Since the dipoles cancel the divergent contributions of the real emission matrix elements in the infrared regions, the dipoles can be tested by evaluating

$$R = \left| \frac{|\mathcal{M}|^2 + \mathcal{D}}{|\mathcal{M}|^2} \right|, \tag{3.28}$$

where $\mathcal{D}$ represents the sum of the dipoles. This ratio should go to zero, as the invariant mass m_{ij} of an emitter pair or the energy of a final state gluon E_i decrease. This has been checked for the individual real emission subprocesses in the various soft and collinear regions. Fig. 3.3 shows the cancellation after summing over all subprocesses. Besides the convergence of the subtraction terms towards the real emission matrix elements, it also shows that numerical problems might appear in the far collinear region, as it can be seen in the upper left panel for $m_{ai} \lesssim 1\,\text{MeV}$. To avoid such problems, a technical cut $m > 0.1\,\text{GeV}$ on the invariant mass of all parton pairs is applied in `VBFNLO`. It has been checked that the results are insensitive to this cut.

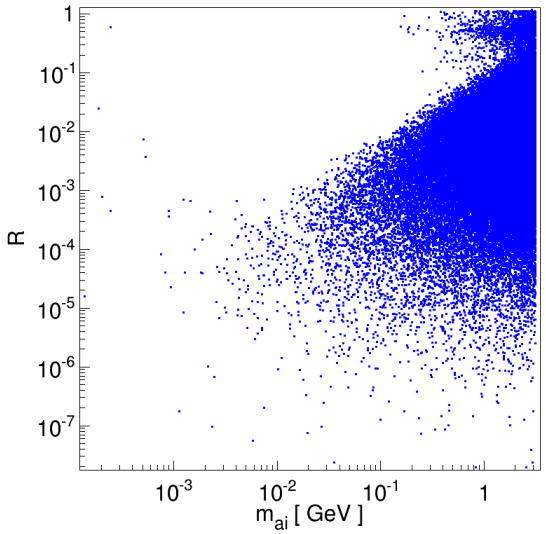

(1) Collinear initial state radiation.

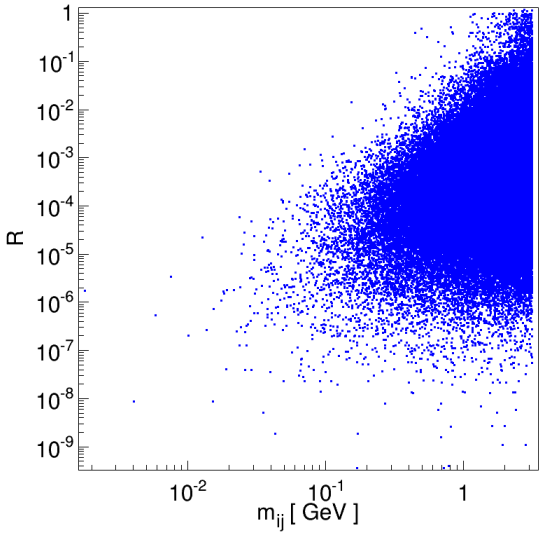

(2) Collinear final state radiation.

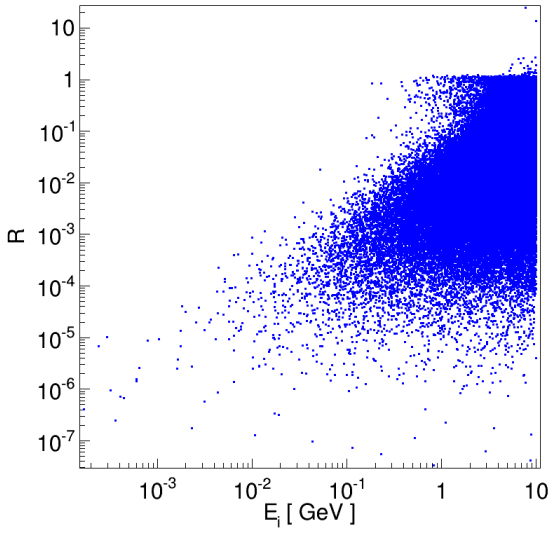

(3) Soft radiation.

Figure 3.3.: Cancellation of the real emission amplitudes with the subtraction terms in the soft and collinear regions for the process $ZZjj$. All subprocesses and all combinations $a \in \{1, 2\}$ and $i, j \in \{3, 4, 5\}$ are included. The cancellation is specified by the relative difference R of the real emission amplitudes and subtraction terms as given by Eq. (3.28).

3.3. Virtual Amplitudes

3.3.1. Building Blocks

The implementation of the virtual amplitudes, including up to hexagon contributions, is the most challenging part of the calculation. To deal with the large number of Feynman diagrams, the amplitudes are constructed using building blocks, that combine the evaluation of various diagrams with identical ordering of the external particles. These building blocks, which have been implemented by another member of the collaboration, use external currents as inputs and assume a general coupling structure of the vector bosons to fermions with the coupling constants stripped off. They are therefore very generic and can be used for the calculations of other processes in VBFNLO [56–58]. In the following, we concentrate on the building blocks containing the hexagon diagrams.

Two of these building blocks, which have already been used for the calculation of $W\gamma\gamma j$ in Ref. [81], are shown in Figs. 3.4 and 3.5. The "HexLine" routines collect one-loop corrections to Born topologies where four vector bosons are attached to a quark line. These vector bosons can be general effective currents as already used in Section 3.1. To

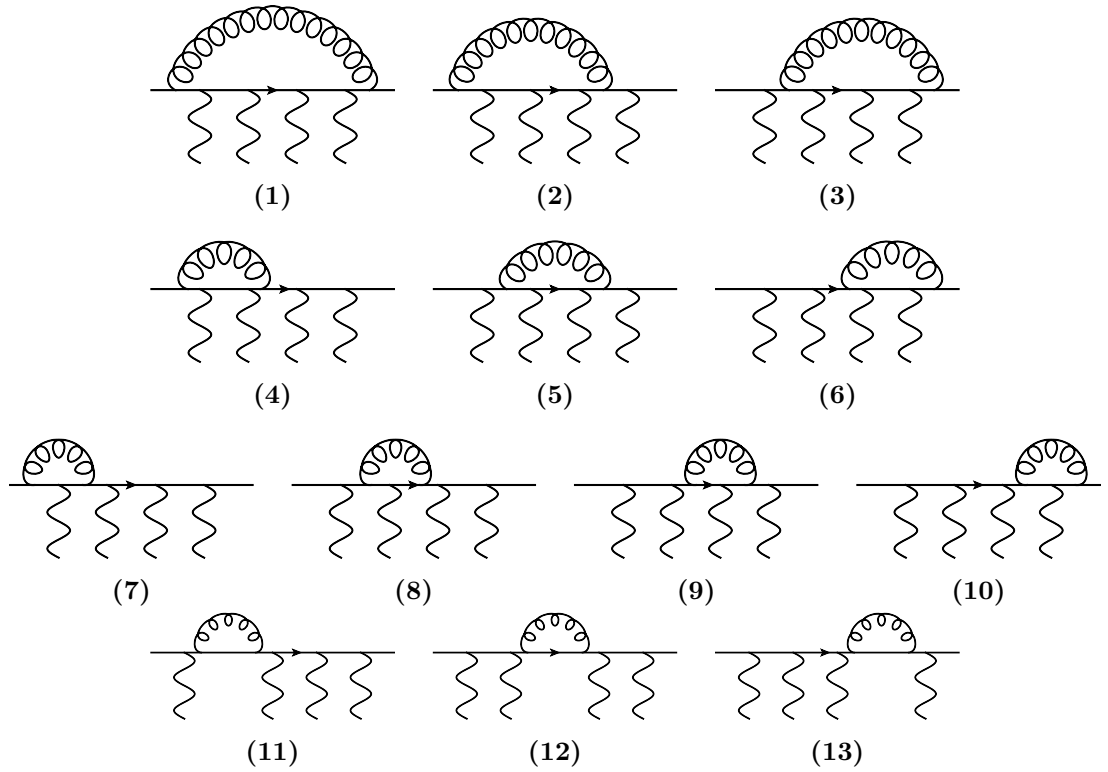

Figure 3.4.: The "HexLine Abelian" contribution collects one-loop corrections to a quark-line with four vector bosons attached. It includes Hexagon, Pentagon, Box, Vertex and Self-energy corrections.

allow gluons being attached to the quark line as well, the number and position of these have to be assigned to the routines and the result is then split into the contributions to the individual color structures. A calculation of the color factors can be found in Appendix A. In the "HexLine Abelian" (Fig. 3.4), the diagrams with at most one external gluon being attached inside the loop contribute to the corresponding color structure of the Born diagram with an additional factor of C_F or $(C_F - C_A/2)$ for the case of no and one gluon, respectively. The option to allow two external gluons being attached to the loop had to be added to the routine. In this case the color structure is given by

$$t^c t^a t^b t^c = \left(C_F - \frac{C_A}{2}\right) t^a t^b + \frac{1}{2N} C_A T_R \delta^{ab} \mathbb{1} = -\frac{1}{6} t^a t^b + \frac{1}{4} \delta^{ab} \mathbb{1}, \tag{3.29}$$

or the corresponding one with the indices a and b interchanged. It therefore contributes to the color structure of the corresponding Born diagram, as well as the color structure $\delta^{ab}\mathbb{1}$, which doesn't appear at LO.

In the "HexLine NonAbelian" routine, one of the vector bosons is a gluon attached to the gluon arc. The option that one of the three vector bosons attached to the quark line can be a gluon, had to be added here, as well. Depending on its position, the diagrams contribute to different color structures: if e.g. in Fig. 3.5 the gluon at the top of the diagrams has color index a and the middle one of the lower vector bosons is a gluon with color index b, the diagrams (4)-(6) contribute to the color structures $t^b t^a$, $\delta^{ab}\mathbb{1}$ and $t^a t^b$, respectively. The corresponding color factors can be found in Appendix A.

Similar to the Abelian and NonAbelian HexLine building blocks, there are PenLine and BoxLine routines, that collect one-loop corrections to a quark line with three or two vector bosons attached to it. Again, the option to have two external gluons has to be added to the existing routines.

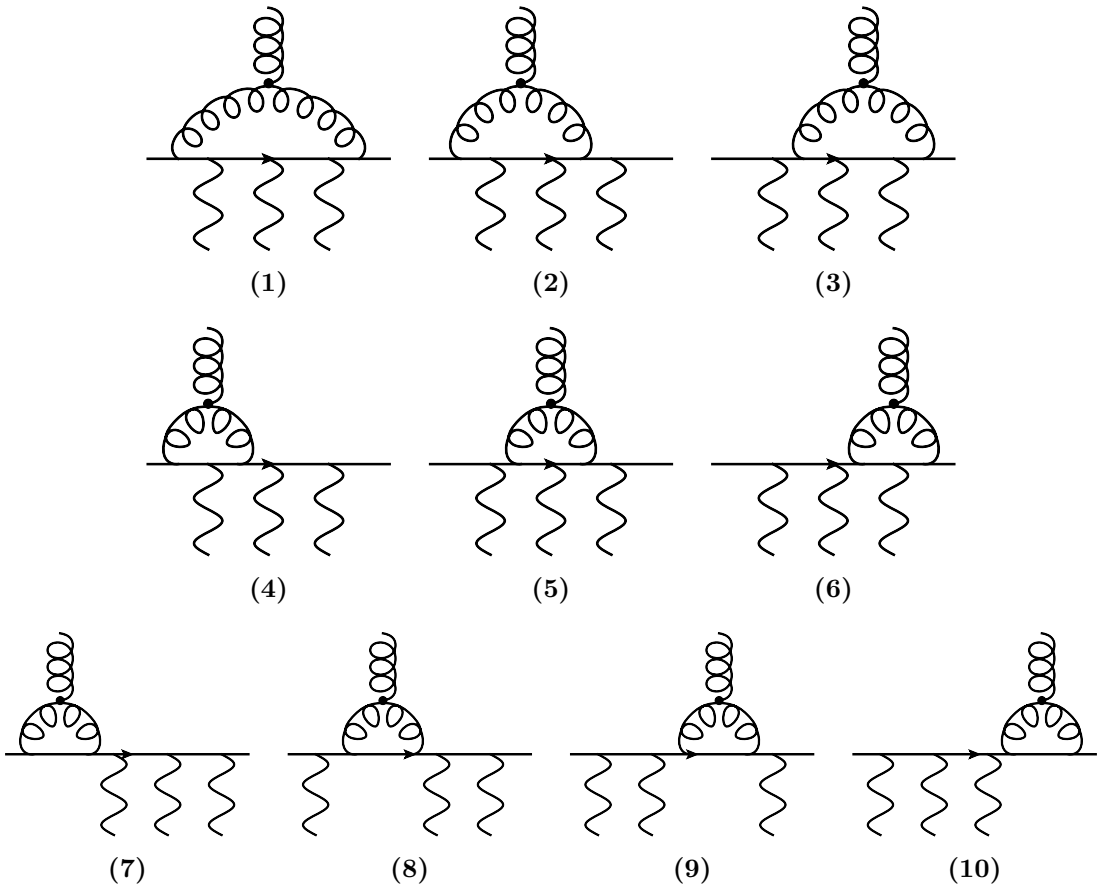

Figure 3.5.: The "HexLine NonAbelian" involves diagrams with three vector bosons attached to the quark line and a gluon attached to the gluon arc.

In addition to the above routines that only have to be modified, there are some new building blocks that explicitly involve four external partons. Fig. 3.6 shows new hexagon topologies appearing in the virtual amplitude of the 2-quark-2-gluon subprocesses. The left diagram involves two 3-gluon vertices and a new building block is assembled, combining this diagram with the corresponding two pentagon and three box diagrams that one obtains by moving the vector bosons along the quark line. Similarly a building block consisting of six diagrams is created by combining diagrams with a 4-gluon vertex. The right diagram of Fig. 3.6 represents this building block. The color structure of these contributions is presented in Appendix A. In addition to these two new HexLine building blocks, two similar PenLine building blocks have to be created, where only one external vector boson is attached to the quark.

In the 4-quark amplitudes, there are additional building blocks collecting Feynman diagrams with two gluons being exchanged between the two quark lines. Fig. 3.7 shows four diagrams representing four new building blocks. As for the other building blocks, the hexagon diagrams shown in Fig. 3.7 are combined with the diagrams one obtains by moving the external vector bosons along the quark lines, thereby including pentagon and box contributions. The four building blocks are therefore called "HexBox" contributions. The top row of Fig. 3.7 represents the "HexBox1" contributions, where the two vector bosons are coupled to the same quark line. They can be further classified into a "direct" (left diagram) and a "crossed" (right diagram) contribution, depending on the ordering of the internal gluons. As shown in Appendix A, they contribute with different color factors to the color structures $\mathcal{C}_t$ and $\mathcal{C}_u$. Each of this two HexBox1 contributions consists of 6 Feynman diagrams. The lower row of Fig. 3.7 represents the "HexBox2" building blocks,

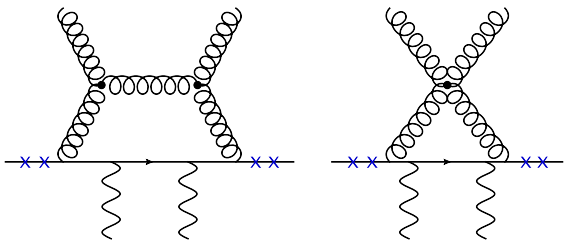

Figure 3.6.: Representative Feynman diagrams of two new building blocks appearing in the virtual amplitude of the 2-quark-2-gluon subprocesses. In the building blocks, the diagrams shown here are combined with the corresponding ones, where the EW vector bosons are moved along the quark line to the positions indicated with a cross. Therefore, each building block consists of 6 diagrams.

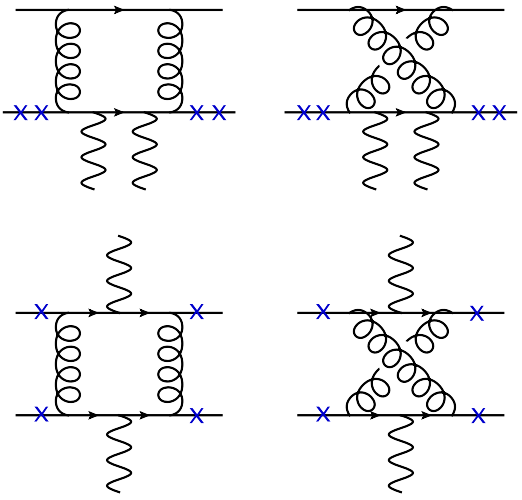

Figure 3.7.: Representative Feynman diagrams of new building blocks appearing in the virtual amplitude of the 4-quark subprocesses. In the building blocks, the diagrams shown here are combined with the corresponding ones, where the EW vector bosons are moved along the quark line to the positions indicated with a cross. Therefore, each of the diagrams shown in the upper row, which represents the "HexBox1" building block represents 6 diagrams. The "HexBox2" building block is represented by the diagrams in the lower row, which represent 9 diagrams.

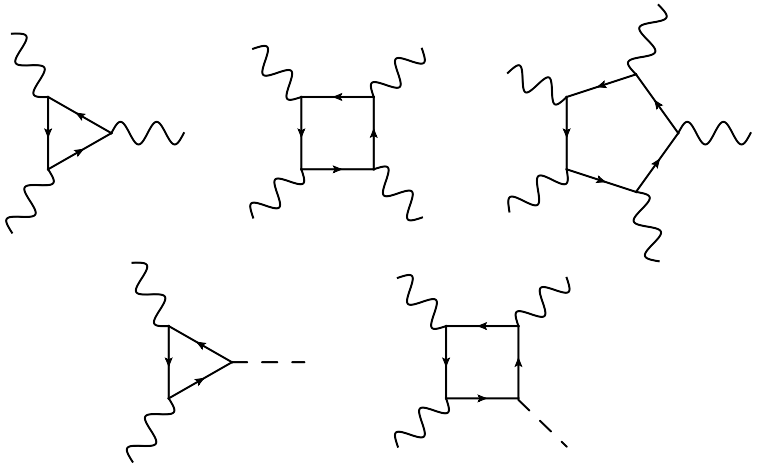

Figure 3.8.: Fermion loop diagrams appearing in the virtual amplitudes. The Higgs contributions shown in the second row only contribute to the process $ZZjj$.

in which one vector boson is attached to each quark line. Similar to the HexBox1, it is split into a direct and crossed contribution, each including nine diagrams. Furthermore, there are direct and crossed "PenBox" routines, where only one vector boson is coupled to a quark line.

Besides the above explained building blocks, the one-loop amplitude involves further self energy and vertex corrections as well as closed quark loops (see Fig. 3.8). The latter ones include up to pentagon diagrams of rank five in the case of $ZZjj$ production and involve massless as well as the massive top quarks. For this specific process, there are also contributions with a Higgs boson coupling to a closed top quark loop and the Higgs boson decaying to a Z boson pair. To deal with the large number of fermion loop contributions in $ZZjj$ production, parts of the code for gluon-induced ZZj production [82] have been used. For the other processes, an own implementation has been created using the general building blocks for the fermion loops. Where possible, Furry's theorem has been used to reduce the number of subroutine calls.

To compute the individual building blocks, we used the program described in Ref. [83]. The method is summarized in the following. The strategy is to use the `Mathematica` program with the `FeynCalc` [84] package to do algebraic simplifications in D dimensions and to obtain expressions for the Feynman diagrams that can be calculated numerically. The Feynman gauge as well as the anticommuting prescription of γ_5 [85] are used. Except for the fermion loop contributions, all quarks appearing in the diagrams are massless, and therefore their helicity can be fixed and is used as an input parameter to the building blocks. Hence, the coupling constants can be stripped off and the vector bosons can be assumed to be general effective currents with a vector-like coupling to the quark. For the closed quark loop diagrams, this method cannot be used in case of massive quarks and a general coupling

$$\gamma_\mu \left(g_L P_L + g_R P_R\right) \tag{3.30}$$

of the vector bosons to the quark is applied, where $P_{L,R} = (\mathbb{1} \mp \gamma_5)/2$ are the projection operators onto left- and right-handed spinor components and $g_{L,R}$ are the corresponding coupling constants, which are input parameters to the building blocks.

With this general couplings, the Feynman rules are applied to the diagrams of a building block to obtain analytic expressions of the matrix elements in d dimensions. Then, the Dirac matrices are reordered to collect repeated indices and the contraction $\gamma^\mu\gamma_\mu = D$ is applied. Note that the result of this contraction is D, whereas the dimensionality of the loop momentum is d. This allows to obtain results using conventional dimensional regularization in the t'Hooft Veltman scheme [86] where $D = d$ or in the four-dimensional helicity scheme [87] where $D = 4$. An overview of the different regularization schemes can be found in Ref. [88].

In addition to the contraction of repeated indices, all γ_5 matrices appearing in the fermion loop contributions are moved to the right using the anti-commutation relation. Similarly, the Dirac matrices contracted with the loop momentum l are moved to the right and the terms containing $\not{l}\not{l} = l^2$ or $l \cdot p_i$ are canceled with the denominators to obtain simpler one-loop integrals. The results of the individual diagrams i are then split into two contributions,

$$\mathcal{M}_i = \mathcal{M}_i^{D=4} + (D-4)\,\mathcal{M}_i^{DR}, \tag{3.31}$$

where $\mathcal{M}_i^{D=4}$ are the results one obtains in dimensional reduction by setting $D = 4$. The poles of $\mathcal{M}_i^{DR}$ lead to rational terms when using conventional dimensional regularization ($D = d$), which factorize against the corresponding Born matrix elements. Therefore, the building blocks only contain the contributions $\mathcal{M}_i^{D=4}$ and the additional rational terms

can be added manually to the amplitude to obtain results in conventional dimensional regularization. Since except for wave function renormalization graphs, all rational terms are of UV origin [89], the second term of Eq. (3.31) does not lead to additional contributions to the poles of the amplitude.

The two contributions of Eq. (3.31) are then decomposed into spinor chains, called standard matrix elements SM_j, that can be evaluated using the helicity method [76] with a fixed helicity τ, and additional factors T_k and F_k which are calculated from the kinematic variables and polarization vectors

$$\mathcal{M}_i^{D=4,DR} = \sum_{j,k,\tau} \mathrm{SM}_{j,\tau}\, F_k\, T_k. \tag{3.32}$$

The full dependence on the polarization vectors is included in T_k, whereas F_k in particular includes the scalar and tensor one-loop integral coefficients. After this decomposition, a FORTRAN code for the building block is generated. The tensor coefficients appearing in F_k are evaluated numerically using the reduction formalism of Passarino and Veltman [90] for up to four point functions and the method by Denner and Dittmaier [91] for the pentagon and hexagon integrals. The latter reduction algorithm has been implemented in terms of the momenta external to the loop, using the notation of Ref. [90] as presented in Ref. [83]. Additional rational terms appearing in the tensor reduction are included and the scalar integrals are calculated as in Refs. [92–96].

An additional input parameter of the building blocks allows to switch between the evaluation of the finite part or the ε^{-2} and ε^{-1} poles of the one-loop integrals. Using these building blocks to create the scattering amplitudes therefore allows to calculate the finite parts and the poles with the same code and the cancellation of the poles with the endpoint function $\mathbf{I}$ (see Section 2.2.2) is a first check of the calculation. Since the factor F_k in Eq. (3.32) does not contain the polarization vectors of the external currents, an efficient summation over configurations with identical kinematics is possible, thereby avoiding the time consuming recalculation of the tensor integrals. With only a minor increase of computing time, this allows the evaluation of e.g. various helicity combinations, contributions of a Z boson and the corresponding virtual photon, or replacing a polarization vector with its momentum to apply gauge tests (see Section 3.3.2). This is crucial to obtain a fast code.

The evaluation of the HexBox and PenBox contributions (see Fig. 3.7) involves standard matrix elements of the type

$$\mathrm{SM}_{i,\pm,\pm} = \bar{u}(p_3)\Gamma^{\mu_1\cdots\mu_n} P_{L,R} u(p_1) \otimes \bar{u}(p_4)\Gamma_{\mu_1\ldots\mu_n} P_{L,R} u(p_2), \tag{3.33}$$

where Γ represents a chain of γ-matrices and n matrices γ^{μ_i} have to be contracted with the corresponding matrix in the second spinor chain. The numerical evaluation of these tensor contractions is very time consuming and Chisholm identities [97], such as

$$\gamma^{\mu_1}\gamma^{\mu_2}\gamma^{\mu_3} P_{L,R} \otimes \gamma_{\mu_1}\gamma_{\mu_2}\gamma_{\mu_3} P_{L,R} = 16\gamma^{\mu_1} P_{L,R} \otimes \gamma_{\mu_1} P_{L,R} \tag{3.34}$$

and

$$\gamma^{\alpha}\gamma^{\beta}\gamma^{\mu_1} P_{L,R} \otimes \gamma_{\mu_1} P_{L,R} = \gamma^{\mu_1} P_{L,R} \otimes \gamma^{\beta}\gamma^{\alpha}\gamma_{\mu_1} P_{L,R} \tag{3.35}$$

can be used to simplify this expressions. As an example, one obtains

$$\begin{aligned}
&\bar{u}(p_3)\gamma^{\mu_1}\gamma^{\mu_2}\gamma^{\mu_3} P_{L,R} u(p_1) \otimes \bar{u}(p_4)\not{\epsilon}_5\not{p}_3\gamma_{\mu_1}\gamma_{\mu_2}\gamma_{\mu_3} P_{L,R} u(p_2) \\
&= 16\,\bar{u}(p_3)\gamma^{\mu_1} P_{L,R} u(p_1) \otimes \bar{u}(p_4)\not{\epsilon}_5\not{p}_3\gamma_{\mu_1} P_{L,R} u(p_2) \\
&= 16\,\bar{u}(p_3)\not{p}_3\not{\epsilon}_5\gamma^{\mu_1} P_{L,R} u(p_1) \otimes \bar{u}(p_4)\gamma_{\mu_1} P_{L,R} u(p_2) \\
&= 0,
\end{aligned} \tag{3.36}$$

where in the last step the Dirac equation for particle 3 has been applied. Therefore, the corresponding standard matrix element involving a rank three tensor contraction does not have to be evaluated.

3.3.2. Gauge Tests and Rescue System

The reduction of tensor one-loop integrals into scalar integrals involves the evaluation of determinants, that occur in denominators. In some phase space regions, large numerical cancellations appear leading to bad numerical accuracy if the determinants are small. Especially the inverse Gram determinants appearing in the reduction formalism of Ref. [90] can lead to numerical instabilities, but also the Cayley determinants appearing in Ref. [91] can be problematic. It is therefore necessary to identify these instabilities and to treat the corresponding contributions separately to obtain more stable results.

The strategy used here is to identify instabilities using "gauge tests" that are obtained by replacing polarization vectors by their four-momenta,

$$\varepsilon^\mu(p) \to p^\mu. \tag{3.37}$$

These replacements lead to exact algebraic relations between various Feynman diagrams and evaluating these allows to estimate the numerical accuracy of the contributions. As has been explained earlier, the building blocks can be reevaluated using the above replacement with only a minor increase in computing time. This method has also been used for all other processes implemented in VBFNLO. However, in contrast to most other processes, where the phase space point is discarded if a gauge test fails, a "rescue system" is called, which reevaluates the tensor and scalar integrals of the corresponding building block with quadruple precision. If the results obtained with this method still fail the gauge test, the amplitude is set to zero and the phase space point is discarded.

There are two types of gauge tests that can be constructed. The first one relates N-point functions with a difference of two $(N-1)$-point functions as shown in the following for a box diagram for simplicity. The diagram in the left of Fig. 3.9 can be written as

$$\varepsilon_2^\mu \varepsilon_3^\nu \mathcal{M}_{\mu\nu} \propto \varepsilon_2^\mu \varepsilon_3^\nu \int \frac{\mathrm{d}^d q}{(2\pi)^d} \frac{1}{q^2}\, \bar{u}(p_4)\gamma^\alpha \frac{1}{\not{q}_3}\gamma_\nu \frac{1}{\not{q}_2}\gamma_\mu \frac{1}{\not{q}_1}\gamma_\alpha u(p_1), \tag{3.38}$$

where the convention

$$q_i = q + \sum_{j=1}^{i} p_j \tag{3.39}$$

is used to add the external momenta p_j to the loop momentum q. Applying the replacement $\varepsilon_2 \to p_2$ in Eq. (3.38), one obtains

$$\begin{aligned} p_2^\mu \varepsilon_3^\nu \mathcal{M}_{\mu\nu} &\propto p_2^\mu \varepsilon_3^\nu \int \frac{\mathrm{d}^d q}{(2\pi)^d} \frac{1}{q^2}\, \bar{u}(p_4)\gamma^\alpha \frac{1}{\not{q}_3}\gamma_\nu \frac{1}{\not{q}_2}\gamma_\mu \frac{1}{\not{q}_1}\gamma_\alpha u(p_1) \\ &= \varepsilon_3^\nu \int \frac{\mathrm{d}^d q}{(2\pi)^d} \frac{1}{q^2}\, \bar{u}(p_4)\gamma^\alpha \frac{1}{\not{q}_3}\gamma_\nu \frac{1}{\not{q}_2}(\not{q}_2 - \not{q}_1)\frac{1}{\not{q}_1}\gamma_\alpha u(p_1) \\ &= \varepsilon_3^\nu \int \frac{\mathrm{d}^d q}{(2\pi)^d} \frac{1}{q^2} \left(\bar{u}(p_4)\gamma^\alpha \frac{1}{\not{q}_3}\gamma_\nu \frac{1}{\not{q}_1}\gamma_\alpha u(p_1) - \bar{u}(p_4)\gamma^\alpha \frac{1}{\not{q}_3}\gamma_\nu \frac{1}{\not{q}_2}\gamma_\alpha u(p_1) \right). \end{aligned} \tag{3.40}$$

This corresponds to a difference of two three-point functions, where the momentum of the removed particle 2 is added to the adjacent particles 3 or 1, respectively. The accuracy

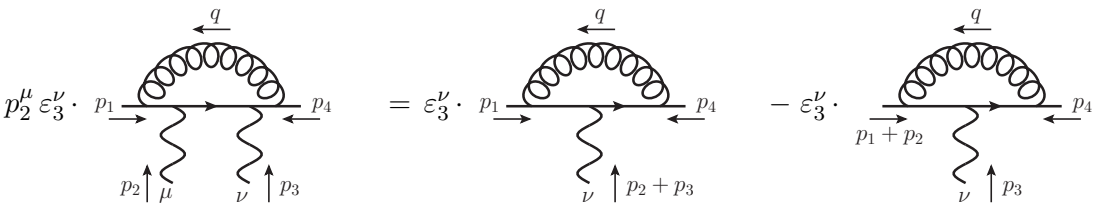

Figure 3.9.: Replacing the polarization vector ε_2 of the box diagram with the corresponding momentum p_2 leads to a difference of two vertex diagrams.

of the box diagram can be estimated by evaluating the above expressions numerically and calculating

$$\text{GaugeTestResult} = \frac{\mathcal{M}^{\text{box}} - \mathcal{M}^{\text{vert,1}} + \mathcal{M}^{\text{vert,2}}}{\max(|\mathcal{M}^{\text{box}}|, |\mathcal{M}^{\text{vert,1}}|, |\mathcal{M}^{\text{vert,2}}|)}, \tag{3.41}$$

where the individual contributions correspond to the terms in Eq. (3.40). The normalization with the maximum of the individual contributions is done to obtain a dimensionless quantity[§].

The second method for the construction of gauge tests explicitly uses the gauge invariance of the amplitudes. After the replacement of Eq. (3.37), the sum of all diagrams belonging to the same gauge invariant subset is zero. Therefore, one can evaluate the building blocks for different permutations of the external vector bosons and apply a test similar to Eq. (3.41). To obtain small gauge invariant sets of diagrams, one can assume that the vector bosons belong to different $U(1)$ gauge groups[¶]. Then it is enough to permute the current that has been replaced by its momentum to all positions, while keeping the order of the other particles fixed.

At least one of the above tests is applied to all diagrams to estimate the accuracy of the result. If the GaugeTestResult is larger than a fixed limit, typically set to 0.01, the rescue system is called to evaluate the corresponding contributions with higher numerical accuracy. Knowing that the numerical problems typically arise in the tensor reduction of the one-loop integrals, only the scalar and tensor integrals are reevaluated with quadruple precision. To achieve an improvement, one has to convert the momenta of the particles, which are given in double precision, to quadruple precision. To ensure that the condition $p^2 = 0$ is fulfilled with quadruple precision for massless on-shell particles, the energy of these particles has to be reevaluated using $p_0 = |\vec{p}|$. Similarly, the four-momentum of one off-shell particle has to be reevaluated from the other momenta to ensure momentum conservation being fulfilled with quadruple precision. The results of the building block and the gauge test are then reevaluated with the tensor reduction being performed in quadruple precision. If the gauge test still indicates numerical instabilities, the complete amplitude is set to zero to avoid incomplete gauge cancellations of the other contributions to the amplitude. As shown in Fig. 3.10, the error due to neglecting these points is well below the per mill level, if the limit to the GaugeTestReuslt is chosen to be in the range $[10^{-3}; 10^{-1}]$.

3.3.3. Implementation of the Amplitudes

Using the building blocks defined in Section 3.3.1 with different permutations and combinations of external currents, the amplitudes can be constructed. As for the Born and real

[§]If the denominator of Eq. (3.41) is zero, one has to set GaugeTestResult = 0.

[¶]This is possible, since the coupling constants are not included in the building blocks.

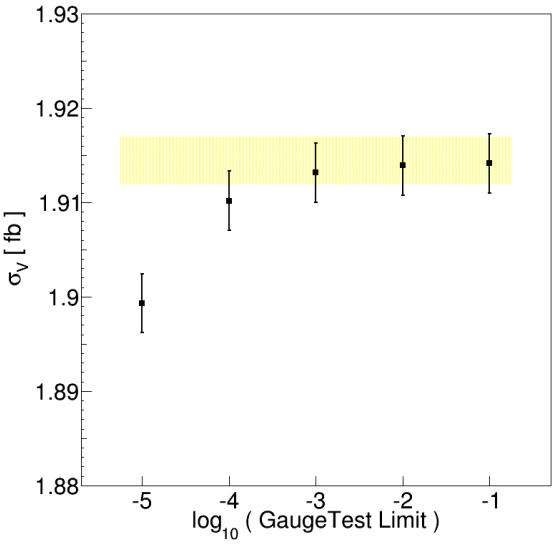

Figure 3.10.: Dependence of the virtual contribution on the limit to the GaugeTestResult. The reults are obtained using the cuts and input parameters presented in Section 4.2 and using the same phase space points for the individual results. The yellow band with a width of $0.001 \cdot \sigma^{NLO}$ is shown for comparison.

emission contributions, the EW coupling constants of the vector bosons to the fermions are already included in the effective currents, thereby combining contributions of a Z boson and the corresponding virtual photon. Only for the fermion loop diagrams the Z and γ^* contributions have to be separated and the EW coupling constants are provided as inputs to the building blocks. In the evaluation of the scalar integrals, which appear in the calculation of the one-loop diagrams, the common factor

$$F = \frac{1}{16\pi^2}\,\mu^{-2\varepsilon}\,\Gamma(1+\varepsilon)\,(4\pi)^{\varepsilon} = \frac{1}{16\pi^2}\,\mu^{-2\varepsilon}\,S_{\varepsilon} \tag{3.42}$$

is dropped, where μ is the arbitrary mass parameter of the dimensional regularization. To obtain the full one-loop matrix element $\mathcal{M}_{\text{1-loop}}$, the results of all building blocks, denoted as $\mathcal{M}'_{\text{1-loop}}$, have to be summed and multiplied with the above factor as well as the proper power of the strong coupling constants g_s^0,

$$\mathcal{M}_{\text{1-loop}} = (g_s^0)^4 \cdot F \cdot \mathcal{M}'_{\text{1-loop}}. \tag{3.43}$$

To obtain $\mathcal{M}'_{\text{1-loop}}$, the results of the individual building blocks are added up, separating them into the basic color structures. For the 4-quark processes these are the same as for the Born amplitudes, $\mathcal{C}_t$ and $\mathcal{C}_u$. However, compared to the Born amplitude there is no one-to-one relationship between the color structures and the s- and t-channel diagrams. The 2-quark-2-gluon amplitudes involve a new color structure $\mathcal{C}_3 = \delta^{ab}\mathbb{1}$ as well as those of the Born amplitude, $\mathcal{C}_1$ and $\mathcal{C}_2$.

Figures 3.11 and 3.12 show how the full virtual amplitudes of the 2-quark-2-gluon and 4-quark subprocesses can be constructed. The individual building blocks appearing there have to be called for the various permutations of external vector bosons. As for the Born and real emission contributions, the summation over the lepton and photon helicities is done using a random phase as described in Section 3.1. Furthermore, a full summation over parton helicities is applied for the 4-quark subprocesses, making use of the efficient caching system of the building blocks. For the 2-quark-2-gluon subprocesses the amplitudes are calculated with fixed parton helicities using the simple random helicity summation. Based on the additional computing time of the building blocks for evaluating additional helicity configurations and the runtime of the LO processes, it has been estimated that both methods for the helicity summation would lead to a similar runtime of the Monte Carlo integration.

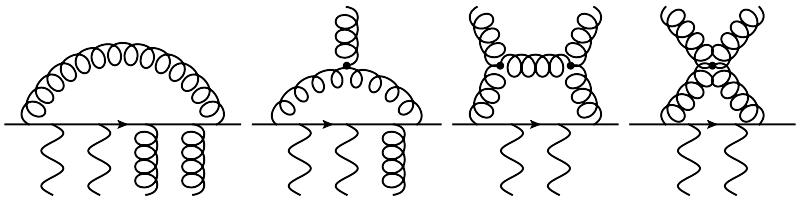

(1) HexLine contributions.

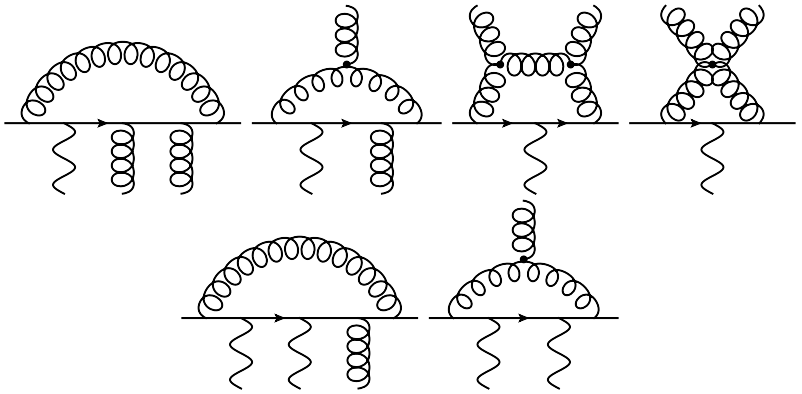

(2) PenLine contributions. In the first row, the EW vector boson is the current $\tilde{V}$. The external gluon in the second row is the off-shell current g^*.

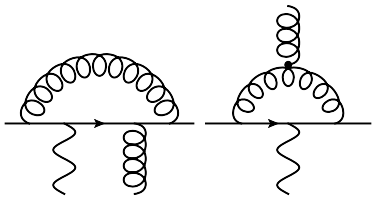

(3) BoxLine contributions. The external vector bosons are the currents $\tilde{V}$ and g^*.

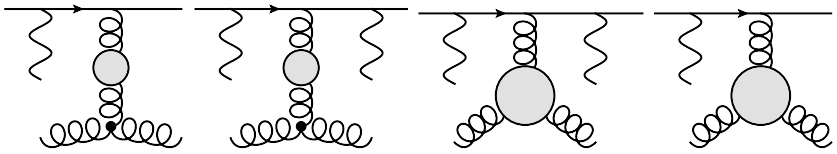

(4) Self energy and vertex corrections. The circles represent all quark, gluon and ghost contributions.

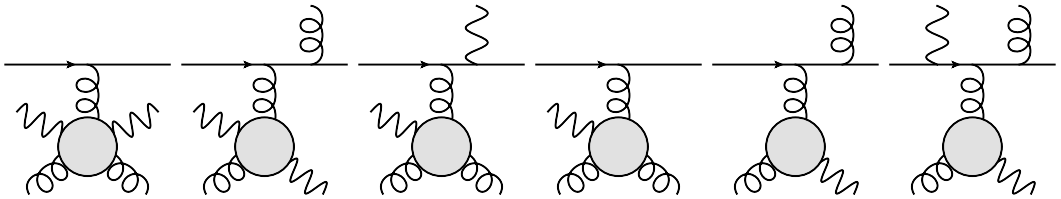

(5) Additional fermion loop contributions. The first and second diagram only appear in the calculation of $ZZjj$ and include the contribution of a Higgs boson, which is coupled to a top loop and decays into the Z boson pair. Furthermore, for the diagrams with three gluons being attached to the loop, there are additional contributions with a three-gluon vertex outside the loop.

Figure 3.11.: Topologies appearing in the 2-quark-2-gluon amplitudes. The Feynman diagrams represent the corresponding building block. These have to be called with all permutations of the external vector bosons.

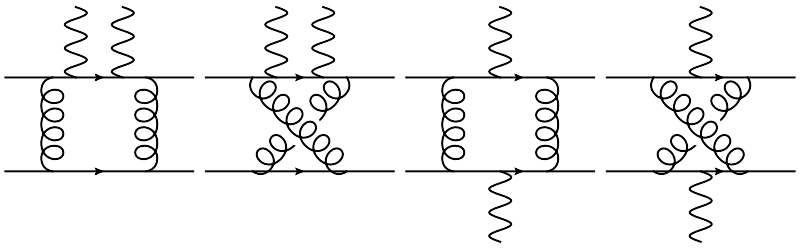

(1) HexBox contributions.

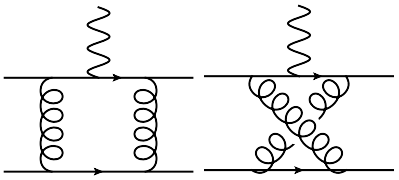

(2) PenBox contributions with the external current $\tilde{V}$.

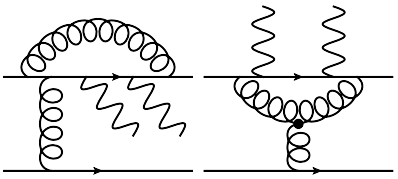

(3) PenLine contributions.

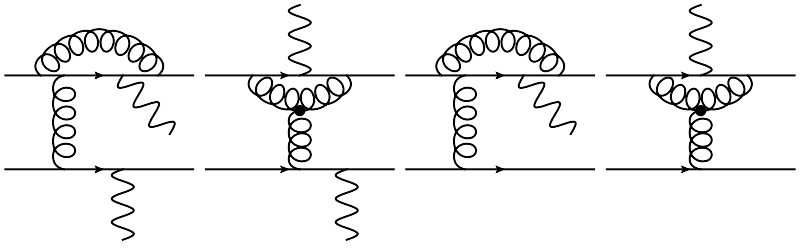

(4) BoxLine contributions. The current $\tilde{V}$ has to be used in diagrams 3 and 4.

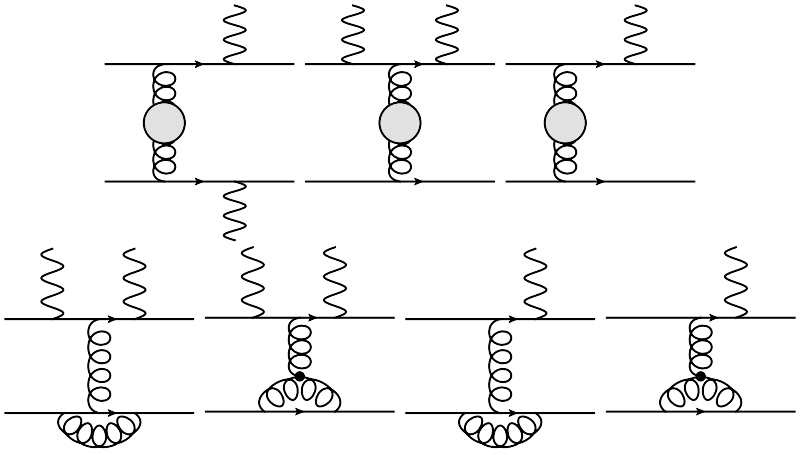

(5) Self energy and vertex corrections.

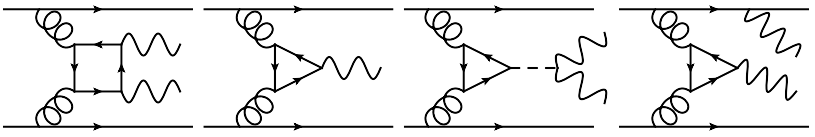

(6) Additional fermion loop contributions. Diagrams 1-3 only contribute to $ZZjj$ production.

Figure 3.12.: Topologies appearing in the 4-quark amplitudes where the Feynman diagrams represent the corresponding building block. These have to be called with all permutations of the external vector bosons. For $W^{\pm}W^{\pm}jj$ production only the contributions with one EW gauge boson being coupled to each external quark line contribute.

To obtain UV finite amplitudes, the quark and gluon fields as well as the strong coupling constant have to be renormalized as explained in Section 2.2.3. For the sum of Born and one-loop matrix elements, one obtains

$$\begin{aligned}\mathcal{M}^r_{\text{Born}} + \mathcal{M}^r_{\text{1-loop}} &= (g_s^0)^2 \left(\mathcal{M}_{\text{Born}} + (g_s^0)^2 F \mathcal{M}'_{\text{1-loop}}\right) \cdot Z_{WF} \\ &= (g_s^{\text{r}})^2 \mu^{2\varepsilon} Z_g^2 \left(\mathcal{M}_{\text{Born}} + \frac{\alpha_s}{4\pi} Z_g^2 S_\varepsilon \mathcal{M}'_{\text{1-loop}}\right) \cdot Z_{WF} \\ &= (g_s^{\text{r}})^2 \mu^{2\varepsilon} \left(\mathcal{M}_{\text{Born}}(1 + 2\,\delta Z_g + \delta Z_{WF}) + \frac{\alpha_s}{4\pi} S_\varepsilon \mathcal{M}'_{\text{1-loop}} + \mathcal{O}(\alpha^2)\right),\end{aligned} \tag{3.44}$$

where an index r indicates renormalized quantities and the strong coupling constants of the unrenormalized matrix elements have been written explicitly. In the second line, the relation between the bare and renormalized coupling constant (see Eq. (2.41)) has been used.

The factor Z_{WF} represents the wave function renormalization constants of the external fields. For the 2-quark-2-gluon subprocesses, it is

$$Z_{WF} = 1 + \delta Z_q + \delta Z_A \tag{3.45}$$

and the UV counter terms can be written as [69]

$$\begin{aligned}\mathcal{M}^{\text{2q2g}}_{ct} &= \mathcal{M}_{\text{Born}} \left(2\,\delta Z_g + \delta Z_q + \delta Z_A\right) \\ &= -\mathcal{M}_{\text{Born}} \frac{\alpha_s}{4\pi} S_\varepsilon \beta_0 \frac{1}{\varepsilon} \left(\frac{\mu^2}{\mu_R^2}\right)^\varepsilon \\ &= -\mathcal{M}_{\text{Born}} \frac{\alpha_s}{4\pi} S_\varepsilon \beta_0 \left(\frac{1}{\varepsilon} + \ln\frac{\mu^2}{\mu_R^2} + \mathcal{O}(\varepsilon)\right) \\ &= -\mathcal{M}_{\text{Born}} \frac{\alpha_s}{4\pi} \beta_0 \left(\frac{1}{\varepsilon} - \gamma_E + \ln 4\pi + \ln\frac{\mu^2}{\mu_R^2} + \mathcal{O}(\varepsilon)\right).\end{aligned} \tag{3.46}$$

Since the factor S_ε can be factored out in the one-loop contributions as well as in the counter terms, the expression in the third line of Eq. (3.46) is used in the implementation.

Similarly, one obtains for the 4-quark amplitudes

$$Z_{WF} = 1 + 2\,\delta Z_q \tag{3.47}$$

and

$$\begin{aligned}\mathcal{M}^{\text{4q}}_{ct} &= \mathcal{M}_{\text{Born}} \left(2\,\delta Z_g + 2\,\delta Z_q Z_A\right) \\ &= \mathcal{M}_{\text{Born}} \frac{\alpha_s}{4\pi} S_\varepsilon\, 2 \frac{1}{\varepsilon} \left[-\frac{\beta_0}{2} \left(\frac{\mu^2}{\mu_R^2}\right)^\varepsilon + \frac{2}{3} T_R \left(\frac{\mu^2}{m_t^2}\right)^\varepsilon\right] \\ &= \mathcal{M}_{\text{Born}} \frac{\alpha_s}{4\pi} S_\varepsilon\, 2 \left[\left(-\frac{\beta_0}{2} + \frac{2}{3} T_R\right) \frac{1}{\varepsilon} - \frac{\beta_0}{2} \ln\frac{\mu^2}{\mu_R^2} + \frac{2}{3} T_R \ln\frac{\mu^2}{m_t^2} + \mathcal{O}(\varepsilon)\right].\end{aligned} \tag{3.48}$$

After summing up the results of the one-loop diagrams and including the counter terms, the renormalized one-loop matrix element can be interfered with the Born contribution to obtain

$$\mathrm{d}\sigma^V = 2\,\text{Re}(\mathcal{M}^*_{\text{Born}} \mathcal{M}_{\text{1-loop}}), \tag{3.49}$$

where the multiplication of the color structures can be done as in Section 3.1. Note that Eq. (3.49) still contains IR singularities and S_ε as defined in Eq. (3.44) is factored out.

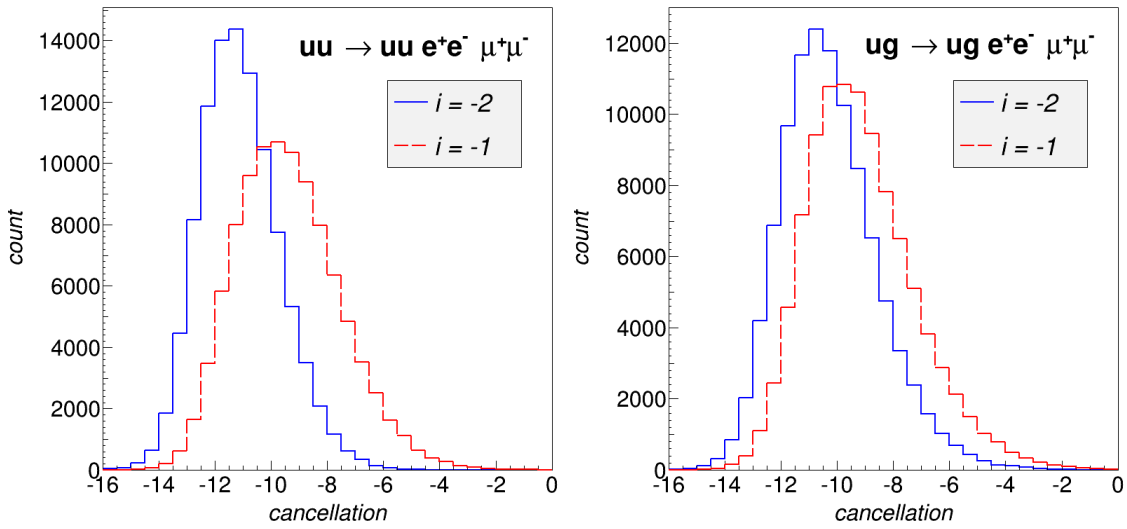

Figure 3.13.: Cancellation of the ε^i poles for the subprocesses $uu \to uu\, e^+e^-\, \mu^+\mu^-$ and $ug \to ug\, e^+e^-\, \mu^+\mu^-$ using 10^5 phase space points. The amplitudes are evaluated with double precision and the cancellation is defined as $\log_{10}(\mathrm{d}\sigma^V + \mathrm{d}\sigma^A)/\mathrm{d}\sigma^A$.

To cancel the IR singularities the contribution of the $\mathbf{I}$ operator

$$\mathrm{d}\sigma^A = \mathbf{I} \otimes \mathrm{d}\sigma^B, \tag{3.50}$$

which results from the integration of the dipoles [68], has to be added to the virtual amplitude. The operator $\mathbf{I}$ can be written as

$$\mathbf{I} = -\frac{\alpha_s}{2\pi} S_\varepsilon \sum_i \frac{1}{\mathbf{T}_i^2} \left[\mathbf{T}_i^2 \left(\frac{1}{\varepsilon^2} - \frac{\pi^2}{2} \right) + \gamma_i \frac{1}{\varepsilon} + \gamma_i + K_i + \mathcal{O}(\varepsilon) \right] \sum_{j \neq i} \mathbf{T}_i\, \mathbf{T}_j \left(\frac{\mu^2}{2\, p_i \cdot p_j} \right)^\varepsilon \tag{3.51}$$

with

$$\gamma_q = \frac{3}{2} C_F, \qquad \gamma_g = \frac{11}{6} C_A - \frac{2}{3} N_F T_R, \tag{3.52}$$

$$K_q = \left(\frac{7}{2} - \frac{\pi^2}{6} \right) C_F, \qquad K_g = \left(\frac{67}{18} - \frac{\pi^2}{6} \right) C_A - \frac{10}{9} N_F T_R. \tag{3.53}$$

Note the minor differences in the two round brackets of Eq. (3.51) compared to Ref. [68], that result from factoring out S_ε. For the implementation of this contribution, a `Mathematica` file has been created that expresses the color correlations $\langle \mathcal{M}_{\mathrm{Born}} | \mathbf{T}_i \mathbf{T}_j | \mathcal{M}_{\mathrm{Born}} \rangle$ in terms of Born contributions to the basic color structures. Furthermore, the series expansion in ε is calculated and a FORTRAN code for the evaluation of the ε^{-2} and ε^{-1} poles as well as the finite contributions is generated.

After summing the contributions $\mathrm{d}\sigma^V$ and $\mathrm{d}\sigma^A$, the result is independent on the arbitrary mass scale μ of dimensional regularization and the poles in ε cancel, which has been checked numerically. The cancellation of the poles appearing in Eqs. (3.49) and (3.50) is shown in Fig. 3.13. Using double precision arithmetics, a cancellation of about 10 decimal digits is observed for the bulk of phase space points. However, for a few per mill of the phase space points the agreement is worse than 2 digits. This is due to instabilities in the tensor reduction and shows that a rescue system, as the one described in Section 3.3.2, is needed. After the cancellation of all poles, the limit $\varepsilon \to 0$ can be applied. Therefore, the factor S_ε which has been factored out in all contributions becomes 1.

3.4. Finite Collinear Remainder

The remaining collinear divergences stemming from initial-state parton splittings can be factorized into a redefinition of the parton distribution functions. After the divergences have been canceled, the additional finite parts, can be written as [68]

$$\begin{aligned}\mathrm{d}\sigma_{ab}^{C,\mathrm{fin}} = \int_0^1 \mathrm{d}x \Bigg[&\sum_{a'} \left(\mathbf{K}(x) + \mathbf{P}(x, xp_a, \{p\}, \mu_F^2)\right)^{aa'} \otimes \mathrm{d}\sigma_{a'b\to X}^{B}(xp_a, p_b) \\ &+ \sum_{b'} \left(\mathbf{K}(x) + \mathbf{P}(x, xp_b, \{p\}, \mu_F^2)\right)^{bb'} \otimes \mathrm{d}\sigma_{ab'\to X}^{B}(p_a, xp_b) \Bigg].\end{aligned} \tag{3.54}$$

These contributions have to be convoluted with the parton density functions $f_a(x_a, \mu_F^2)$ and $f_b(x_b, \mu_F^2)$ and integrated over the phase space of the corresponding Born process.

In the following, only the contribution of the first line of Eq. (3.54), denoted as $\mathrm{d}\sigma_{a'b}^{C}$, will be considered, which results from collinear splittings of a parton a into the parton a' entering the hard matrix element, and an additional unobserved parton as illustrated by the following figure.

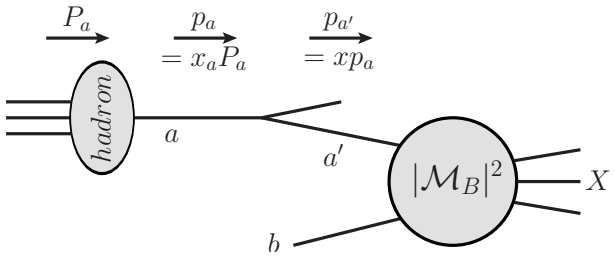

The methods used here closely follow the description of Refs. [34, 98, 99] and can be similarly applied to obtain the second contribution $\mathrm{d}\sigma_{ab'}^{C}$. Including the parton density function of particle a, one obtains

$$\begin{aligned}&\int_0^1 \mathrm{d}x_a f_a(x_a, \mu_F^2) \mathrm{d}\sigma_{ab}^{C,\mathrm{fin}} = \\ &\qquad \int_0^1 \mathrm{d}z \int_z^1 \frac{\mathrm{d}x}{x} \sum_{a'} f_a\left(\frac{z}{x}\right) \left(\mathbf{K}(x) + \mathbf{P}(x, p_{a'}, \{p\}, \mu_F^2)\right)^{aa'} \otimes \mathrm{d}\sigma_{a'b\to X}^{B}(p_{a'}, p_b),\end{aligned} \tag{3.55}$$

where the substitution $z = x\, x_a$ has been applied to rewrite all momenta in terms of the corresponding Born phase space with incoming momenta $p_{a'} = zP_a$ and $p_b = x_b P_b$.

The further evaluation leads to lengthy expressions and requires the proper treatment of the non-trivial color-correlations between the operators $\mathbf{K}$ and $\mathbf{P}$ with the Born matrix elements. However, the result can be written in the compact form

$$\begin{aligned}&\int_0^1 \mathrm{d}x_a f_a(x_a, \mu_F^2) \mathrm{d}\sigma_{a'b}^{C,\mathrm{fin}} = \frac{\alpha_s}{2\pi} \cdot \int_0^1 \mathrm{d}z \sum_{a'} \\ &\left[f_a(z, \mu_F^2) \delta^{aa'} \mathcal{A}^a + \int_z^1 \frac{\mathrm{d}x}{x} \left(f_a\left(\frac{z}{x}, \mu_F^2\right) - x f_a(z, \mu_F^2) \right) \delta^{aa'} \mathcal{B}^a + f_a\left(\frac{z}{x}, \mu_F^2\right) \mathcal{C}^{aa'} \right].\end{aligned} \tag{3.56}$$

The coefficients $\mathcal{A}^a$, $\mathcal{B}^a$ and $\mathcal{C}^{aa'}$ are given in Appendix B, which also lists integrals of the plus-distribution needed for the calculation of the coefficients. It is convenient to organize the summation over subprocesses in terms of the Born configurations appearing in the finite collinear terms. For a Born level subprocess $a'b \to X$, the flavor of the coefficients

$\mathcal{A}^a$ and $\mathcal{B}^a$ and the corresponding parton density function is fixed. For a' being a quark of flavor f, the last contribution of Eq. (3.56) is

$$\frac{\alpha_s}{2\pi} \cdot \int_0^1 \mathrm{d}z \int_z^1 \mathrm{d}x \left[f_{q_f}\left(\frac{z}{x}, \mu_F^2\right) \mathcal{C}^{qq} + f_g\left(\frac{z}{x}, \mu_F^2\right) \mathcal{C}^{gq} \right]. \tag{3.57}$$

The corresponding expression for a' being a gluon is

$$\frac{\alpha_s}{2\pi} \cdot \int_0^1 \mathrm{d}z \int_z^1 \mathrm{d}x \left[f_g\left(\frac{z}{x}, \mu_F^2\right) \mathcal{C}^{gg} + \sum_f f_{q_f}\left(\frac{z}{x}, \mu_F^2\right) \mathcal{C}^{qg} \right], \tag{3.58}$$

where the sum includes all massless quarks and anti-quarks. The color correlated matrix elements appearing in the coefficients $\mathcal{A}^a$, $\mathcal{B}^a$ and $\mathcal{C}^{aa'}$ can be evaluated using the routines `ColCorrME2q2g` and `ColCorrME4q` (see Section 3.2).

Differently from the other processes implemented in `VBFNLO`, the integration of the finite collinear terms is done using the phase space generator of the Born contribution. This not only allows to reuse large parts of the code for the summation over subprocesses, but also the adapted grid files generated during the Monte Carlo integration of the Born contribution can be reused. For the additional x integration, an additional random number $x_i \in [z; 1]$ is generated for each phase space point[‖].

3.5. Further Checks

In addition to the checks mentioned in the previous sections, further tests have been done at the level of individual phase space points and on the level of integrated cross sections.

In particular, all parts of the calculation have been checked by comparison with an independent calculation, which was done by another member of the collaboration. There, the tree-level amplitudes were calculated using `HELAS` [77] routines. `FeynArts-3.4` [100] and `FormCalc-6.2` [101] were used to obtain the virtual amplitudes. An inhouse loop library `LoopInts` [102] is used to calculate the scalar and tensor integrals of up to rank 5 hexagons. The two implementations have been compared at individual phase space points and full agreement of all Born and virtual amplitudes has been found for all subprocesses. The virtual contribution typically agrees with 6-12 identical digits while it is 9-12 digits for the Born. Furthermore, the real emission contribution, including the subtraction terms, has been validated at individual phase space points. At the level of integrated cross sections, the LO contribution and the finite collinear remainder have been compared and agreement within the Monte-Carlo error has been found.

As a further test of the subtraction terms, these have been adapted using the method of Refs. [103, 104] to restrict the phase space integration of the subtraction terms to the infrared regions. This method was primarily introduced to reduce the number of dipoles that have to be evaluated at the individual phase space points. However, due to the efficient calculation of the dipole terms, as described in Section 3.2, no significant improvement of the runtime has been obtained and this method is therefore only used as an additional check. Varying the α parameter introduced in Refs. [103, 104], the contributions of the real emission and the **I**- and **K**-operator change by factors of $\mathcal{O}(1)$, while the total NLO cross section remains unmodified.

In addition, some contributions of the implementation have been validated by comparison with other programs. At the amplitude level, the squared matrix elements for all subprocess types have been compared with `MadGraph-4` [79]. The LO cross sections of all

[‖] This random number is not driven by the adaptive Monte Carlo algorithm.

		$W^\pm W^\pm jj$	$W^\pm Zjj$	$W^\pm \gamma jj$	$ZZjj$	
Virtual	4q-type	91 μs	3.4 ms	3.4 ms	6.7 ms	(29 ms)
Amplitude	2q2g-type	–	23 ms	23 ms	28 ms	(120 ms)
σ_{LO} (0.1% MC error)		12 min	7 min	9 min	12 min	
σ_{NLO} (1% MC error)		20 min	2.5 h	3 h	3.5 h	

Table 3.2.: Runtime** of the virtual amplitudes and cross section calculations with all contributions included. The runtime of the virtual amplitudes of the 4-quark type include the full summation over parton spins, whereas only one spin configuration is considered in the 2-quark-2-gluon amplitudes. For both types, only one spin configuration of the EW system is calculated. All configurations of the quark types are calculated as described in Section 3.1. The runtime of the virtual amplitude for $ZZjj$ production is split into the contribution without closed fermion loops, where at least one EW boson couples to the loop, and the additional time for evaluating these is shown in brackets. The cross sections are evaluated using the input parameters listed in Section 4.2.

processes under consideration, as well as the corresponding processes with an additional jet, i.e. QCD-induced $VVjjj$ production, have been validated against `Sherpa-1.4` [55] using the `Comix` [105] generator. Full agreement within an MC error of less than 0.1 % has been found. Furthermore, the implementations of $W^\pm Zjj$ and $ZZjj$ production have been adapted to allow the calculation of $W^\pm jj$ and Zjj production at NLO QCD, as well. For these processes, the real emission contribution, including the subtraction terms, agrees with `Sherpa` within an MC error of less than 0.3 %. Due to the substantial runtime, which is more than a factor of 100 larger using the latter program, this test has only been done with a precision better than 1% for the $VVjj$ production.

The full NLO results for Wjj production have been compared with `MCFM` [106, 107] and agreement at the per mill level has been found. Similarly, NLO results for $W^\pm W^\pm jj$ production have been validated against the implementation of Ref. [41, 42] into the `POWHEG-BOX` [108] framework and both results agree within a MC error of less than 0.5%.

3.6. Runtime and additional Optimizations

The runtime** for evaluating the virtual amplitudes and the calculation of total cross sections is listed in Table 3.2. It shows, that the runtime of the virtual amplitudes of the 2-quark-2-gluon processes is much larger than for the processes of the 4-quark type, even though the latter include the full summation over parton spins, whereas for the former only one spin configuration is considered. The amplitudes of the 2-quark-2-gluon type involve up to hexagon contributions of rank five, whereas the hexagons appearing in the 4-quark subprocesses are of maximally rank four. Furthermore, the use of Chisholm identities (see Section 3.3) allows to significantly simplify the HexBox and PenBox contributions appearing in the subprocesses of the 4-quark type.

The table also shows that the virtual amplitude of the $W^\pm W^\pm jj$ process is very fast in comparison to the other processes. This is due to the restriction, that the two W bosons have to couple to different quark lines due to electric charge conservation, which largely reduces the number of involved diagrams. In particular, there are no PenLine contributions, which for the other processes appear in the subprocesses of the 4-quark type. The implementation of the amplitudes for $W^\pm Zjj$ and $W^\pm \gamma jj$ production are the same, leading to the same runtimes. The runtime of the $ZZjj$ amplitudes are slightly

**All runtimes shown here are obtained on an Intel i5-3470 computer with one core and using the Intel-ifort version 12.1.0.

larger, since for $W^{\pm}Zjj$ and $W^{\pm}\gamma jj$ production the quark-types of one quark-line are fixed, whereas for $ZZjj$, all combinations have to be considered. In addition, the $ZZjj$ calculation involves closed fermion loops with both Z bosons being coupled to it. This leads to rank five pentagons in the 2-quark-2-gluon amplitude and rank four boxes in the 4-quark subprocesses, which require the summation over the various quarks in the fermion loop, including the massive top quark. In total, these fermion loop contributions are much slower than the other contributions of the virtual amplitude. Since they are a gauge-invariant set of diagrams, they can be calculated separately and due to their small contribution to the cross section, they can be calculated with a reduced number of phase space points as explained in the following.

The full cross section calculation involves many contributions that can be calculated separately. They can be split according to

- subprocess
- NLO contribution (σ^B, σ^V, σ^R, σ^C, additional fermion loops in $ZZjj$ production)
- phase space generator (only for $W^{\pm}\gamma jj$ production, see Section 2.2.4).

Calculating the Born contributions first allows to use the adapted grids of the Monte-Carlo integration for the contributions σ^C and σ^V, such that the time consuming virtual amplitudes are predominantly evaluated in the phase space regions with large contributions to the cross section. In contrast to the other contributions, the full sum over subprocesses is done for the real emission to make use of the caching system described earlier. The phase space integration of the other contributions is split into the various subprocess types according to the individual lines of Eqs. (3.15) and (3.19).

The Monte Carlo integration of a contribution i leads to a specific runtime t_i and estimate of the absolute error $\Delta\sigma_i$ for the integral, which are related by the relation $\Delta\sigma_i \sim t_i^{-1/2} \sim N_i^{-1/2}$, where N_i is the number of evaluated phase space points. Minimizing the total runtime

$$T = \sum_i t_i \tag{3.59}$$

of the full calculation, while keeping the combined error

$$\Delta\sigma = \sqrt{\sum_i \Delta\sigma_i^2} \tag{3.60}$$

fixed, leads to the condition

$$\frac{\Delta\sigma_1}{\Delta\sigma_i} \cdot \sqrt{\frac{t_i}{t_1}} = C_i \stackrel{!}{=} 1 \qquad \forall i, \tag{3.61}$$

where the first contribution is chosen as an arbitrary reference. The optimal number for phase space points for each contribution can be obtained by running all contributions once to obtain the coefficients C_i. Afterwards, the number of phase space points can be adjusted according to $N_i \to N_i/C_i$, such that the condition of Eq. (3.61) is fulfilled. Using this method, e.g. the computing intensive virtual amplitudes or subprocesses with a minor contribution to the total cross section are evaluated with a reduced number of phase space points. This is shown in Table 3.3, where the result of a run for the cross section calculation of $ZZjj$ production is split into individual subprocesses and contributions to the NLO cross section.

classification	contribution	σ_i [fb]	$\Delta\sigma_i$ [ab]	$\Delta\sigma_i/\sigma_i$ [%]	t_i	N_i/N_1	C_i
subprocess	$qg \to qg$	3.002	7.84	0.26	6.8 h	1	1.00
	$\bar{q}g \to \bar{q}g$	1.468	4.27	0.29	3.4 h	2^{-1}	1.29
	$q\bar{q} \to gg$	1.594	4.03	0.25	4.2 h	2^{-1}	1.53
	$gg \to q\bar{q}$	0.364	1.59	0.44	34 min	2^{-3}	1.44
	$qq \to qq$	0.511	1.90	0.37	59 min	1	1.57
	$q\bar{q} \to q\bar{q}$	0.628	2.08	0.33	57 min	2^{-1}	1.41
	$\bar{q}\bar{q} \to \bar{q}\bar{q}$	0.083	0.77	0.93	8.2 min	2^{-3}	1.45
NLO contribution	σ^B	4.182	1.83	0.04	57 min	1	1.00
	σ^V (no QL)	1.916	9.50	0.50	13.3 h	2^{-5}	0.75
	σ^C	1.561	1.27	0.08	52 min	2^{-1}	1.16
	σ^V (QL)	-0.009	3.44	39.5	2.3 h	2^{-10}	0.86
	σ^R	-2.580	6.81	0.26	20 h	2^2	1.63
σ^{NLO}	all	5.070	12.39	0.24	37 h		

Table 3.3.: Cross section and runtime** of the program for $ZZjj$ production split into the various subprocess types and NLO contributions using optimized grids (see Section 2.2.4). The calculation of the virtual contributions is split into contributions of closed quark loops with at least one EW gauge boson being attached to the loop (QL) and the evaluation of all other one-loop diagrams. The factors C_i (defined in Eq. (3.61)) are close to one, which indicates that the number of phase space point N_i for all contributions i is close to the optimum value. The factor C_i for the real emission contribution is calculated with respect to all other contributions.

For $ZZjj$ production, the number of phase space points for the evaluation of the virtual contributions is reduced by a factor 2^5 compared to the corresponding Born level contribution. For the calculation of the very time consuming fermion loop contributions, which constitute less than 0.5% of the cross section, the number of phase space points is reduced by a further factor of 2^5. It has been checked that, using the adapted grids of the Born calculation, the error estimate for the Monte Carlo integration of this closed quark-loops is reliable, even though the relative error of this contribution can be close to 100%. For the various subprocesses, the number of evaluated phase space points varies within an factor of 2^5. The number of phase space points for the real emission contribution can be adjusted according to the combined error estimate and runtime of the other contributions.

With the optimizations presented here and in the previous sections, the calculation of LO and NLO cross sections is very fast, as shown in Table 3.2. The LO cross sections can be evaluated within a few minutes with per mill level accuracy. For $W^\pm W^\pm jj$ production, the calculation of the amplitudes only constitutes $\sim$ 10% of the calculation of the LO cross section and the increased runtime is probably due to a worse convergence of the phase space integration. The runtime of the NLO calculations shows that $W^\pm W^\pm jj$ production is very simple in comparison to the other processes, due to the limited number of contributing subprocesses and diagrams. The calculation of $W^\pm \gamma jj$ production is slightly slower than $W^\pm Zjj$ production, since the second phase space region where the three-body decay $W \to l\nu\gamma$ dominates is important and must be calculated separately. $ZZjj$ production, which involves many spin configurations and fermion loop contributions is the slowest process, with a runtime of $3.5h$ to obtain the NLO cross section with 1% accuracy.

CHAPTER 4

Phenomenological Results

4.1. Overview

In this chapter, the phenomenology of inclusive $VVjj + X$ production at the LHC will be discussed. The focus will be on the QCD-induced contributions of $\mathcal{O}(\alpha_s^2\alpha^2)$ for on-shell production, whose implementation has been presented in the previous chapter. In addition there are purely electroweak contributions of $\mathcal{O}(\alpha^4)$ as well as interferences between these two production mechanisms. Representative Feynman diagrams for the various contributions are shown in Fig. 4.1. The EW channel can be further split into "vector-boson-fusion" (VBF) processes, which include all diagrams with t- or u-channel EW gauge boson exchange between the two quark lines, and into s-channel contributions, that in particular include the production of three vector bosons, with one vector boson decaying into a quark-antiquark pair.

The phenomenology of the QCD-induced processes $W^\pm W^\pm jj$, $W^\pm Zjj$, $W^\pm \gamma jj$ and $ZZjj$ will be discussed in Sections 4.4-4.7. The corresponding results have been published in Refs. [44, 47–49]. Before studying the individual processes in detail, in the rest of this section, their relevance shall be discussed and an overview of the available calculations will be given. In Section 4.2, the input parameters as well as the phase space cuts used are defined. In Section 4.3, the scale dependence of the processes will be discussed. For processes with a W boson, the focus will be on the positively charged final states and it can be expected that, apart from the overall normalization due to different total cross sections, the results for the corresponding negatively charged final states are similar.

4.1.1. Importance of $VVjj$ Production in Particle Physics

Studying $VVjj$ production is an important part of the physics program at the LHC since it allows to probe the mechanism of EW symmetry breaking. In particular, the VBF contributions, including the $VV \to VV$ scattering, are sensitive to the self interactions of the EW gauge bosons. This scattering also includes contributions of the recently discovered Higgs boson [1, 2], which are needed to unitarize the amplitudes in the SM. In particular, the VBF processes $ZZjj$ and W^+W^-jj include Higgs production via $qq \to Hjj$ in VBF, with the Higgs decaying into ZZ or W^+W^-. The VBF mechanism is one of the most important Higgs production channels. It not only constitutes the second largest production

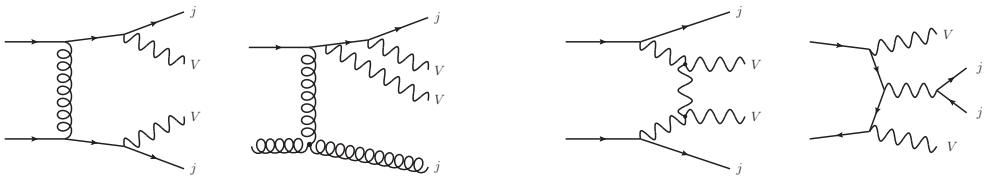

(1) QCD-induced contributions **(2)** EW contributions

Figure 4.1.: Representative Feynman diagrams for the QCD-induced and EW contributions to $VVjj$ production.

cross sections, but also features very characteristic signatures in detectors, which allow for an efficient background suppression. These signatures are common to all VBF processes and will be discussed in the following paragraph.

The VBF processes only include EW t- and u-channel exchange between two quark lines. The corresponding contributions peak at low virtualities of the exchanged vector bosons leading to a relatively small momentum transfer between the quark lines. Hence, the final state quarks lead to two jets in the far forward regions of the detector with a large rapidity separation and a large invariant mass, while their transverse momenta can be relatively small. The electroweak bosons are typically produced in the central region of the detector, with their decay products lying in the rapidity region between the two hardest jets. This characteristic signature of the VBF processes can be used to reduce large parts of the backgrounds, including the corresponding QCD-induced processes*. A second characteristic feature of the VBF processes is the suppression of additional jet activity in the central detector region: Due to the absence of color exchange between the two quark lines, additional gluon radiation predominantly appears in the vicinity of the final state quarks, similar to bremsstrahlung in QED. In contrast, the corresponding QCD-induced processes develop more radiation in the central region. A veto on events with additional jets in the central region can therefore be used to reduce the QCD-induced contributions. See e.g. Refs. [110, 111] for discussions of this central jet veto.

The characteristic signatures of the VBF processes allow for precision measurements of vector boson scattering and the Higgs boson. In the SM, these are determined by the EW symmetry group $SU(2) \otimes U(1)$ and the Higgs potential. Measurements of these processes therefore allow for a test of the fundamental structures of the SM. Even though the predictions made within the SM are in very good agreement with the experimental results obtained at collider experiments, physics beyond the standard model (BSM) could lead to, yet unobserved, modifications of the gauge boson self interactions. While modifications to the triple gauge couplings can be determined in the production of vector boson pairs, the determination of the quartic gauge couplings requires the measurement of vector boson scattering or the production of three EW gauge bosons. In addition, new heavy particles in models beyond the SM can manifest as resonances appearing in the invariant mass distribution of vector boson pairs. See e.g. Ref. [112] for a phenomenological discussion.

Besides the direct sensitivity of $VVjj$ production processes to BSM physics, they also constitute backgrounds to various other BSM searches. Most supersymmetric models obey the conservation of R-parity, which leads to cascade decays of SUSY particles into the lightest supersymmetric particle and additional SM particles. These cascades result in events with many leptons, jets and missing transverse momentum. Similar signatures can be obtained by the processes considered in this thesis, which is why they constitute an important background to BSM searches. A recent experimental analysis with this type of final states can be found in Ref. [113].

*see e.g. Ref. [109] and references therein.

In addition, the processes studied here are important to test double parton scattering, i.e. the simultaneous occurrence of two hard interactions (see e.g. Ref. [114] for a definition). To observe these, one typically looks for final states, which have a small production cross section when producing them in a single interaction, but can be produced by two interactions with significant cross sections as well. In this regard, a final state with two identically charged leptons and missing transverse energy is quite promising since in a single interaction it only can be produced by $W^{\pm}W^{\pm}jj$, which is suppresses by $\mathcal{O}(\alpha_s^2)$, compared to the production of two W bosons in different interactions [115–117]. Note that the $W^{\pm}W^{\pm}jj$ cross section is finite, even if the usual kinematic cuts on the two jets are not applied. Further backgrounds for double parton interactions are diboson production with undetected or misidentified leptons. Hence, the other processes discussed in this thesis can become important for double parton scattering, as well.

4.1.2. Available Calculations

Precise measurements in the EW sector, in $VVjj$ production processes for example, require precise theoretical predictions of these processes as well. The VBF contributions have been calculated to NLO accuracy in QCD in Refs. [22–26] for processes with all combinations of massive gauge bosons and in Ref. [27] for the production of a W boson in association with a real photon in the final state. Common to these calculations is that they neglect interferences between the t- and u-channel diagrams to avoid the calculation of up to eight-point one-loop integrals, when off-shell effects are included. This "VBF approximation" is justified, because the interferences are small if a large separation and invariant mass of the two hardest jets is demanded. The calculations of Refs. [22–25, 27] are publicly available in the flexible parton level Monte Carlo program VBFNLO [56–58]. This program also provides NLO QCD corrections to triboson production, which constitutes the EW s-channel contribution to $VVjj$ production. Details on the calculation of triboson production with full leptonic decay can be found in Refs. [28–34]. The corresponding processes with one vector boson decaying hadronically, leading to the final state $VVjj$, have recently been presented in Ref. [35] including all off-shell effects. In addition, NLO QCD corrections to on-shell production have been presented in Refs. [36–40] and in Ref. [39] NLO EW corrections to on-shell WWZ production have been discussed. Furthermore, the production of $W\gamma\gamma$ in association with one jet is known at NLO accuracy in QCD [81].

The calculation of the QCD-induced processes is more complicated, due to the contributions of up to six-point one-loop diagrams and non trivial color structures. However, these calculations have become possible in the last few years and results for basically all combinations of vector bosons are known with the exception of $Z\gamma jj$. Calculations for the production of $W^{\pm}W^{\pm}jj$ [41–44], $W^{+}W^{-}jj$ [45, 46], $W^{\pm}Zjj$ [47], $W^{\pm}\gamma jj$ [48], $ZZjj$ [49] and $\gamma\gamma jj$ [50, 51] have been presented. Furthermore photon pair production in association with three jets has been calculated in Ref. [51]. The missing $Z\gamma jj$ process can, in principle, be obtained with minor modifications from the $ZZjj$ calculation.

4.2. Selection Cuts and Input Parameters

To allow for a comparison of the individual processes, a common set of cuts and input parameters is used. For the final state leptons we demand

$$p_{Tl} > 20\,\text{GeV}, \quad |y_l| < 2.5, \quad R_{ll} > 0.4, \quad R_{jl} > 0.4, \tag{4.1}$$

where $R = \sqrt{(\Delta\phi)^2 + (\Delta y)^2}$ is the separation in the azimuthal angle – rapidity plane. The jets are clustered using the anti-k_T algorithm [118] with a cone radius $R = 0.4$ and they are required to fulfill

$$p_{Tj} > 20\,\text{GeV} \quad \text{and} \quad |y_j| < 4.5. \tag{4.2}$$

They are ordered in transverse momentum and the two hardest jets are sometimes refered to as tagging jets. For processes involving W bosons an additional cut on the missing transverse momentum of

$$\not{p}_T > 30\,\text{GeV} \tag{4.3}$$

is applied, which is defined by the momentum of the neutrino system. For photons, the isolation criterion proposed by Frixione [75] (see Section 2.2.5) is applied with separation parameter $\delta_0 = 0.7$. In addition, the following cuts are applied,

$$p_{T\gamma} > 30\,\text{GeV}, \quad |y_\gamma| < 2.5, \quad R_{l\gamma} > 0.4, \quad R_{j\gamma} > 0.7. \tag{4.4}$$

As EW input parameters, we use $M_W = 80.385\,\text{GeV}$, $M_Z = 91.1876\,\text{GeV}$ and $G_F = 1.16637 \times 10^{-5}\,\text{GeV}^{-2}$. From this, the weak mixing angle and the electromagnetic coupling constant are calculated using the standard model tree level relations

$$\cos\theta_W = \frac{M_W}{M_Z} \quad \text{and} \quad \alpha = \frac{\sqrt{2}}{\pi} G_F M_W^2 \sin^2\theta_W. \tag{4.5}$$

We use the MSTW2008 parton distribution functions [119] with $\alpha_s^{LO}(M_Z) = 0.13939$ and $\alpha_s^{NLO}(M_Z) = 0.12018$. All fermions, except for the top quark with $m_t = 173.1\,\text{GeV}$, are assumed massless. We use $\overline{MS}$ renormalization for the strong coupling constant and decouple the top quark from the running of α_s. The decay widths of the weak bosons are calculated to be $\Gamma_Z = 2.50890\,\text{GeV}$ and $\Gamma_W = 2.09761\,\text{GeV}$. The calculation for $ZZjj$ and of the EW contributions in Section 4.4 involve contributions of the Higgs boson with $M_H = 126\,\text{GeV}$ and $\Gamma_H = 4.195\,\text{MeV}$. All calculations are performed in the context of proton-proton collisions at the LHC with a center of mass energy of $\sqrt{s} = 14\,\text{TeV}$.

We present our results using three different choices of the renormalization and factorization scale. Since a fixed scale cannot represent all the kinematical configurations appearing in the calculation, dynamical scales are used, that take into account the momentum configuration at each phase space point. A common scale choice in multi-leg calculations is the total transverse energy of the event, and we therefore define

$$\mu_{HT} = \frac{1}{2}\left(\sum_{i\,\in\,\text{partons}} p_{Ti} + \sum_{V_i} E_{Ti}\right), \tag{4.6}$$

where the transverse energy is given by

$$E_T = \sqrt{p_T^2 + m^2}, \tag{4.7}$$

with m being the reconstructed mass of the particle[†]. In addition, the scale choices

$$\mu'_{HT} = \frac{1}{2}\left(\sum_{i\,\in\,\text{jets}} p_{Ti}\,\mathrm{e}^{\,|y_i - y_{12}|} + \sum_{V_i} E_{Ti}\right), \quad \text{with } y_{12} = \frac{1}{2}(y_1 + y_2), \tag{4.8}$$

and

$$\mu_{ET} = \frac{1}{2}\left(\,E_T(j_1 j_2) + E_T(V_1 V_2)\right) \tag{4.9}$$

are used, which take into account the invariant mass of the tagging jet system (see Section 4.3). Note that in the definition of μ_{HT} the sum of the transverse parton momenta is calculated, whereas for μ'_{HT} the corresponding sum is done for the jets to avoid large contributions by partons collinear to the beam. If not stated otherwise, the renormalization and factorization scales are set equal.

The results are obtained by simulating the decay of the vector bosons into a specific leptonic final state without identical leptons and are then multiplied by an appropriate factor to account for all possible combinations of leptons of the first and second generation. This is a factor of 4 for the $WZjj$ production and a factor of 2 for the other processes. The neglected Pauli interferences due to identical leptons in the final state are expected to be less than 0.1% (see e.g. [28] for a discussion of this effect for WWZ production).

4.3. Scale Dependence

Calculating cross sections for hadron collisions at a fixed order in perturbation theory leaves a dependence of the results on the unphysical renormalization and factorization scales. These dependences are canceled by higher order terms and therefore a variation of these scales can be used to estimate the size of the neglected contributions. However, this error estimate should not be considered as the true theoretical uncertainty since this variation does not affect all the higher order terms.

In this section, the scale dependence of the total cross sections is studied. The scales, as defined in Eqs. (4.6), (4.8) and (4.9), are multiplied by factors $\xi \in [1/10, 10]$. Fig. 4.2 shows the dependence of the cross sections on simultaneous variation of the factorization and renormalization scales as well as the dependence on varying the scales individually for the processes $W^+\gamma jj$ and W^+W^+jj using μ'_{HT} as the central scale. It is striking that the scale uncertainty is dominated by the dependence of the cross section on the renormalization scale. At LO this is determined by the running of α_s^2 and results in differences of about 40% for scale variations by a factor of two around the central value. The next-to-leading order corrections partly compensate the dependence of the LO results leading to a scale dependence that is typical for NLO calculations: For large values of μ_R, the smallness of α_s is compensated by positive corrections, whereas for small scales one obtains negative corrections. This leads to a significant reduction of the scale dependence in the NLO result, especially in the region close to the maximum.

For variations by a factor of 2 around the central value, the variation of the cross sections is reduced to 6% for $W^+\gamma jj$ and 17% for W^+W^+jj. The dependence on the factorization scale is rather small with variations of the LO (NLO) results by 3% (2%) for $W^+\gamma jj$ and 4% (1%) for W^+W^+jj. The larger scale dependence of W^+W^+jj production compared to the results of Ref. [41], where a dependence of less than 10% was obtained, is due to the different scales used. The latter results use fixed values for the scales, which are too low for the high transverse momentum and high invariant mass regions. When comparing the distributions in Section 4.4 with the ones presented in Ref. [41], it can be seen that the fixed scale leads to much larger uncertainties in those phase space regions.

[†]The reconstructed mass of a W bosons can be used in the calculation, even though it cannot be determined experimentally.

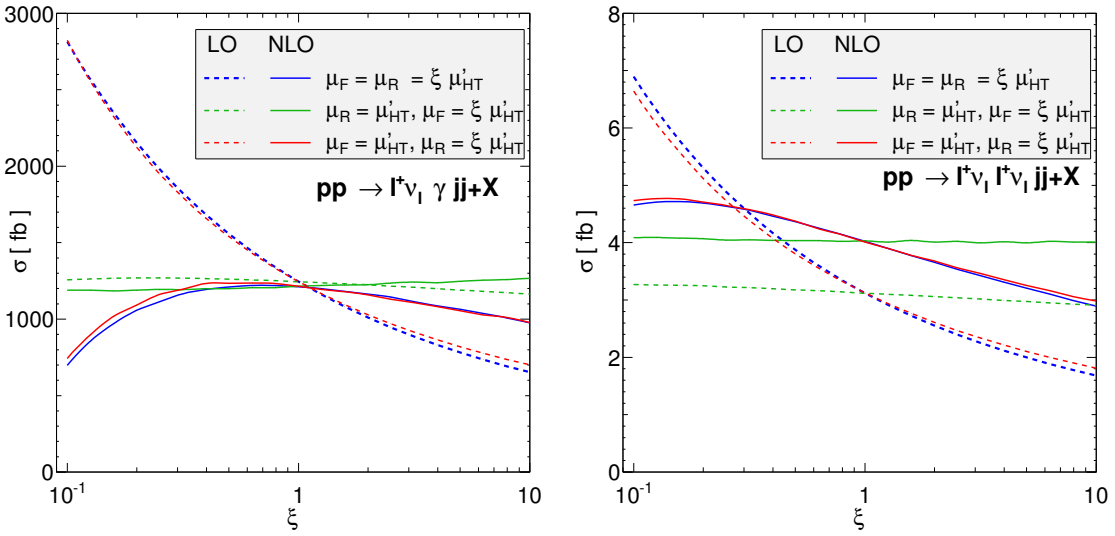

Figure 4.2.: Scale dependence of the total cross section for $W^{\pm}\gamma jj$ and $W^{\pm}W^{\pm}jj$ production processes at LO and NLO with μ'_{HT} as central scale. For both processes there is no visible dependence on the factorization scale and the simultaneous variation of both scales matches the dependence on the renormalization scale.

In the following, the factorization and renormalization scales will be set equal. The simultaneous variation of both scales is shown in Fig. 4.3 for the individual processes using the three scale definitions of Eqs. (4.6), (4.8) and (4.9) as central scale. Except for $W^{\pm}W^{\pm}jj$ production, which is special due to the absence of gluon induced processes at LO, all processes show a similar behavior in scale dependence. The appearance of new contributions at NLO often leads to large K-factors, which is defined as the ratio of the NLO and LO result. This large K-factors can be seen in e.g. diboson production [120–122] and Higgs boson production via gluon fusion [123, 124]. Also in $W^{\pm}W^{\pm}jj$ production a larger K-factor of 1.20-1.38 (depending on the scale choice) at $\xi = 1$ is observed, whereas for the other processes, the K-factor is close to one with corrections of less than 10% in most cases. However, one should keep in mind that there is a large scale dependence at LO and that this discussion depends on the definition of the central scale.

At leading order, the variations of the scales by a factor of two around the central values leads to differences in the cross sections of about 40-50% with respect to the central scale. This scale dependence is smallest for $W^{\pm}W^{\pm}jj$ production with differences of 42% for the scale choices μ'_{HT} and μ_{ET}. For $W^{\pm}\gamma jj$ and $ZZjj$ production, they are about 45% and the largest uncertainties of 49% are obtained for $W^{\pm}Zjj$ production using the scale choice μ_{HT}. The scale dependence is largely reduced after including the next-to-leading order corrections, which yields about 17-20% for $W^{\pm}W^{\pm}jj$ production and less than 10% for the other processes. A more conservative estimate of the scale uncertainties is obtained by combining the scale variations by a factor of two with the selection of the three different central scales. Using this method, scale uncertainties of 59-64% are obtained at LO. The NLO corrections reduce these to 25% for $W^{\pm}W^{\pm}jj$ production and to 11-14% for the other processes.

From the definition of the scales, it is clear that the value for μ_{HT} is smaller than the other two choices, resulting in the largest LO results in Fig. 4.3. The scale choices μ'_{HT} and μ_{ET} have very similar shapes of the scale variation – not only at LO, but also at NLO. Furthermore, they lead to nearly identical cross section for $W^{\pm}W^{\pm}jj$ production, which is due to very similar differential distributions $\frac{d\sigma}{d\mu'_{HT}}$ and $\frac{d\sigma}{d\mu_{ET}}$ for these processes. Except for $W^{\pm}W^{\pm}jj$ production, the cross sections rapidly decrease for small values of ξ, especially

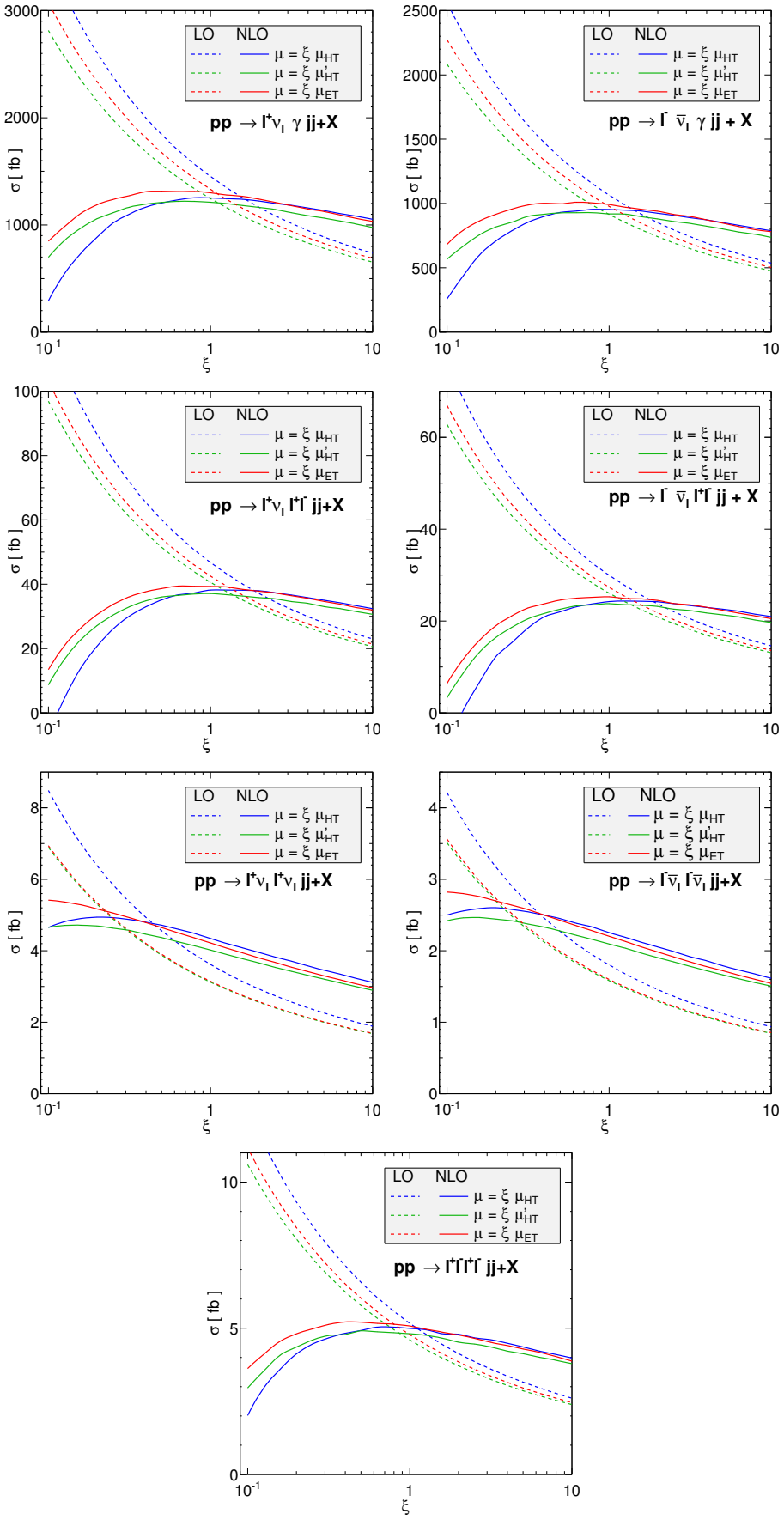

Figure 4.3.: Scale dependence of the total cross sections for $W^{\pm}\gamma jj$, $W^{\pm}Zjj$, $W^{\pm}W^{\pm}jj$ and $ZZjj$ production (from top to bottom). The renormalization and factorization scales are set to $\mu_R = \mu_F = \mu$ and varied around the various central scales defined in Eqs. (4.6), (4.8) and (4.9).

when using μ_{HT}. In this region, the scales are too small, being of the order of 10 GeV at $\xi = 0.1$, which is inappropriate for representing the kinematics of these processes. The maxima of the graphs $\sigma^{NLO}(\mu)$ are close to $\xi = 1$ and one often argues, that this region indicates a good scale, because it features the minimal dependence on scale variations. In addition, the intersections of the LO and NLO results are close to $\xi = 1$, which is a further hint towards the goodness of the scales used here.

In the following four sections, we will analyze various differential distributions of the processes W^+W^+jj, W^+Zjj, $W^+\gamma jj$ and $ZZjj$ in further detail.

4.4. $W^\pm W^\pm jj$

Compared with the other processes under consideration, the QCD-induced production of same-sign $W^\pm W^\pm jj$ is special since it does not involve gluon induced subprocesses at LO. Their absence leads to a relatively small cross section that is of similar size as for the corresponding electroweak process. For the same reason it can be expected that the interferences between the EW and QCD production modes are largest for this process. Therefore, before further discussion of the NLO correction to the QCD-induced processes, the full LO process, involving QCD as well as electroweak contributions, will be discussed.

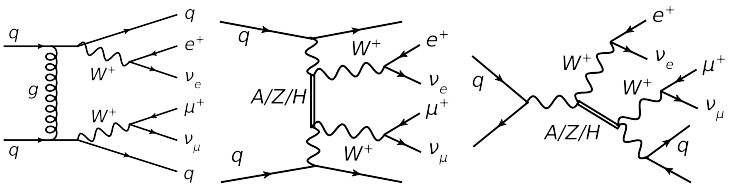

Figure 4.4.: Representative tree-level Feynman diagrams of the process $pp \to e^+\nu_e\mu^+\nu_\mu jj$. The left diagram contributes to the QCD-induced channel. The EW contributions can be split into VBF-like topologies (middle) and s-channel contributions (right). The double lines represent either a neutral EW gauge boson or the Higgs.

4.4.1. Full LO Results including QCD and EW Production Modes

As mentioned earlier, the production of $VVjj$ final states can be split into the QCD contributions of $\mathcal{O}(\alpha_s^2\alpha^2)$, EW contributions of $\mathcal{O}(\alpha^4)$ and interferences between these of order $\mathcal{O}(\alpha_s\alpha^3)$. The EW contributions can be further split into VBF-like parts that involve electroweak t- or u-channel exchanges between the two quark lines and additional s-channel contributions. Some representative diagrams are shown in Fig. 4.4.

Fig. 4.5 shows differential cross sections of the individual contributions to W^+W^+jj production. Here, the scale μ_{HT} (see Eq. (4.6)) is used as central scale in all production channels. For the VBF contributions, a common choice is the momentum transfer Q off the quark lines. However, this scale is not reasonable for the other contributions and for the sake of comparison, the same scale is used for all contributions.

In the bottom-right panel of Fig. 4.5, the distribution in the rapidity difference of the two tagging jets, defined as the two jets with the highest p_T, shows that the individual channels peak in different phase space regions. The electroweak contribution exhibits two maxima that can be assigned to the VBF and the s-channel contributions. The VBF contribution is in very good agreement with the full EW result for $\Delta y_{\text{tags}} > 3$, but fails in describing the region of low Δy_{tags}, where the contributions of the s-channel diagrams dominate. The QCD contribution peaks at low Δy_{tags}.

A similar assignment can be made for the m_{jj} distribution. The electroweak s-channel contributions peak at M_W due to the W^- splitting into a quark pair. For $m_{jj} > 150\,\text{GeV}$ the electroweak production is dominated by the VBF channels leading to a very good agreement between these two contributions. Comparing the VBF and the QCD channel, one observes large differences as well: While the QCD contribution peaks at $m_{jj} \approx 150\,\text{GeV}$, the VBF contribution is maximal for $m_{jj} \approx 500\,\text{GeV}$.

These differences can be used to enhance the EW process compared to the QCD one. Applying additional cuts of e.g.

$$m_{jj} > 200\,\text{GeV}, \quad \Delta y_{\text{tags}} > 2.5 \tag{4.10}$$

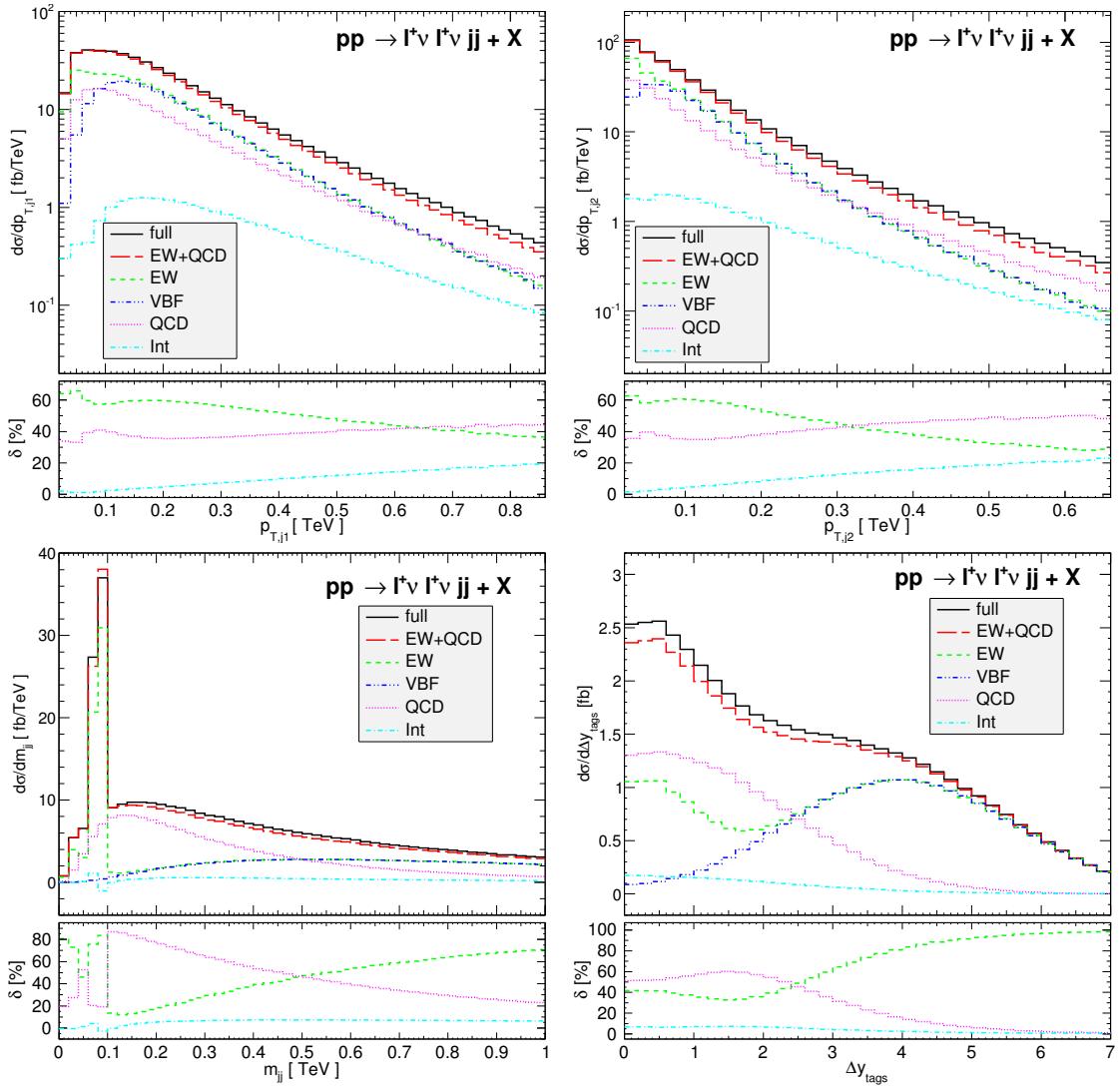

Figure 4.5.: Differential cross sections of the process W^+W^+jj for the transverse momenta of the two tagging jets as well as their invariant mass and separation. The distributions are split into various contributions and are calculated at LO using the scale μ_{HT} (see Eq. (4.6)). The small panels show the relative EW, QCD and interference contributions compared to the full LO results.

not only reduces the contribution of the QCD process from 37% to 16%, but also legitimates the use of the VBF approximation for the EW process.

The interferences between the QCD and EW channels only contribute with about 5% to the total cross section. However, as it can be seen in Fig. 4.5, they can get large in phase space regions that only give a small contribution to the total cross section. Their contribution increases for high p_T of the jets up to about 20% for $p_{T,j1} \approx 900\,\text{GeV}$ or $p_{T,j2} \approx 600\,\text{GeV}$. In the Δy_{tags} distribution, the contribution of the interferences decreases from 9% to less than 1% in regions of large Δy_{tags}. This effect can be explained by the color structure of the amplitudes (see Section 3.1). For large jet separations Δy_{tags}, the effects of s-channel diagrams are largely suppressed and only interferences of the EW t-channel diagrams with the u-channel diagrams of the QCD process (or vice versa) contribute. Since only one of these channels can get large, this leads to a large suppression of the interference effects. In the m_{jj} distribution, the interference effects only show a small dependence for $m_{jj} > 200\,\text{GeV}$. However, in the low mass region there are some sign changes that relate

to the propagators of the electroweak s-channel contributions as depicted in Fig. 4.5. The most striking one takes place at $m_{jj} = M_W$, where the propagator of the W^- boson, which splits into a quark-antiquark pair, changes its sign. Further sign changes close to this region occur, when the invariant mass of the two jets and one of the vector bosons, m_{jjV}, passes M_Z or M_H.

Since the interference effects are small, one can study the QCD and EW processes separately. Therefore, in the following only the QCD-induced contributions are considered at next-to-leading order. When combining these results with the corresponding EW ones, it is possible to add the interference contributions at LO. Once more, it should be mentioned that the interference effects are expected to be largest for $W^\pm W^\pm jj$ production due to the absence of gluon induced subprocesses and because both QCD and EW amplitudes involve only left-chiral quarks and leptons. For the other processes, one can expect to obtain interference effects smaller than 5% of the total cross section.

4.4.2. NLO QCD Corrections to QCD-induced W^+W^+jj Production

The effects of the QCD corrections on the total cross section have already been shown in Section 4.3. The K-factor, defined as the ratio of the NLO to the LO result, is 1.20 when using μ_{HT} as factorization and renormalization scales. However, this factor cannot reflect the dependence of the QCD corrections on kinematical quantities and a discussion based on differential cross sections is mandatory. Fig. 4.6 shows important distributions at LO and NLO as well as the corresponding differential K-factors.

In the p_T distributions of the jets in Fig. 4.6, the NLO corrections show, except for the low p_T region, only a modest phase space dependence: The differential K-factors are monotonically falling, leading to slightly softer jets at NLO. This might be due to the three jet events, which account for about 65% of the NLO cross section, where the third jet carries away momentum from the tagging jets. While for $p_{T,j1} < 100\,\text{GeV}$ the K-factor increases up to 1.5, beyond this low p_T region the K-factor slightly decreases from 1.2 to 1.1; in the $p_{T,j2}$ distributions the K-factor drops from 1.25 in the low p_T region to 1.05 at $p_{T,j2} = 700\,\text{GeV}$.

The NLO corrections to the invariant mass and rapidity separation of the two tagging jets exhibit a more striking dependence, with corrections of about a factor of two appearing in both distributions. The K-factor is close to two in the low m_{jj} region and rapidly drops for $m_{jj} < 200\,\text{GeV}$. After that, it slowly decreases further, being less than one for $m_{jj} > 1\,\text{TeV}$. The differential K-factor to the rapidity separation of the tagging jets constantly decreases from 1.4 at $\Delta y_{\text{tags}} = 0$, reaching 0.6 at $\Delta y_{\text{tags}} = 6$. Understanding these large corrections is important, because one typically demands large separations of the tagging jets when studying vector boson scattering. It turns out that these large corrections are mostly caused by the use of the scale μ_{HT}, which is not appropriate in this phase space region: The invariant mass m_{ij} of two massless particles i and j can be expressed as

$$m_{ij}^2 = 2p_{T,i}p_{T,j}\left(\cosh\Delta y_{ij} - \cos\Delta\phi_{ij}\right), \tag{4.11}$$

where Δy_{ij} and $\Delta\phi_{ij}$ are their rapidity and azimuthal angle separations, respectively. Hence, the invariant mass m_{ij}, which certainly is a relevant scale of the process, largely increases with the rapidity separation Δy_{ij}, while the transverse momenta can be small. Since the scale μ_{HT} only includes the transverse momenta of the jets, it is too small in the high Δy_{tags} region. Therefore, one uses a too large value of α_s which is compensated by large negative NLO corrections. A more suitable scale should therefore include the invariant mass as well as the p_T of the jets. This justifies the use of the scales μ'_{HT} and μ_{ET} defined in Eqs. (4.8) and (4.9). Due to the additional exponential in μ'_{HT}, this scale

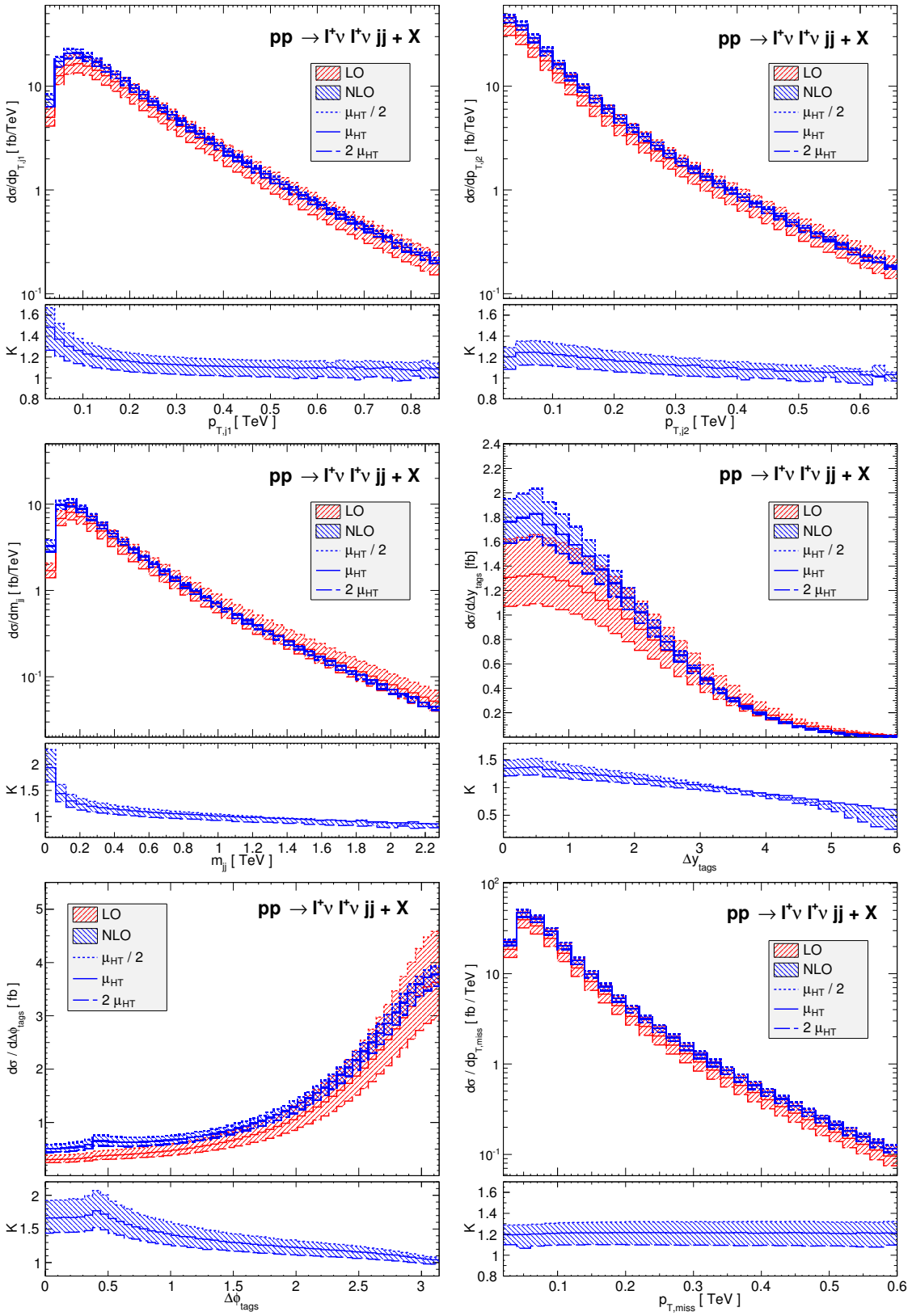

Figure 4.6.: Differential cross sections at LO and NLO as well as the corresponding differential K-factors for QCD-induced W^+W^+jj production. The upper row shows the transverse momentum of the two hardest jets, ordered in p_T. In the middle, the distributions of their invariant mass and rapidity separation are shown. In the lower row the azimuthal angle difference of the hardest jets as well as the missing transverse momentum are shown. The bands describe scale variations by a factor of two around the central scale μ_{HT}. The K-factor bands are due to the scale variation of the NLO results, with respect to $\sigma_{LO}(\mu_{HT})$.

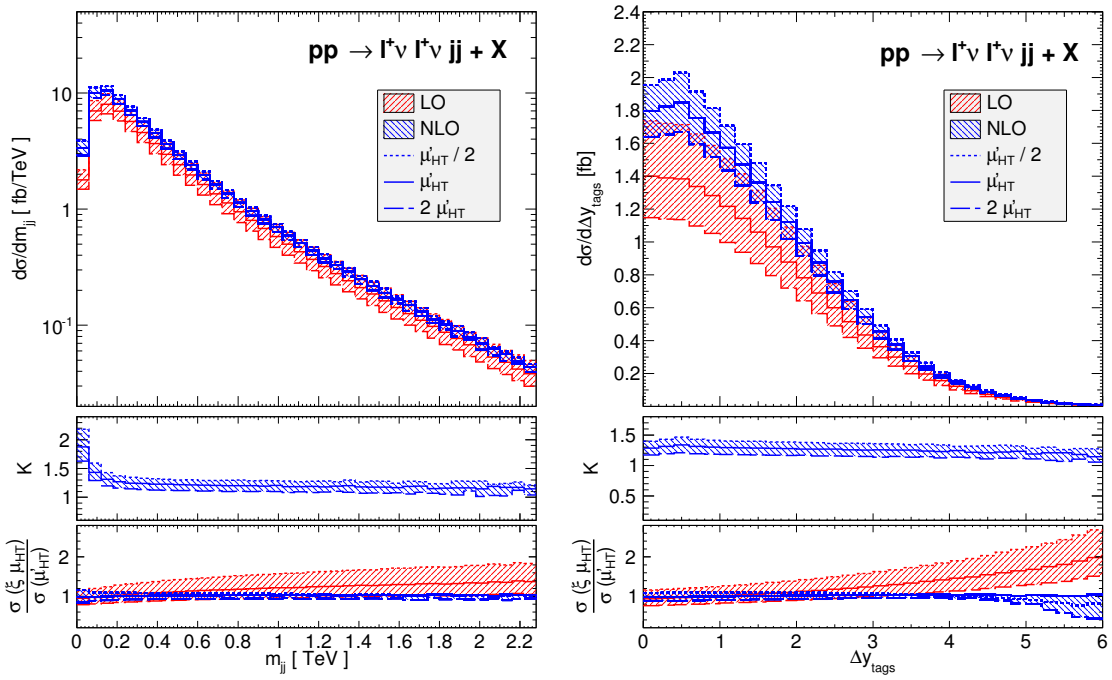

Figure 4.7.: Differential cross sections for $W^{\pm}W^{\pm}jj$ production showing the distribution of the invariant mass and rapidity separation of the tagging jets. The top and middle panels are as in Fig. 4.6, but using the modified scale μ'_{HT}. The lower panel shows the ratio of the differential cross sections using the scale $\xi\ \mu_{HT}$ over the modified scale μ'_{HT} at LO and NLO with $\xi \in [1/2, 2]$.

is equal to μ_{HT} for $\Delta y_{\text{tags}} = 0$, but resembles the invariant mass for large separations. A similar scale choice has been used in Ref. [125] for dijet production at NLO QCD. The scale μ_{ET} features a similar behavior. If the jets are close to each other, they typically have a low invariant mass and for the (vectorial) sum of the transverse momenta holds $p_{T,jj} \approx p_{T,j1} + p_{T,j2} \approx E_T(jj)$. However, for large separations, $p_T(jj)$ typically gets small and one obtains $E_T(jj) \approx m_{jj}$.

Figs. 4.7 and 4.8 show the distributions of the invariant mass and rapidity separation of the tagging jets using the modified scales μ'_{HT} and μ_{ET}. Except for the region $m_{jj} < 200\,\text{GeV}$, the phase space dependence of the K-factors is largely reduced, being nearly flat for μ'_{HT}. In addition, the plots show the ratio of the cross sections evaluated with μ_{HT} and μ_{ET} compared to $\sigma(\mu'_{HT})$. There, one observes that the three scale choices lead to a very good agreement of the shapes at NLO and the differences basically reduce to the overall scale uncertainty of about 15%. While the LO results using μ'_{HT} and μ_{ET} are in good agreement within the scale uncertainty, $\sigma(\mu_{HT})$ differs from the other results by a factor of two in the high Δy_{tags} region. Hence, the K-factor of 0.6 observed in the high region of the Δy_{tags} distributions shown in Fig. 4.6 is due to the too large LO result caused by the use of the improper scale μ_{HT}. A further indication of the failing of this scale in this region is the increasing width of the scale uncertainty band at NLO. This is primarily due to the result of $\sigma_{NLO}(\mu_{HT}/2)$ which shows that this scale is too small here.

As it can be seen in Fig. 4.6, the azimuthal angle difference of the tagging jets peaks at $\Delta\phi_{\text{tags}} = \pi$. This reflects a different behavior compared to the processes that will be discussed in the following sections and can be explained by the special structure of this process: It does not involve external gluons at LO, whereas for the other processes the LO subprocesses with external gluons constitute $\sim 85\%$ of the cross section. The quark-gluon and gluon-gluon splittings appearing in the other processes lead to more events

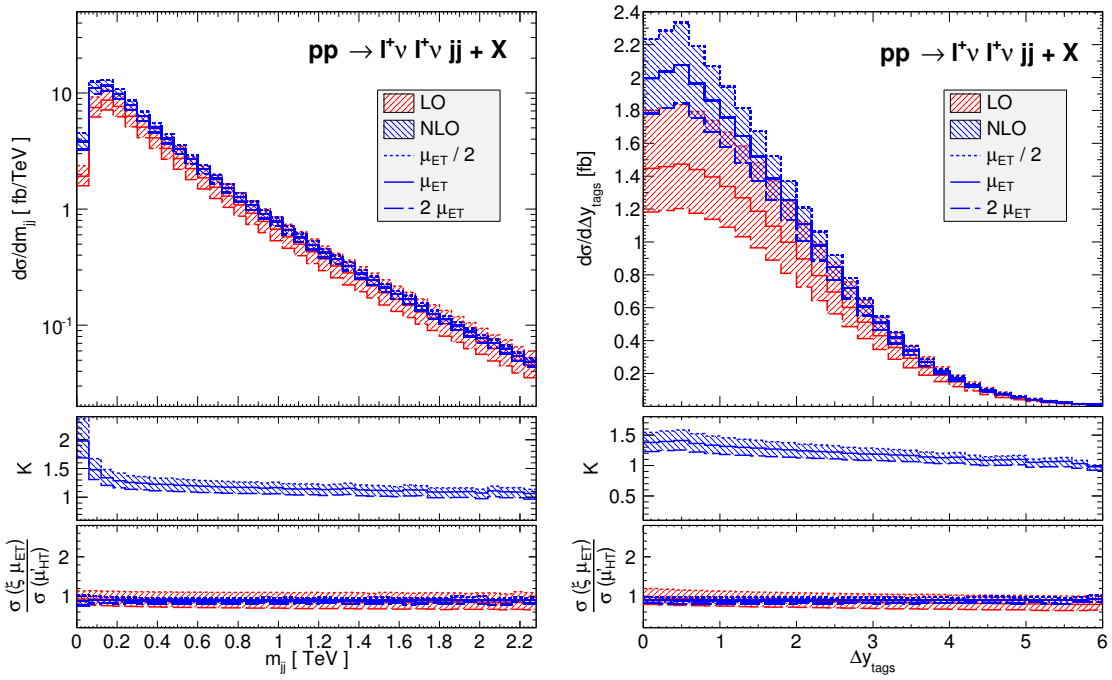

Figure 4.8.: Differential cross sections for $W^{\pm}W^{\pm}jj$ production showing the distribution of the invariant mass and rapidity separation of the tagging jets. The top and middle panels are as in Fig. 4.6, but using the modified scale μ_{ET}. The lower panel shows the ratio of the differential cross sections using the scale $\xi\ \mu_{ET}$ over the scale μ'_{HT} at LO and NLO with $\xi \in [1/2, 2]$.

with smaller separations of the jets. Another feature of this process is its symmetry: The dominant subprocesses are of the type

$$qq \to W^+W^+qq \to l^+\nu\, l^+\nu\, qq, \tag{4.12}$$

where each initial and final state particle appears in pairs. This leads to more symmetric final states with identical particles preferential recoiling against each other. The same argument holds for the subprocesses with $\bar{q}\bar{q}$ in the initial state and for the $q\bar{q}$ initiated subprocesses only the appearance of suppressed s-channel contributions might lead to a different behavior.

The distribution of missing transverse momentum, shown in the bottom right of Fig. 4.6, obeys a nearly flat K-factor. In general, the distributions of W decay products, which are not shown here, have only a small phase space dependence. In the p_T distributions of the leptons and the distribution of their invariant mass, the K-factor decreases from 1.2 to 1.0 in the tails of the distributions, similar to the $p_{T,j2}$ distribution. The rapidity distributions of the leptons have a nearly constant K-factor with a slightly increasing scale uncertainty for large $|y_l|$.

It remains to discuss the large K-factor for $m_{jj} < 200\,\text{GeV}$, which is common for all three scale choices. Although the identical behavior of the scales can be expected here, since they agree in the low m_{jj} limit as discussed, it turns out that this increase is due to a new configuration opening up at NLO. The gluon appearing in the real emission can become a jet on its own, while the quarks only lead to one further jet. This contribution peaks at low invariant masses of the jets due to the quark-gluon splitting depicted in Fig. 4.9. We have confirmed that this effect indeed causes the observed increase of the K-factor by separately calculating the real emission contributions with one gluon jet and only one further jet.

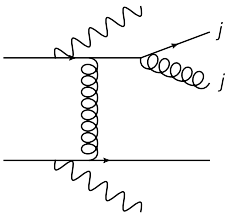

Figure 4.9.: Feynman diagram representing the new contributions appearing at NLO, which causes the large K-factor in the region $m_{jj} < 200\,\text{GeV}$ in Figs. 4.6 through 4.8.

Knowing that the scale μ_{HT} is too small for large separations or invariant masses of the jets, we will not use it further in the following discussions of the other processes. Since the scales μ'_{HT} and μ_{ET} are in good agreement, both at LO and NLO, only one of those will be used respectively in the following sections.

4.5. $W^{\pm}Zjj$: QCD-induced Production

For the production of $W^{\pm}Zjj$, no new channels open up at NLO and therefore one does not expect phase space regions with large K-factors as it is the case in W^+W^+jj production. Fig. 4.10 shows kinematical distributions of the tagging jets for W^+Zjj production using the scale μ'_{HT} (see Eq. (4.8)).

Comparing the $p_{T,j}$ distributions of Fig. 4.6 and Fig. 4.10, one notes that in W^+Zjj more soft events are produced than in W^+W^+jj production: While in the former process the transverse momentum distribution of the second jet drops by four orders of magnitude in the range $p_{T,j2} < 700\,\text{GeV}$, it only reduces by 2-3 orders in the latter process. A similar effect, but not as pronounced, can also be seen in the $p_{T,j1}$ distribution. This is due to the appearance of subprocesses with external gluons, which contribute about 85% of the cross section. The initial state gluons carry not only typically smaller momentum fractions of the initial state protons, but also gluon radiation peaks at low gluon momenta and low parton separations[‡]. The absence of gluonic subprocesses in W^+W^+jj production also leads to a largely reduced cross section in the first bin of the $p_{T,j1}$ distribution.

The K-factor of the m_{jj} distribution increases from 0.8 to 1.1 in the range $0 < m_{jj} < 600\,\text{GeV}$. Beyond this region, it stays nearly constant. For the Δy_{tags} distribution, the K-factor increases from 0.8 to 1.2 in the range $0 < \Delta y_{\text{tags}} < 6$. The NLO corrections of $\lesssim 20\%$ and a nearly flat K-factor in the m_{jj} distribution show that μ'_{HT} is a good scale choice for this process, even though it does not produce as flat K-factors as in W^+W^+jj production (Fig. 4.7).

Compared to W^+W^+jj production, the gluonic subprocesses lead to a significant difference in the distribution of the azimuthal angle difference of the tagging jets, with only a small dependence on $\Delta\phi_{\text{tags}}$. However, the cross section would diverge in the low $\Delta\phi_{\text{tags}}$ region, if no separation cut on the jets would be applied. The effects of this cut are clearly visible at $\Delta\phi_{\text{tags}} = 0.4$ and $\Delta y_{\text{tags}} = 0.4$, and the effects are much stronger than in W^+W^+jj production.

It is important to study the kinematical distributions of the electroweak decay products, since also effects of new physics beyond the SM are expected to have an influence here. Typical BSM signals are e.g. new resonances in the invariant mass distribution of the EW vector bosons, enhanced contributions in the tails of the total transverse energy,

$$H_T = \sum_{i\,\in\,\text{jets}} p_{T,i} + \sum_{i\,\in\,\text{leptons}} p_{T,i} + \not{p}_T, \tag{4.13}$$

or transverse momentum distributions [112, 113, 126, 127]. Therefore, knowing the next-to-leading order corrections in the SM is very important, since an enhancement due to these could be misinterpreted as an indication for BSM physics. Higher order terms can lead to large corrections in the tails of distributions, if new channels open up in the real emission contributions. This has been shown in Refs. [128–131], where NLO results for vector boson (pair) production with different jet multiplicities have been merged to obtain approximate NNLO results using the LoopSim method [128].

Important distributions of the EW system are shown in Fig. 4.11. The upper left distribution shows the invariant mass of the WZ system, which cannot be fully reconstructed experimentally due to the unknown longitudinal momentum of the neutrino. However, the invariant mass can be estimated by either assuming the W boson to be on-shell and

[‡]Here, we are interested in the non-singular region, where the radiated gluon and the emitter produce two separate jets.

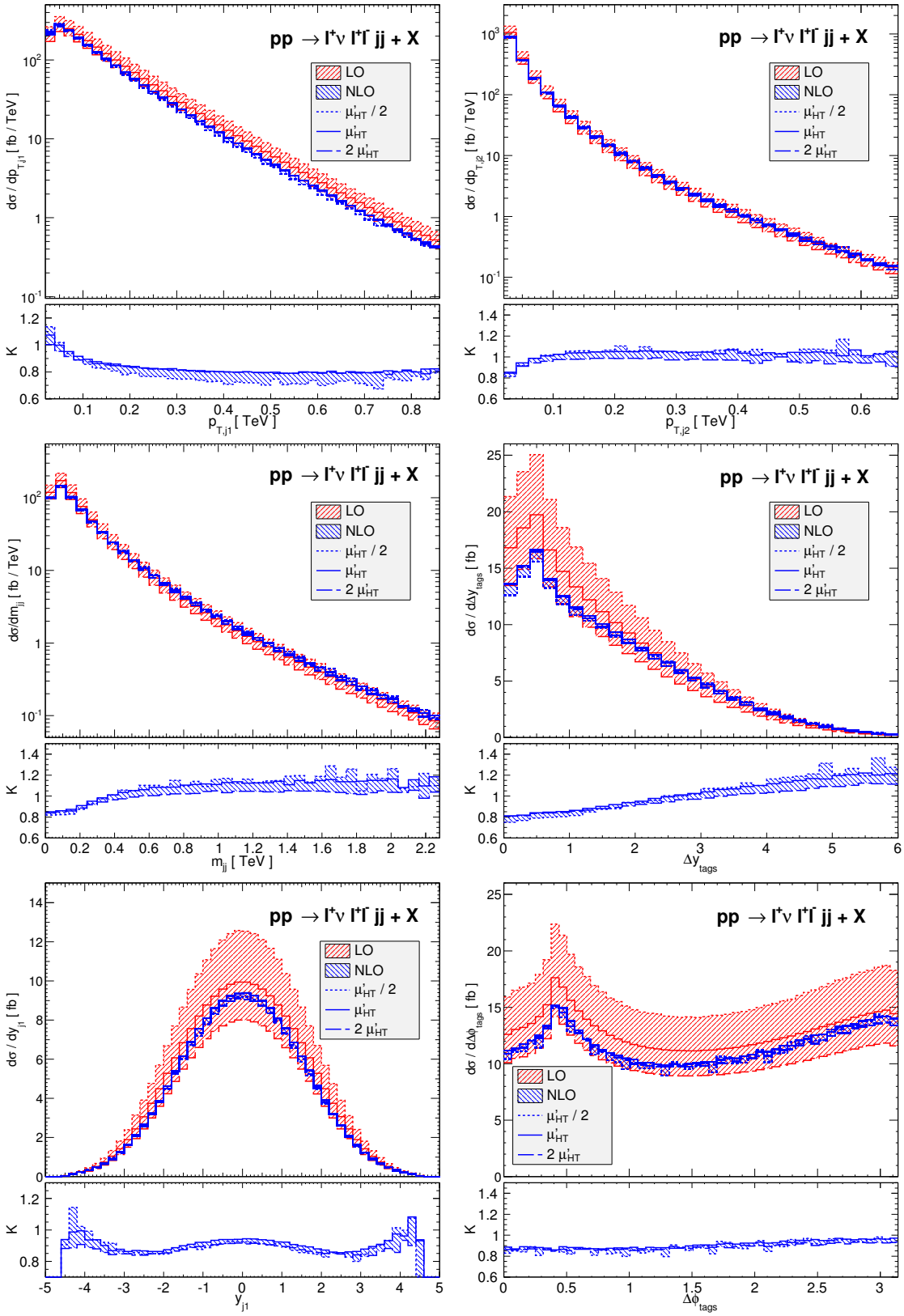

Figure 4.10.: Differential cross sections at LO and NLO as well as the corresponding differential K-factors for W^+Zjj production, similar to Fig. 4.6, but using the central scale μ'_{HT}. In addition to the transverse momentum, invariant mass and rapidity separation of the tagging jets, the rapidity distribution of the hardest jet as well as the azimuthal angle difference of the tagging jets are shown.

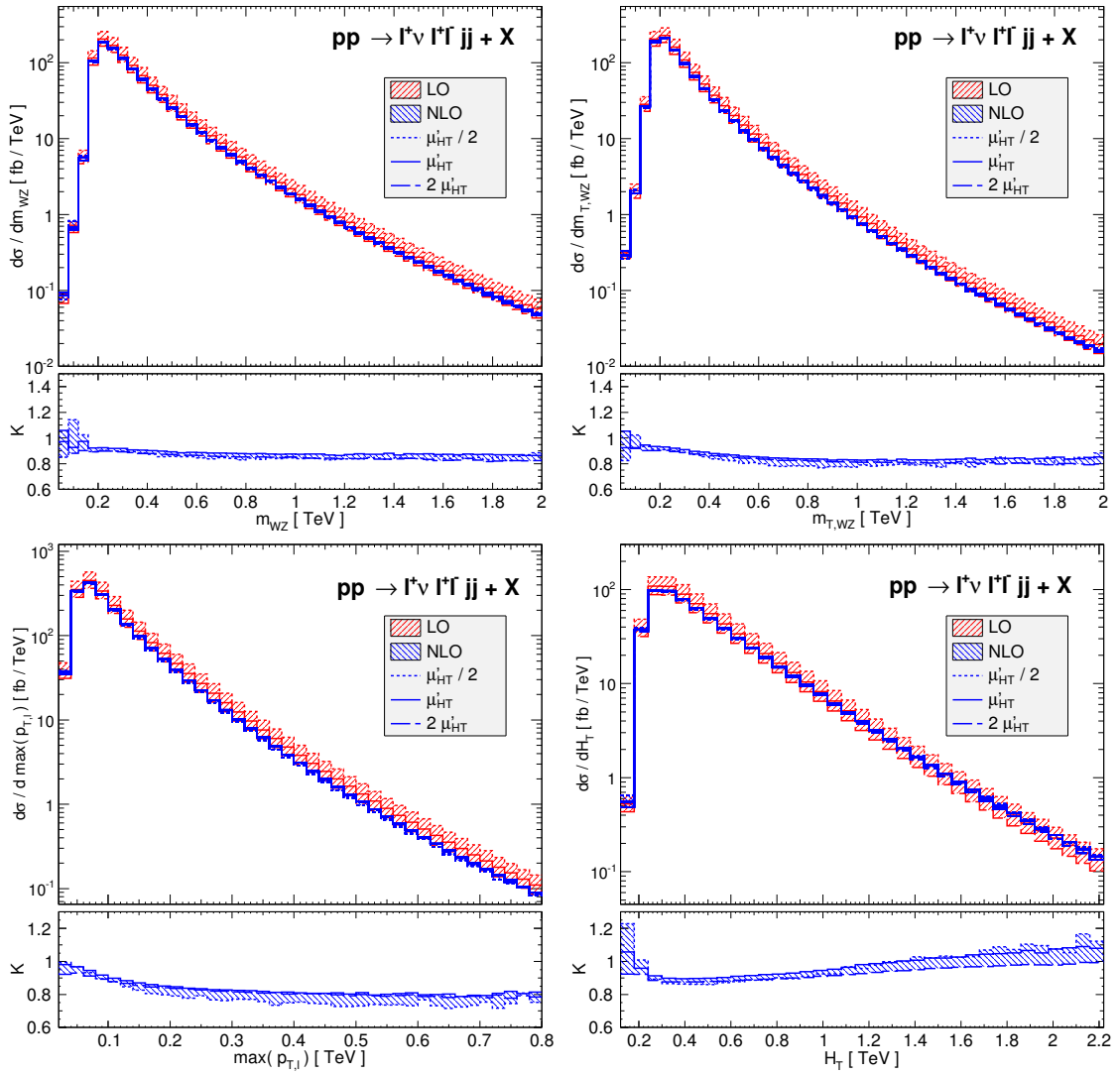

Figure 4.11.: Differential cross sections at LO and NLO as well as the corresponding differential K-factors for W^+Zjj production, similar to Fig. 4.6, but using the central scale μ'_{HT}. The upper row shows the invariant mass of the WZ system and its cluster transverse mass as defined in Eq. (4.14). In the lower row, the transverse momentum distribution of the hardest lepton as well as the distribution of the total transverse energy H_T, defined in Eq. (4.13), are shown.

reconstructing the longitudinal neutrino momentum from this assumption, or using the cluster transverse mass [112, 132]

$$m^2_{T,WZ} = \left(\sqrt{m^2(\ell\ell\ell) + p^2_T(\ell\ell\ell)} + |p_{T,\text{miss}}| \right)^2 - \left(\vec{p}_T(\ell\ell\ell) + \vec{p}_{T,\text{miss}}\right)^2 , \tag{4.14}$$

which is shown in the upper right. Compared to the true value of m_{WZ}, the missing information of the longitudinal momentum leads to a small shift towards lower values of $m_{T,WZ}$. The NLO corrections show only a minor dependence on the electroweak system, with a slightly increasing K-factor in the low p_T and low mass regions. Only the H_T distribution, which includes the transverse momenta of the jets as well, has an increasing K-factor in the tail of the distribution, indicating that the scale is chosen slightly too high in this region.

4.6. $W^{\pm}\gamma jj$: QCD-induced Production

Compared to the other processes under consideration, there is only one vector boson decaying into leptons in $W^{\pm}\gamma jj$ production. The missing branching ratio of the second boson leads to a significantly larger cross section in $W^{\pm}\gamma jj$ production, allowing for measurements with much higher event rates. Since the structure of this process is very similar to $W^{\pm}Zjj$ production, one can expect to obtain similar results for the shapes of the distributions. This can be seen by comparing the jet distributions of these processes, which are shown in Figs. 4.10 and 4.12. Not only the shapes of the distributions are similar, but also the differential K-factors show the same behavior.

Since the distributions of the jets closely follow the results of Section 4.5, the focus of this section will be on the kinematical distributions of the $W\gamma$ system, which are presented in Figs. 4.13 and 4.14. The distribution of the invariant mass $m_{W\gamma}$ exhibits two maxima, with a sharp peak at $m_{W\gamma} = M_W$ being due to the three body decay of $W \to \ell\nu\gamma$. The corresponding contribution in $W^{\pm}Zjj$ production is largely suppressed, since one of the vector boson propagators would have to be far off-shell. Beyond this first sharp peak, the distribution is similar to the one in $W^{\pm}Zjj$ production, but due to the production of only one massive vector boson, it is shifted towards lower values of the invariant mass. As in $W^{\pm}Zjj$ production, the invariant mass cannot be reconstructed experimentally and one has to use the cluster transverse mass [132, 133]

$$m_{T,W\gamma}^2 = \left(\sqrt{m^2(\ell\gamma) + p_T^2(\ell\gamma)} + |p_{T,\text{miss}}|\right)^2 - \left(\vec{p}_T(\ell\gamma) + \vec{p}_{T,\text{miss}}\right)^2, \tag{4.15}$$

similar to Eq. (4.14). Comparing the distributions of $m_{T,W\gamma}$ and $m_{W\gamma}$, one observes poor agreement in the low mass region, with more low mass events in the distribution of $m_{T,W\gamma}$.

When studying the gauge interactions of the EW bosons, one is not interested in the final state radiation with the photon being emitted from the lepton. This contributions can be reduced by applying a cut on the cluster transverse mass of $m_{T,W\gamma} > 90\,\text{GeV}$. The results obtained with this additional cut are shown in Figs. 4.13 and 4.14 as well. Comparing the $m_{W\gamma}$ and $m_{T,W\gamma}$ distributions shows, that the three body decay of the W boson can be reduced with this cut, even though the cluster transverse mass yields only a poor approximation of the true invariant mass in this region. The reduction of events due to radiative W decays, by applying the additional cut, is also apparent in the distributions showing the separation of the lepton and photon in Fig. 4.13. Especially in the $R_{\ell\gamma}$ and $\Delta\phi_{\ell\gamma}$ distributions, the peak at low separations is completely removed.

The K-factors in the $m_{W\gamma}$, $m_{T,W\gamma}$ and $\Delta\phi_{\ell\gamma}$ distributions show only minor dependences. Larger phase space dependences can be observed in the distributions of R separation and rapidity difference. While the K-factor steadily increases in the $\Delta y_{\ell\gamma}$ distribution, it shows a more complicated structure in the R separation distributions. There, it is nearly constant for $R < \pi$, because the separation can be increased by changing the azimuthal angle difference, which only has a small effect on the NLO corrections. Beyond this region, a further increase of the R separation is only possible by increasing the rapidity separation leading to an increase of the K-factor. In this region, one can also observe an increase of the scale uncertainty.

Fig. 4.14 shows the transverse momenta distributions of the photon, the lepton and the neutrino as well as the distribution of the invariant mass $m_{\ell\gamma}$. The K-factor has a similar behavior for all these distributions: It drops from 1 at low values to about 0.8 at 500 GeV. Therefore, the dependence of the K-factor on these variables is of similar size as on the jet distributions in Fig. 4.12.

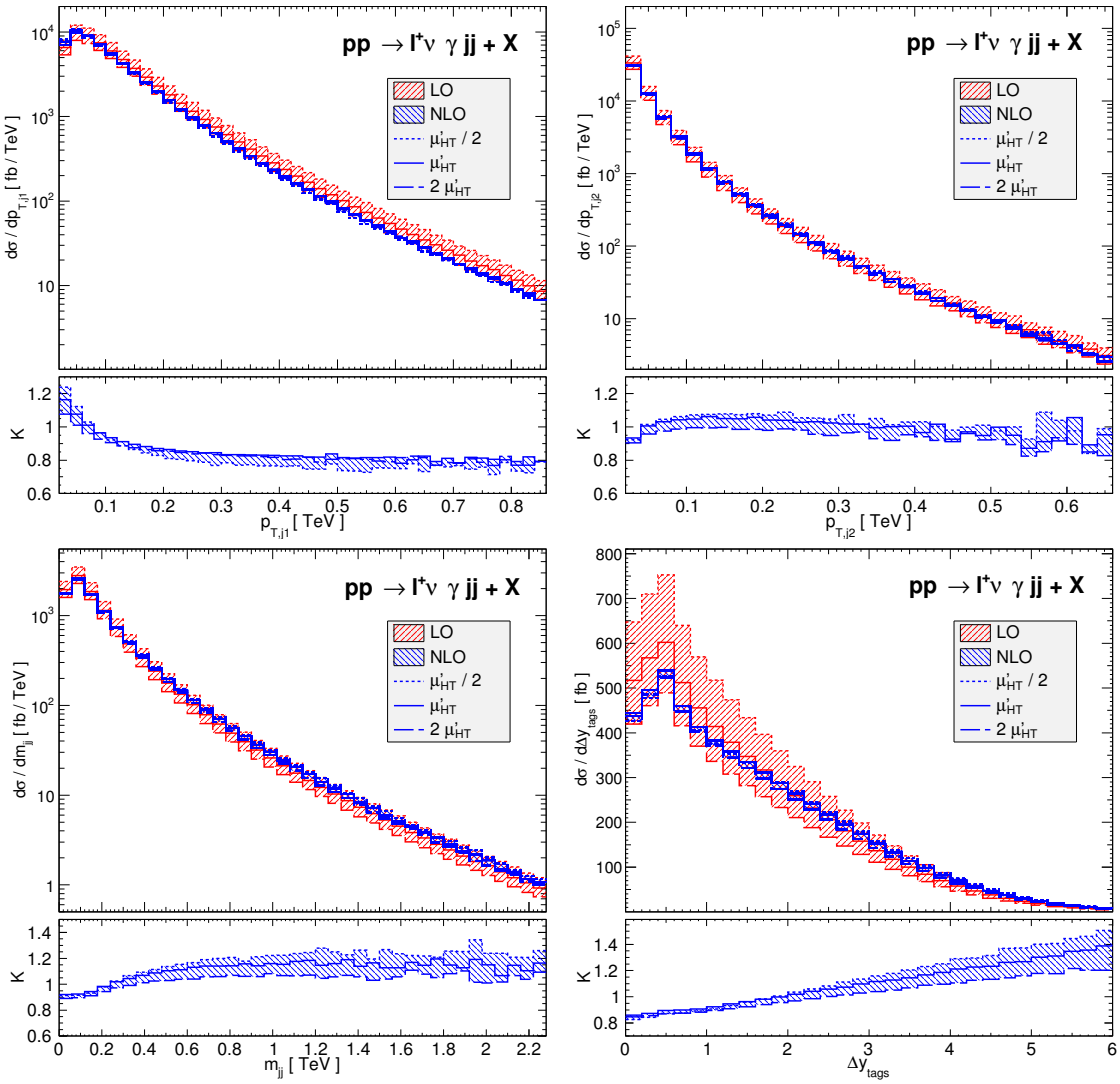

Figure 4.12.: Differential cross sections at LO and NLO as well as the corresponding differential K-factors for $W^+\gamma jj$ production, similar to Fig. 4.6, but using the central scale μ'_{HT}. The transverse momentum distribution of the tagging jets as well as their invariant mass and rapidity separation are shown.

It is worth noting that the K-factors of the results obtained with the additional $m_{T,W\gamma}$ cut closely follow the corresponding K-factor without this cut for all the distributions discussed here.

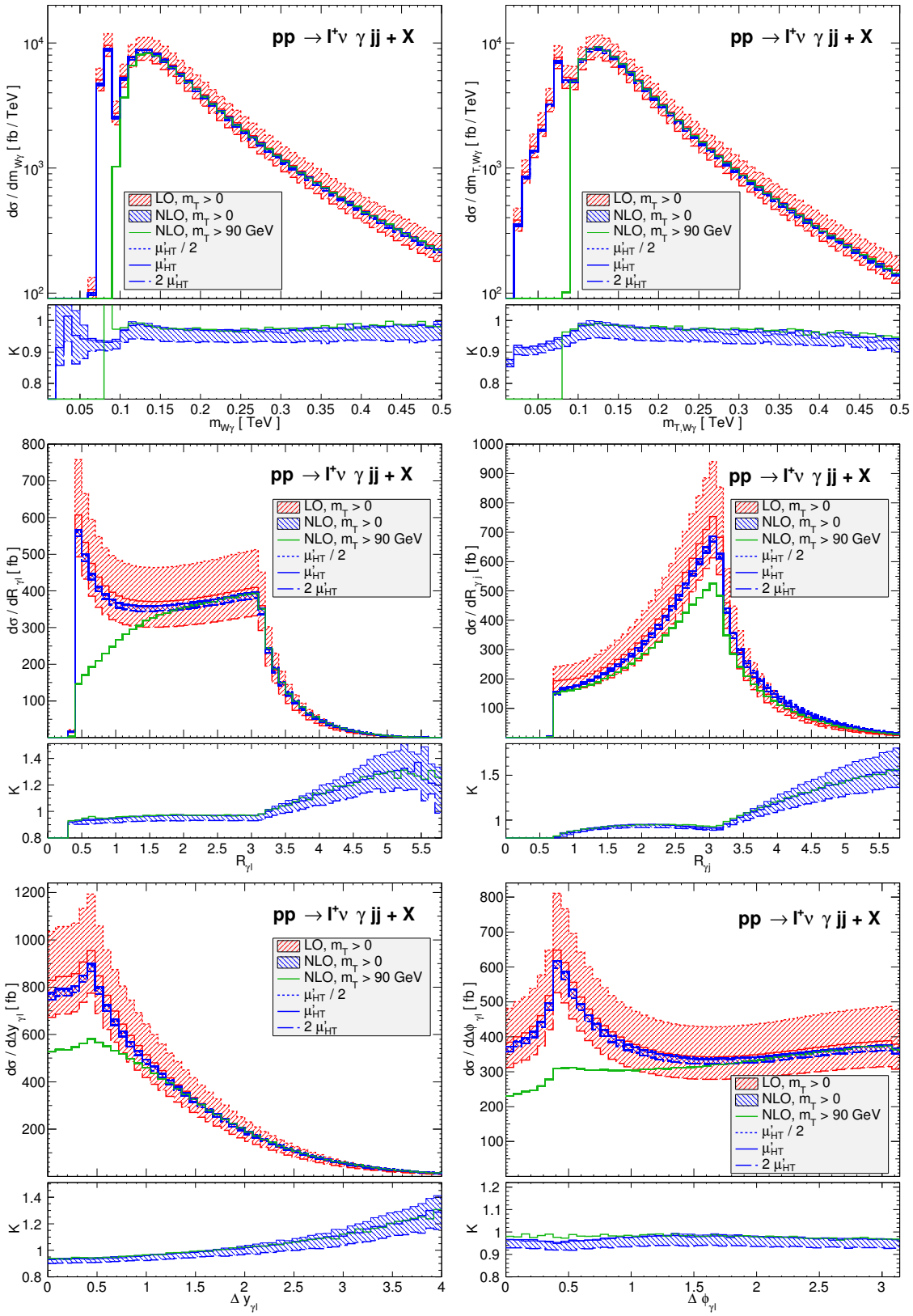

Figure 4.13.: Differential cross sections at LO and NLO as well as the corresponding differential K-factors for $W^+\gamma jj$ production, similar to Fig. 4.6, but using the central scale μ'_{HT}. In addition to the results which are obtained using the cuts as defined in Section 4.2, also the results for $\sigma^{NLO}(\mu'_{HT})$ with an additional cut of $m_{T,W\gamma} > 90\,\text{GeV}$ are shown. The distributions of the invariant mass as well as the cluster transverse mass of the $W\gamma$ system are shown in the top row. The middle row shows the distribution of the R separation of the photon to the lepton and jets. The rapidity and azimuthal angle separation of the photon and lepton are shown in the lower row.

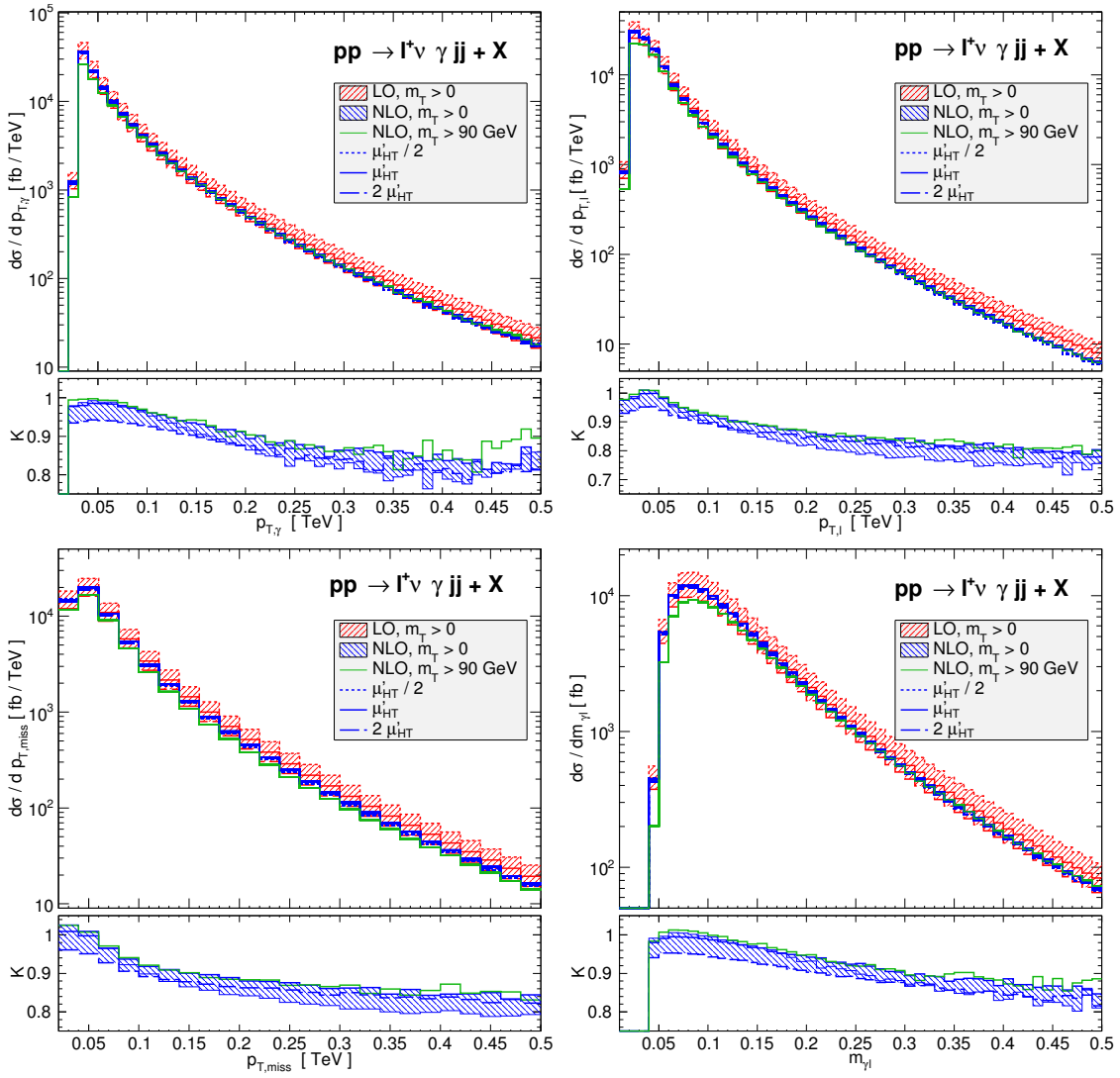

Figure 4.14.: Differential cross sections at LO and NLO as well as the corresponding differential K-factors for $W^+\gamma jj$ production, similar to Fig. 4.6, but using the central scale μ'_{HT}. In addition to the results which are obtained using the cuts as defined in Section 4.2, also the results for $\sigma^{NLO}(\mu'_{HT})$ with an additional cut of $m_{T,W\gamma} > 90\,\text{GeV}$ are shown. The distributions show the transverse momentum of the photon, the lepton and the neutrino ($p_{T,\text{miss}}$) as well as of the lepton-photon invariant mass.

4.7. $ZZjj$: QCD-induced Production

In contrast to the other processes discussed in this thesis, $ZZjj$ production has an experimentally fully reconstructible leptonic final state. It is of high importance, since the corresponding EW contribution includes Higgs production via vector boson fusion, with decay of the Higgs boson to four charged leptons. This experimentally clear final state allows for precise measurements of the Higgs mass and coupling to the Z bosons.

In the following, the QCD process is calculated using μ_{ET} as the central value for the factorization and renormalization scales. It has been checked that the results using μ'_{HT} as the central scale are very close to the ones presented here, as it has also been shown in Section 4.4 in W^+W^+jj production. The distributions related to the two hardest jets are shown in Fig. 4.15. The shape and the corresponding K-factors are very similar to the ones obtains in $W^\pm Zjj$ and $W^\pm\gamma jj$ production. Only the rapidity separation distribution of the tagging jets shows a larger difference, with the K-factor significantly increasing with the jet separation. This difference does not occur due to the different choice of the scales, but is likely a process specific effect.

The invariant mass distribution of the four lepton system is shown in the top left of Fig. 4.16. Below the large continuum contribution in the phase space region of $m_{ZZ} \gtrsim 2M_Z$, where on-shell production of both Z bosons is possible, there is an additional peak at $m_{ZZ} = M_Z$ due to the four lepton decay of a Z boson. At NLO a contribution with a s-channel Higgs boson exchange appears in the virtual amplitude, which for $m_{ZZ} \approx M_H$ behaves as

$$\mathcal{M}^V(m_{ZZ}^2) \sim \frac{1}{m_{ZZ}^2 - M_H^2 + \mathrm{i}M_H\Gamma_H}. \tag{4.16}$$

Because the virtual amplitude is interfered with the Born amplitude, which does not involve the Higgs propagator, one does not obtain a Breit-Wigner distribution in this region, but the structure of a single pole. Therefore, in the vicinity of $m_{ZZ} = M_H$ the contributions below and above this threshold nearly cancel. The contribution due to the Higgs boson therefore peaks in the continuum region at about $m_{ZZ} = 200\,\mathrm{GeV}$ and contributes with about 0.3% to the cross section. The corresponding contribution is shown separately in the top left plot of Fig. 4.16.

For a full description of $ZZjj$ production, not only the corresponding EW processes, but also the Hjj production via gluon fusion, with the Higgs boson decaying into four leptons, should be added to the results shown here. The gluon fusion contribution can be added without double counting the Higgs contributions: The diagrams in the virtual amplitude involving the Higgs boson are only interfered with the continuum of $ZZjj$ production, whereas the corresponding squared matrix elements appear in the gluon fusion process.

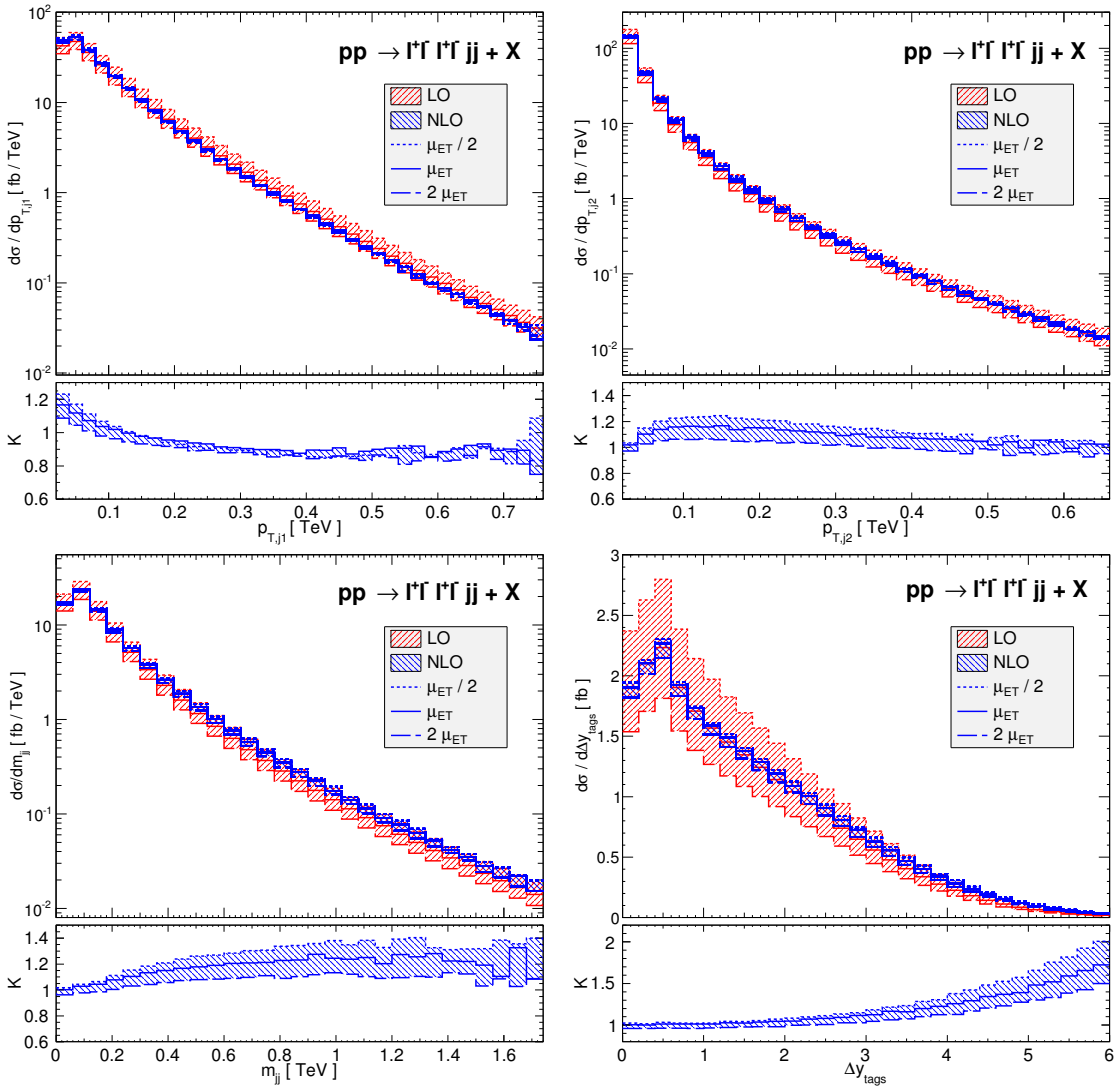

Figure 4.15.: Differential cross sections at LO and NLO as well as the corresponding differential K-factors for $ZZjj$ production, similar to Fig. 4.6, but using the central scale μ_{ET}. The transverse momentum of the tagging jets as well as their invariant mass and rapidity separation are shown.

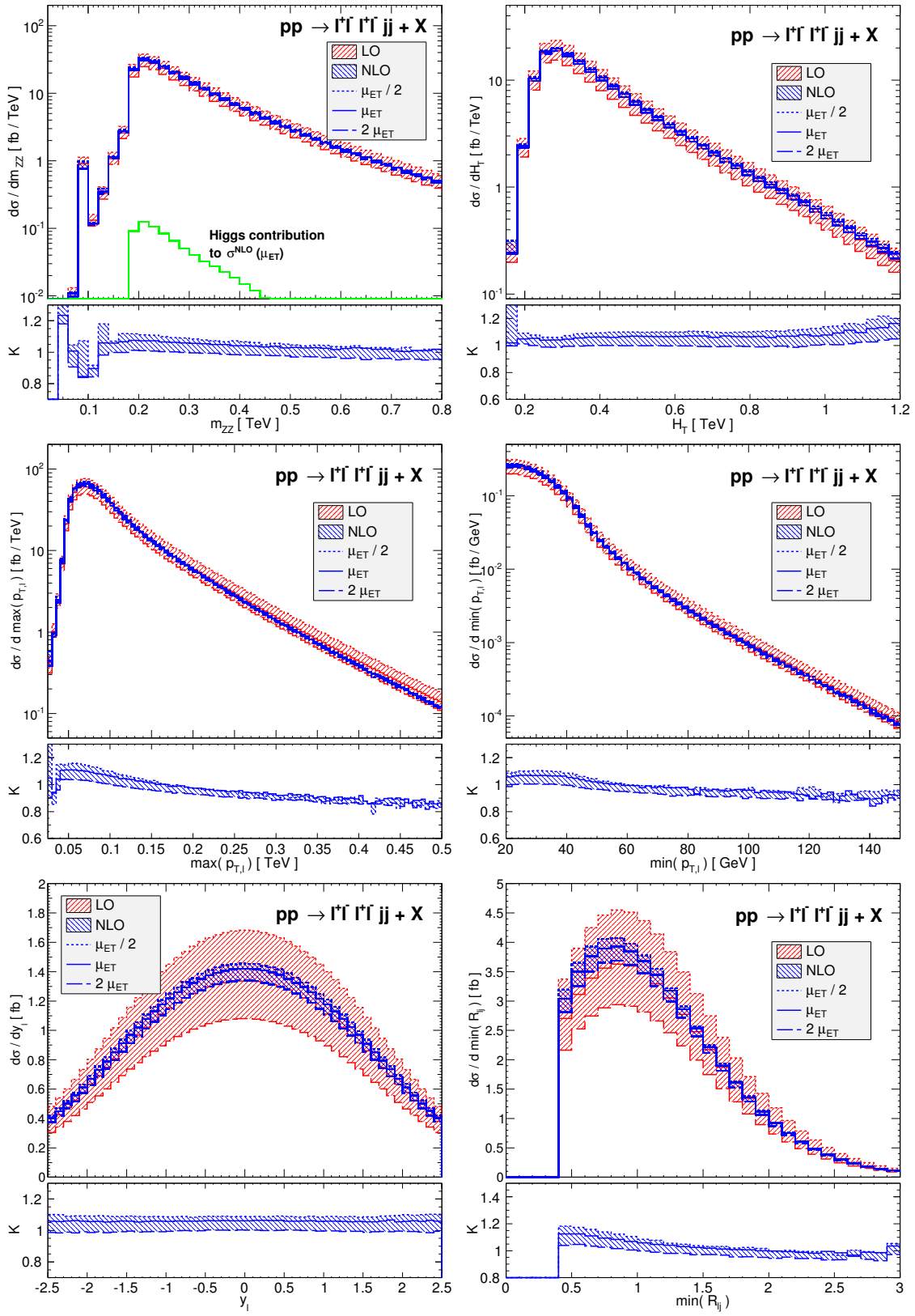

Figure 4.16.: Differential cross sections at LO and NLO as well as the corresponding differential K-factors for $ZZjj$ production, similar to Fig. 4.6, but using the central scale μ_{ET}. The invariant mass distribution of the four leptons is shown in the upper left panel, where the contribution of the Higgs boson to $\sigma^{NLO}(\mu_{ET})$ is shown separately. In the top right panel, the distribution of the total transverse momentum H_T defined in Eq. (4.13) is shown. In the middle row, the distributions of the maximum and minimum lepton transverse momenta are shown. The lower row shows the rapidity distribution of the leptons as well as the minimum of the lepton-jet R separation.

CHAPTER 5

Summary and Outlook

In this thesis, the QCD-induced contributions to $W^\pm W^\pm jj$, $W^\pm Zjj$, $W^\pm \gamma jj$ and $ZZjj$ production at hadron colliders, including the full leptonic decay of the massive vector bosons, have been calculated at NLO accuracy in QCD. The cross section calculations have been implemented into the Monte Carlo program VBFNLO, where special focus has been put on fast and stable numerical evaluation.

The details of the calculation have been presented in Chapter 3, focusing on the implementation of the virtual and real emission amplitudes as well as on the optimizations, that are used to obtain an efficient summation over Feynman diagrams, spin configurations, dipole subtraction terms and subprocesses. To guarantee the numerically stable evaluation of the virtual amplitudes, we have implemented a trigger system based on Ward identities, which allows to identify the occurrence of numerical instabilities. The corresponding contributions are then reevaluated using higher precision.
Furthermore, various checks to confirm the correctness of the code have been presented: The individual parts of the implementation have carefully been compared with an independent calculation, showing full agreement of both codes. At the level of the integrated cross sections, the Born as well as the real emission contributions have been compared with results generated with the program Sherpa. The full NLO cross sections of $W^\pm W^\pm jj$ and $W^\pm jj$ production have been compared with results obtained with the programs POWHEG-BOX and MCFM, respectively and agreement within the Monte Carlo errors has been found in both cases.

The phenomenology of the processes under consideration has been discussed in Chapter 4. LO results of W^+W^+jj production have been presented, taking into account the various EW- and QCD-induced contributions, as well as the interferences between these. We found that the interference effects account for less than 5% of the cross section in most phase space regions. The interference effects being small legitimates the separate calculation of the NLO corrections to the EW- and QCD-induced contributions of $VVjj$ production.
The effects of the NLO corrections to the QCD-induced contributions have been discussed in detail. There, a significant reduction of the scale dependence of the cross section predictions has been obtained for all processes: Varying the factorization and renormalization scales by a factor of two around a central scale at LO leads to theoretical uncertainties close to 50%, which are reduced to about 10-20% at NLO.
While in most phase space regions the corrections are of the order of 20% or less, we

observed large corrections by up to a factor of two in regions with large separation or invariant mass of the two tagging jets. In these regions, the invariant mass m_{jj} is much larger than the transverse momenta of the jets or the invariant masses of the electroweak bosons, which are all relevant scales of the processes. Hence, it is highly non-trivial to choose an appropriate value for the renormalization and factorization scale. Results using three different choices for the central values of these scales have been presented. We have shown that the large corrections are due to the large scale uncertainties at LO, while at NLO the results obtained with the different scale choices agree within the scale uncertainty of 10-20%.

The code for the calculation of QCD-induced $W^\pm W^\pm jj$, $W^\pm Zjj$ and $W^\pm \gamma jj$ production has been included in the latest release of the program VBFNLO [58], which allows to extend the results presented in this thesis to arbitrary phase space cuts and input parameters. The $ZZjj$ production will be added in an upcoming version. Furthermore, we plan to extend the implementation to include the $Z\gamma jj$, $\gamma\gamma jj$ and W^+W^-jj production.
With the QCD-induced processes being included in VBFNLO, this program now allows to calculate all contributions to $VVjj$ production – the EW contributions, which are sensitive to vector boson scattering and quartic gauge couplings, as well as the QCD-induced $VVjj$ production.

APPENDIX A

Color Algebra

A.1. Basics

Here, the color structures needed in this thesis are given. Before the discussion of the process specific ones, a summary of the basic relations, as they can be found in most text books about quantum field theory [59–61] and QCD [134, 135], are given. The color structure of QCD is determined by the properties of the symmetry group $SU(3)$, which is defined by the commutation relation

$$[t_r^a, t_r^b] = \mathrm{i} f^{abc} t_r^c, \tag{A.1}$$

where t_r are the generators of a representation r and f^{abc} are the structure constants of the group. In the following, the index r is neglected, if the fundamental representation is used. The adjoint representation A is given by the structure constants with $(t_A^a)^{bc} = -\mathrm{i} f^{abc}$. The quadratic Casimir invariants C_r are defined by

$$t_r^a t_r^a = C_r \, \mathbb{1}_r. \tag{A.2}$$

In the fundamental and adjoint representation, they are

$$C_F = \frac{N^2 - 1}{2N} = \frac{4}{3} \quad \text{and} \quad C_A = N = 3, \tag{A.3}$$

respectively. In addition, the Dynkin index T_R of the fundamental representation is defined by

$$\mathrm{Tr}(t^a t^b) = T_R \, \delta^{ab} = \frac{1}{2} \, \delta^{ab}. \tag{A.4}$$

The invariants are related by

$$T_r \, d_A = C_r \, d_r, \tag{A.5}$$

where C_r, T_r and d_r are the quadratic Casimir invariant Dynkin index and the dimension of representation r. $d_A = 8$ is the dimension of the adjoint representation.

All results presented in the following can be obtained using relations presented previously. Common structures appearing in the calculation are

$$\mathrm{i}f^{abc}t^b t^c = -\frac{C_A}{2}\,t^a = -\frac{3}{2}\,t^a \tag{A.6}$$

and

$$t^a t^b t^a = \left(C_F - \frac{C_A}{2}\right) t^b = -\frac{1}{6}\,t^b. \tag{A.7}$$

The last equation can be generalized for arbitrary expressions of the type $t^a \Gamma t^a$, where Γ represents a product of generators t^i in the fundamental representation. Knowing that Γ has to be a linear combination of the generators and the identity, it is clear, that the general expression has the form

$$t^a \Gamma t^a = x \cdot \Gamma + y \cdot \mathbb{1}. \tag{A.8}$$

Using the special case of Eq. (A.7) and taking the trace of Eq. (A.8), one obtains

$$t^a \Gamma t^a = \left(C_F - \frac{1}{2}C_A\right) \Gamma + \frac{1}{2N}\,C_A\,\mathrm{Tr}(\Gamma)\,\mathbb{1} = -\frac{1}{6}\Gamma + \frac{1}{2}\,\mathrm{Tr}(\Gamma)\,\mathbb{1}. \tag{A.9}$$

A further useful relation is the Fierz-identity,

$$t^a_{ki} t^a_{lj} = T_R \left(\delta_{li}\delta_{kj} - \frac{1}{N}\delta_{ki}\delta_{lj}\right). \tag{A.10}$$

A.2. Color Structure of the Born Amplitudes

At tree level, the color structures appearing in the amplitudes with two quarks and two gluons are

$$\mathcal{C}_1 = (t^b t^a)_{ji} \quad \text{and} \quad \mathcal{C}_2 = (t^a t^b)_{ji}, \tag{A.11}$$

and a further color structure appears in the virtual amplitudes:

$$\mathcal{C}_3 = \delta^{ab}\,\mathbb{1}_{ji}. \tag{A.12}$$

For the four quark amplitudes, the color structures are

$$\mathcal{C}_t = t^a_{ki} t^a_{lj} \quad \text{and} \quad \mathcal{C}_u = t^a_{kj} t^a_{li}, \tag{A.13}$$

corresponding to the t- and u-channel diagrams. At tree level, only one of these color structures appears, if there are no identical external quarks. Fig. A.1 diagrammatically shows the color structures $\mathcal{C}_1$ and $\mathcal{C}_t$.

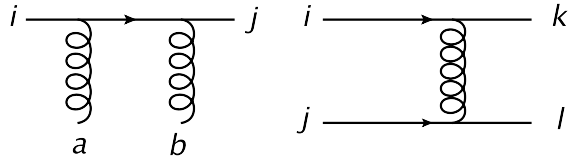

Figure A.1.: Color structures $\mathcal{C}_1$ and $\mathcal{C}_t$ for the two classes of subprocesses at tree level. The other color structures are obtained by interchanging the labels a and b in the two quark two gluon amplitude, or i and j in the four quark processes.

In the following, the bra-ket notation is used to represent the color structures and their complex conjugates. With this, the squared matrix elements can be written as

$$\langle \mathcal{C}_1|\mathcal{C}_1\rangle = \langle \mathcal{C}_2|\mathcal{C}_2\rangle = \mathrm{Tr}(t^a t^b t^b t^a) = N \cdot C_F^2 = \frac{16}{3} \tag{A.14}$$

$$\langle \mathcal{C}_1|\mathcal{C}_2\rangle = \langle \mathcal{C}_2|\mathcal{C}_1\rangle = \mathrm{Tr}(t^a t^b t^a t^b) = N \cdot C_F \cdot \left(C_F - \frac{1}{2}C_A\right) = -\frac{2}{3} \tag{A.15}$$

$$\langle \mathcal{C}_1|\mathcal{C}_3\rangle = \langle \mathcal{C}_3|\mathcal{C}_1\rangle = \langle \mathcal{C}_2|\mathcal{C}_3\rangle = \langle \mathcal{C}_3|\mathcal{C}_2\rangle = \delta^{ab}\,\mathrm{Tr}(t^a t^b) = N \cdot C_F = 4 \tag{A.16}$$

$$\langle \mathcal{C}_3|\mathcal{C}_3\rangle = \delta^{ab}\delta^{ab}\,\mathrm{Tr}(\mathbb{1}) = d_A \cdot N = 24 \tag{A.17}$$

and

$$\langle \mathcal{C}_t|\mathcal{C}_t\rangle = \langle \mathcal{C}_u|\mathcal{C}_u\rangle = \mathrm{Tr}(t^a t^b)\mathrm{Tr}(t^a t^b) = N \cdot T_R \cdot C_F = 2 \tag{A.18}$$

$$\langle \mathcal{C}_t|\mathcal{C}_u\rangle = \langle \mathcal{C}_u|\mathcal{C}_t\rangle = \mathrm{Tr}(t^a t^b t^a t^b) = N \cdot C_F \cdot \left(C_F - \frac{1}{2}C_A\right) = -\frac{2}{3}, \tag{A.19}$$

where $d_A = 8$ is the dimension of the adjoint representation. For the real emission amplitudes, an orthogonal color basis is constructed following the method of Ref. [76].

A.3. Color Correlated Born Matrix Elements

The evaluation of the subtraction terms as defined in Ref. [68] requires the evaluation of color correlated Born amplitudes

$$\langle \mathcal{C}|\mathbf{T}_x\mathbf{T}_y|\mathcal{C}\rangle, \tag{A.20}$$

where x and y each denote an external parton of the Born amplitude. For $x = y$, it is given by the squared Born amplitude multiplied with the quadratic Casimir invariant of the representation, under which the corresponding parton transforms. For the color structure as depicted in Fig. A.1, this is a factor of C_A for x being a or b and a factor of C_F in all other cases. Exploiting the color conservation

$$\mathbf{T}_x \cdot \sum_y \mathbf{T}_y|\mathcal{C}\rangle = 0, \tag{A.21}$$

there are only two more independent color correlated amplitudes for each subprocess.

For the subprocesses with two quarks and two gluons, one gets (using the external labels as in Fig. A.1)

$$\mathbf{T}_i\mathbf{T}_a|\mathcal{C}_1\rangle = -t^b t^{a'} t^c \cdot \mathrm{i}f_{aca'} = -\frac{3}{2}t^b t^a \tag{A.22}$$

$$\mathbf{T}_i\mathbf{T}_j|\mathcal{C}_1\rangle = -t^c t^b t^a t^c = \frac{1}{6}t^b t^a - \frac{1}{4}\delta^{ab}\mathbb{1}. \tag{A.23}$$

Therefore, the color correlated matrix elements read

$$\begin{pmatrix}\langle\mathcal{C}_1|\\ \langle\mathcal{C}_2|\end{pmatrix}\mathbf{T}_i\mathbf{T}_a\begin{pmatrix}|\mathcal{C}_1\rangle & |\mathcal{C}_2\rangle\end{pmatrix} = \begin{pmatrix}1 & 1\\ 1 & -8\end{pmatrix} \tag{A.24}$$

and

$$\begin{pmatrix}\langle\mathcal{C}_1|\\ \langle\mathcal{C}_2|\end{pmatrix}\mathbf{T}_i\mathbf{T}_j\begin{pmatrix}|\mathcal{C}_1\rangle & |\mathcal{C}_2\rangle\end{pmatrix} = -\frac{1}{9}\begin{pmatrix}1 & 10\\ 10 & 1\end{pmatrix}. \tag{A.25}$$

Similarly, one obtains for the four quark subprocesses

$$\begin{pmatrix}\langle\mathcal{C}_t|\\ \langle\mathcal{C}_u|\end{pmatrix}\mathbf{T}_i\mathbf{T}_j\begin{pmatrix}|\mathcal{C}_t\rangle & |\mathcal{C}_u\rangle\end{pmatrix} = \frac{1}{9}\begin{pmatrix}-6 & 10\\ 10 & -6\end{pmatrix} \tag{A.26}$$

and

$$\begin{pmatrix}\langle\mathcal{C}_t|\\ \langle\mathcal{C}_u|\end{pmatrix}\mathbf{T}_i\mathbf{T}_k\begin{pmatrix}|\mathcal{C}_t\rangle & |\mathcal{C}_u\rangle\end{pmatrix} = \frac{1}{9}\begin{pmatrix}3 & -1\\ -1 & 3\end{pmatrix}. \tag{A.27}$$

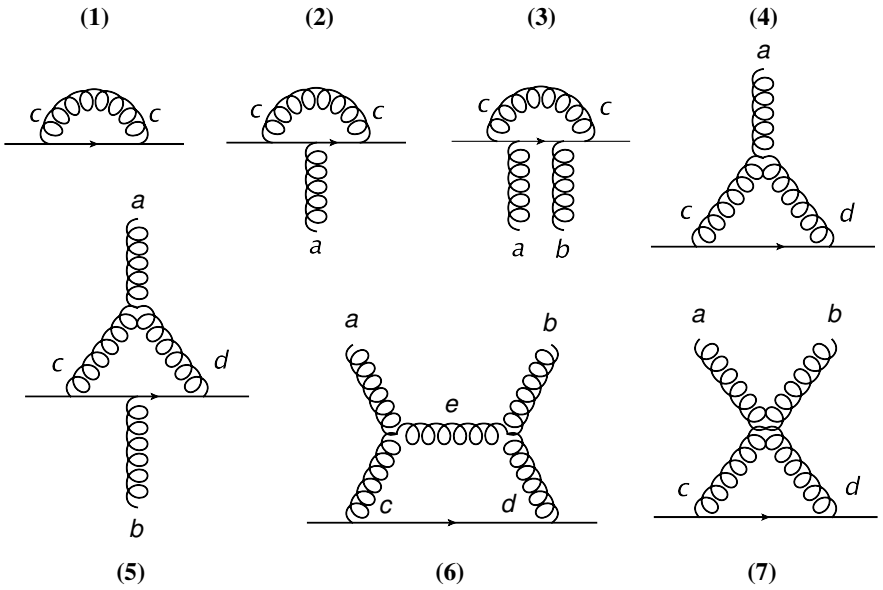

Figure A.2.: Color structures appearing in the virtual amplitude of the 2-quark-2gluon subprocesses.

A.4. Color Structures of the one-loop Amplitudes

Each diagram of the virtual amplitude can be assigned to one or more of the color structures defined in Section A.2. Fig. A.2 shows the basic one-loop diagrams neglecting colorless particles. The corresponding color factors are

$$\text{diagram (1):} \quad t^c t^c = C_F \, \mathbb{1} = \frac{4}{3} \, \mathbb{1} \tag{A.28}$$

$$\text{diagram (2):} \quad t^c t^a t^c = \left(C_F - \frac{C_A}{2} \right) t^a = -\frac{1}{6} \, t^a \tag{A.29}$$

$$\text{diagram (3):} \quad t^c t^b t^a t^c = \left(C_F - \frac{C_A}{2} \right) t^b t^a + \frac{C_A}{2N} \, T_R \, \delta^{ab} \, \mathbb{1} = -\frac{1}{6} \, t^b t^a + \frac{1}{4} \, \delta^{ab} \, \mathbb{1} \tag{A.30}$$

$$\text{diagram (4):} \quad \mathrm{i} f^{acd} t^d t^c = \frac{C_A}{2} \, t^a = \frac{3}{2} \, t^a \tag{A.31}$$

$$\text{diagram (5):} \quad \mathrm{i} f^{acd} t^d t^b t^c = -\frac{C_A}{2N} \, T_R \, \delta^{ab} \, \mathbb{1} = -\frac{1}{4} \, \delta^{ab} \, \mathbb{1} \tag{A.32}$$

$$\text{diagram (6):} \quad \mathrm{i} f^{ace} \mathrm{i} f^{edb} t^d t^c = \frac{C_A}{2} \, t^b t^a + \frac{C_A}{2N} \, T_R \, \delta^{ab} \, \mathbb{1} = \frac{3}{2} \, t^b t^a + \frac{1}{4} \, \delta^{ab} \, \mathbb{1} \tag{A.33}$$

Diagrams (1), (2) and (4) factorize against the corresponding Born diagram and therefore further gluons can easily be added to the quark line outside of the loop. Diagram (7) contains various combinations of the structure constants and the metric tensor. The individual terms can be easily obtained using Eqs. (A.31) and (A.33).

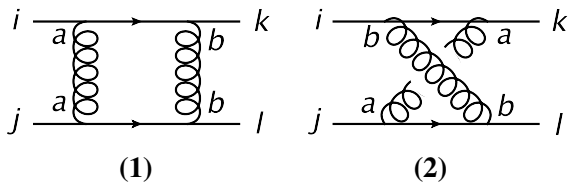

Figure A.3.: Color structures appearing in the virtual amplitude of the 4-quark subprocesses.

The color factors of the diagrams shown in Fig. A.3, which appear in the four-quark amplitudes are

$$\text{diagram (1):} \quad (t^b t^a)_{ki}(t^b t^a)_{lj} = \left(C_F - \frac{C_A}{2}\right) t^a_{ki} t^a_{lj} + T_R\, t^a_{kj} t^a_{li} = -\frac{1}{6}\,\mathcal{C}_t + \frac{1}{2}\,\mathcal{C}_u \quad \text{(A.34)}$$

$$\text{diagram (2):} \quad (t^a t^b)_{ki}(t^b t^a)_{lj} = C_F\, t^a_{ki} t^a_{lj} + T_R\, t^a_{kj} t^a_{li} = \frac{4}{3}\,\mathcal{C}_t + \frac{1}{2}\,\mathcal{C}_u. \quad \text{(A.35)}$$

APPENDIX B

Evaluation of Finite Collinear Terms

B.1. Plus- and β-distribution

The evaluation of the **K**-operator [68] requires the calculation of integrals involving the +-distribution, which is defined by

$$\int_0^1 \mathrm{d}x\, f(x)\,[g(x)]_+ = \int_0^1 \mathrm{d}x\, \left[f(x) - f(1)\right] g(x). \tag{B.1}$$

For the calculation presented in this thesis, the method of Refs. [34, 99] is used. With the same method, one can integrate contributions involving the β-description,

$$\int_0^1 \mathrm{d}x\, f(x)\,[g(x)]_\beta = \int_\beta^1 \mathrm{d}x\, \left[f(x) - f(1)\right] g(x), \tag{B.2}$$

which is a generalization of the +-distribution. It appears in the implementation of the α-parameter [103, 104], which is used to test the subtraction terms (see Section 3.5). The integrals appearing in the calculation are

$$\begin{aligned}\int_0^1 \mathrm{d}x\, f\left(\frac{z}{x}\right) \left(\frac{1}{1-x} \ln\left(\frac{1-x}{x}\right)\right)_+ \theta(x-z) = \\ \int_z^1 \frac{\mathrm{d}x}{x} \left(f\left(\frac{z}{x}\right) - x f(z)\right) \frac{\ln(1-x)}{1-x} - \int_z^1 \frac{\mathrm{d}x}{x} f\left(\frac{z}{x}\right) \frac{\ln x}{1-x} \\ + f(z) \left(\frac{1}{2}\ln^2(1-z) - \frac{\pi^2}{6}\right),\end{aligned} \tag{B.3}$$

$$\begin{aligned}\int_0^1 \mathrm{d}x\, f\left(\frac{z}{x}\right) \left(\frac{1+x^2}{1-x}\right)_+ \theta(x-z) = \\ \int_z^1 \frac{\mathrm{d}x}{x} \left(f\left(\frac{z}{x}\right) - x f(z)\right) \frac{2}{1-x} - \int_z^1 \frac{\mathrm{d}x}{x} f\left(\frac{z}{x}\right) (1+x) \\ + f(z) \left(2\ln(1-z) + \frac{3}{2}\right),\end{aligned} \tag{B.4}$$

$$\int_0^1 \mathrm{d}x\, f\left(\frac{z}{x}\right)\left(\frac{\ln(1-x)}{1-x}\right)_\beta \theta(x-z) =$$
$$\theta(x-\beta)\left[\int_z^1 \frac{\mathrm{d}x}{x}\left(f\left(\frac{z}{x}\right)-xf(z)\right)\frac{\ln(1-x)}{1-x} + f(z)\frac{1}{2}\left[\ln^2(1-z)-\ln^2(1-\beta)\right]\right], \quad \text{(B.5)}$$

$$\int_0^1 \mathrm{d}x\, f\left(\frac{z}{x}\right)\left(\frac{1}{1-x}\right)_\beta \theta(x-z) =$$
$$\theta(x-\beta)\left[\int_z^1 \frac{\mathrm{d}x}{x}\left(f\left(\frac{z}{x}\right)-xf(z)\right)\frac{1}{1-x} + f(z)\left[\ln(1-z)-\ln(1-\beta)\right]\right]. \quad \text{(B.6)}$$

Results for the missing integrals of the +-distribution can be obtained by setting $\beta = 0$.

B.2. Splitting Kernels and Insertion Operators

In the following, the results of Ref. [68] needed for the evaluation of the finite collinear terms are summarized and the coefficients appearing in Eq. (3.56) are listed. The basis for the dipole subtraction terms and their integrated counter parts are the Altarelli-Parisi splitting functions. After regularizing these by adding the corresponding virtual contribution, their four-dimensional contributions are

$$P^{qg}(x) = C_F\frac{1+(1-x)^2}{x}, \quad \text{(B.7)}$$
$$P^{gq}(x) = T_R\left[x^2+(1-x)^2\right], \quad \text{(B.8)}$$
$$P^{qq}(x) = C_F\left(\frac{1+x^2}{1-x}\right)_+ \quad \text{(B.9)}$$

and

$$P^{gg} = 2C_A\left[\left(\frac{1}{1-x}\right)_+ + \frac{1-x}{x} - 1 + x(1-x)\right] + \delta(1-x)\left(\frac{11}{6}C_A - \frac{2}{3}N_f T_R\right). \quad \text{(B.10)}$$

Their regular parts are

$$P^{qq}_{\mathrm{reg}}(x) = -C_F\,(1+x), \quad \text{(B.11)}$$
$$P^{gg}_{\mathrm{reg}}(x) = 2C_A\left[\frac{1-x}{x} - 1 + x(1-x)\right], \quad \text{(B.12)}$$
$$P^{aa'}_{\mathrm{reg}}(x) = P^{aa'}, \quad \text{if } a \neq a'. \quad \text{(B.13)}$$

Furthermore, the functions

$$\bar{K}^{qg}(x) = P^{qg}(x)\ln\frac{1-x}{x} + C_F\,x, \quad \text{(B.14)}$$
$$\bar{K}^{gq}(x) = P^{gq}(x)\ln\frac{1-x}{x} + T_R\,2x(1-x), \quad \text{(B.15)}$$
$$\begin{aligned}\bar{K}^{qq}(x) = {} & C_F\left[2\left(\frac{1}{1-x}\ln\frac{1-x}{x}\right)_+ - (1+x)\ln\frac{1-x}{x} + (1-x)\right] \\ & - \delta(1-x)\left[\left(\frac{50}{9}-\pi^2\right)C_A - \frac{16}{9}T_R N_f\right],\end{aligned} \quad \text{(B.16)}$$
$$\begin{aligned}\bar{K}^{gg}(x) = {} & 2C_A\left[\left(\frac{1}{1-x}\ln\frac{1-x}{x}\right)_+ - \left(\frac{1-x}{x} - 1 + x(1-x)\right)\ln\frac{1-x}{x} + (1-x)\right] \\ & - \delta(1-x)\left(5-\pi^2\right)C_F\end{aligned} \quad \text{(B.17)}$$

and

$$\widetilde{K}^{aa'}(x) = P_{\text{reg}}^{aa'}(x)\ln(1-x) + \delta^{aa'}\mathbf{T}_a^2\left[2\left(\frac{1}{1-x}\ln(1-x)\right)_+ - \frac{\pi^2}{3}\delta(1-x)\right] \tag{B.18}$$

are required.

In contrast to all other sections, the indices of the color operators $\mathbf{T}$ appearing in the following refer to the phase space positions. The particles involved in the initial state splitting are denoted as a and a' with the particles a' and b entering the matrix element of the hard process. The index i is used for summations over the final state partons, whereas the summation over I additionally includes the particle b.

With this conventions, the operator $\mathbf{P}$ can then be written as

$$\mathbf{P}^{aa'}(x, p_{a'}, \{p\}, \mu_F^2) = \frac{\alpha_s}{2\pi}P^{aa'}(x)\frac{1}{\mathbf{T}_{a'}^2}\sum_{I\neq a'}\mathbf{T}_I\mathbf{T}_{a'}\ln\frac{\mu_F^2}{2p_{a'}p_I}. \tag{B.19}$$

The $\mathbf{K}$ operator in the $\overline{\text{MS}}$ scheme is

$$\mathbf{K}^{aa'}(x) = \frac{\alpha_s}{2\pi}\left\{\bar{K}^{aa'}(x) + \delta^{aa'}\sum_i \mathbf{T}_i\mathbf{T}_a\frac{\gamma_i}{\mathbf{T}_i^2}\left[\left(\frac{1}{1-x}\right)_+ + \delta(1-x)\right] - \mathbf{T}_{a'}\mathbf{T}_b\frac{1}{\mathbf{T}_{a'}}\widetilde{K}^{aa'}\right\}, \tag{B.20}$$

where γ_i is determined by the parton type of particle i, with

$$\gamma_q = \frac{3}{2}C_F, \qquad \gamma_g = \frac{11}{6}C_A - \frac{2}{3}T_R N_f. \tag{B.21}$$

These operators can be plugged into Eq. (3.55). Using the integrals of the plus-distributions listed in Appendix B.1, one obtains the coefficients appearing in Eq. (3.56)

$$\begin{aligned}\mathcal{A}^q = {} & C_F\cdot\mathbb{1}\left[\ln^2(1-z) + \frac{2\pi^2}{3} - 5\right] - \frac{C_F}{C_A}\mathbf{T}_b\mathbf{T}_{a'}\left[\ln^2(1-z) - \frac{\pi^2}{3}\right] \\ & + \sum_i \gamma_i\frac{\mathbf{T}_i\mathbf{T}_{a'}}{\mathbf{T}_i^2}\left[\ln(1-z)+1\right] + \sum_{I\neq a'}\mathbf{T}_I\mathbf{T}_{a'}\left[2\ln(1-z)+\frac{3}{2}\right]\ln\frac{\mu_F^2}{2p_{a'}p_I},\end{aligned} \tag{B.22}$$

$$\begin{aligned}\mathcal{B}^q = {} & 2\left(C_F\,\mathbb{1} - \mathbf{T}_{a'}\mathbf{T}_b\right)\frac{\ln(1-x)}{1-x} + \sum_i\gamma_i\frac{\mathbf{T}_i\mathbf{T}_{a'}}{\mathbf{T}_i^2}\frac{1}{1-x} \\ & + \sum_{I\neq a'}\mathbf{T}_I\mathbf{T}_{a'}\frac{2}{1-x}\ln\frac{\mu_F^2}{2p_{a'}p_I},\end{aligned} \tag{B.23}$$

$$\begin{aligned}\mathcal{C}^{qq} = {} & C_F\,\mathbb{1}\left[-\frac{\ln x}{1-x} - (1+x)\ln\frac{1-x}{x} + 1 - x\right] + \mathbf{T}_b\mathbf{T}_{a'}(1+x)\ln(1-x) \\ & - \sum_{I\neq a'}\mathbf{T}_I\mathbf{T}_{a'}(1+x)\ln\frac{\mu_F^2}{2p_{a'}p_I},\end{aligned} \tag{B.24}$$

$$\begin{aligned}\mathcal{C}^{gq} = {} & T_R\,\mathbb{1}\left[\left(x^2-(1-x)^2\right)\ln\frac{1-x}{x} + 2x(1-x)\right] \\ & + \frac{T_R}{C_F}\left(x^2+(1-x)^2\right)\left[-\mathbf{T}_b\mathbf{T}_{a'}\ln(1-x) + \sum_{I\neq a'}\mathbf{T}_I\mathbf{T}_{a'}\ln\frac{\mu_F^2}{2p_{a'}p_I}\right],\end{aligned} \tag{B.25}$$

$$\begin{aligned}\mathcal{A}^g &= C_A \cdot \mathbb{1}\left[\ln^2(1-z)+\pi^2-\frac{50}{9}\right]+\frac{16}{9}T_R N_f \mathbb{1}+\mathbf{T}_b\mathbf{T}_{a'}\left[-\ln^2(1-z)+\frac{\pi^2}{3}\right]\\ &\quad+\sum_i \gamma_i \frac{\mathbf{T}_i\mathbf{T}_{a'}}{\mathbf{T}_i^2}\left[\ln(1-z)+1\right]\\ &\quad+\sum_{I\neq a'}\frac{\mathbf{T}_I\mathbf{T}_{a'}}{C_A}\left[2C_A\ln(1-z)+\frac{11}{6}C_A-\frac{2}{3}T_R N_f\right]\ln\frac{\mu_F^2}{2p_{a'}p_I},\end{aligned} \tag{B.26}$$

$$\begin{aligned}\mathcal{B}^g &= C_A\cdot\mathbb{1}\cdot 2\frac{\ln(1-x)}{1-x}+\sum_i\gamma_i\frac{\mathbf{T}_i\mathbf{T}_{a'}}{\mathbf{T}_i^2}\frac{1}{1-x}-\mathbf{T}_b\mathbf{T}_{a'}\cdot 2\frac{\ln(1-x)}{1-x}\\ &\quad+\sum_{I\neq a'}\mathbf{T}_I\mathbf{T}_{a'}\frac{2}{1-x}\ln\frac{\mu_F^2}{2p_{a'}p_I},\end{aligned} \tag{B.27}$$

$$\begin{aligned}\mathcal{C}^{gg} &= 2C_A\cdot\mathbb{1}\cdot\frac{\ln x}{1-x}\\ &\quad+2\left(\frac{1-x}{x}-1+x(1-x)\right)\left[\mathbb{1}\cdot C_A\,\ln\frac{1-x}{x}-\mathbf{T}_b\mathbf{T}_{a'}\ln(1-x)+\sum_{I\neq a'}\mathbf{T}_I\mathbf{T}_{a'}\ln\frac{\mu_F^2}{2p_{a'}p_I}\right],\end{aligned} \tag{B.28}$$

$$\mathcal{C}^{qg} = \mathbb{1}\cdot C_F\,x + C_F\frac{1+(1-x)^2}{x}\left[\mathbb{1}\cdot\ln\frac{1-x}{x}-\frac{\mathbf{T}_b\mathbf{T}_{a'}}{C_A}\ln(1-x)+\sum_{I\neq a'}\frac{\mathbf{T}_I\mathbf{T}_{a'}}{C_A}\ln\frac{\mu_F^2}{2p_{a'}p_I}\right]. \tag{B.29}$$

Bibliography

[1] **ATLAS Collaboration**, G. Aad *et al.*, *Observation of a new particle in the search for the Standard Model Higgs boson with the ATLAS detector at the LHC*. Phys.Lett. **B716** (2012) 1–29, arXiv:1207.7214 [hep-ex].

[2] **CMS Collaboration**, S. Chatrchyan *et al.*, *Observation of a new boson at a mass of 125 GeV with the CMS experiment at the LHC*. Phys.Lett. **B716** (2012) 30–61, arXiv:1207.7235 [hep-ex].

[3] A. Freitas and P. Schwaller, *Higgs CP Properties From Early LHC Data*. Phys.Rev. **D87** (2013) no. 5, 055014, arXiv:1211.1980 [hep-ph].

[4] **CMS Collaboration**, S. Chatrchyan *et al.*, *Measurement of the properties of a Higgs boson in the four-lepton final state*. Phys.Rev. **D89** (2014) 092007, arXiv:1312.5353 [hep-ex].

[5] **CMS Collaboration**, S. Chatrchyan *et al.*, *Study of the Mass and Spin-Parity of the Higgs Boson Candidate Via Its Decays to Z Boson Pairs*. Phys.Rev.Lett. **110** (2013) 081803, arXiv:1212.6639 [hep-ex].

[6] M. Gell-Mann, *A Schematic Model of Baryons and Mesons*. Phys.Lett. **8** (1964) 214–215.

[7] H. Fritzsch, M. Gell-Mann, and H. Leutwyler, *Advantages of the Color Octet Gluon Picture*. Phys.Lett. **B47** (1973) 365–368.

[8] D. J. Gross and F. Wilczek, *Ultraviolet Behavior of Nonabelian Gauge Theories*. Phys.Rev.Lett. **30** (1973) 1343–1346.
H. D. Politzer, *Reliable Perturbative Results for Strong Interactions?* Phys.Rev.Lett. **30** (1973) 1346–1349.

[9] S. Glashow, *Partial Symmetries of Weak Interactions*. Nucl.Phys. **22** (1961) 579–588.

[10] S. Weinberg, *A Model of Leptons*. Phys.Rev.Lett. **19** (1967) 1264–1266.

[11] A. Salam, *Weak and Electromagnetic Interactions*. Conf.Proc. **C680519** (1968) 367–377.

[12] P. W. Higgs, *Broken symmetries, massless particles and gauge fields*. Phys.Lett. **12** (1964) 132–133.
P. W. Higgs, *Broken Symmetries and the Masses of Gauge Bosons*. Phys.Rev.Lett. **13** (1964) 508–509.

[13] F. Englert and R. Brout, *Broken Symmetry and the Mass of Gauge Vector Mesons*. Phys.Rev.Lett. **13** (1964) 321–323.

[14] G. Guralnik, C. Hagen, and T. Kibble, *Global Conservation Laws and Massless Particles*. Phys.Rev.Lett. **13** (1964) 585–587.

[15] **UA1 Collaboration**, G. Arnison *et al.*, *Experimental Observation of Isolated Large Transverse Energy Electrons with Associated Missing Energy at* $s^{1/2} = 540$ *GeV*. Phys.Lett. **B122** (1983) 103–116.
UA2 Collaboration, M. Banner *et al.*, *Observation of Single Isolated Electrons of High Transverse Momentum in Events with Missing Transverse Energy at the CERN anti-p p Collider*. Phys.Lett. **B122** (1983) 476–485.

[16] **UA1 Collaboration**, G. Arnison *et al.*, *Experimental Observation of Lepton Pairs of Invariant Mass Around 95 GeV/*c^2 *at the CERN SPS Collider*. Phys.Lett. **B126** (1983) 398–410.
UA2 Collaboration, P. Bagnaia *et al.*, *Evidence for Z0* $\to e^+e^-$ *at the CERN anti-p p Collider*. Phys.Lett. **B129** (1983) 130–140.

[17] **CDF Collaboration**, F. Abe *et al.*, *Observation of top quark production in* $\bar{p}p$ *collisions*. Phys.Rev.Lett. **74** (1995) 2626–2631, arXiv:hep-ex/9503002 [hep-ex].
D0 Collaboration, S. Abachi *et al.*, *Observation of the top quark*. Phys.Rev.Lett. **74** (1995) 2632–2637, arXiv:hep-ex/9503003 [hep-ex].

[18] D. Hanneke, S. Fogwell, and G. Gabrielse, *New Measurement of the Electron Magnetic Moment and the Fine Structure Constant*. Phys.Rev.Lett. **100** (2008) 120801, arXiv:0801.1134 [physics.atom-ph].

[19] **LHCb collaboration**, R. Aaij *et al.*, *Measurement of the* $B_s^0 \to \mu^+\mu^-$ *branching fraction and search for* $B^0 \to \mu^+\mu^-$ *decays at the LHCb experiment*. Phys.Rev.Lett. **111** (2013) 101805, arXiv:1307.5024 [hep-ex].
CMS Collaboration, S. Chatrchyan *et al.*, *Measurement of the B(s) to mu+ mu- branching fraction and search for B0 to mu+ mu- with the CMS Experiment*. Phys.Rev.Lett. **111** (2013) 101804, arXiv:1307.5025 [hep-ex].

[20] **ATLAS Collaboration**, G. Aad *et al.*, *Evidence for Electroweak Production of* $W^\pm W^\pm jj$ *in pp Collisions at* $\sqrt{s} = 8$ *TeV with the ATLAS Detector*. arXiv:1405.6241 [hep-ex].

[21] C. Buttar, S. Dittmaier, V. Drollinger, S. Frixione, A. Nikitenko, *et al.*, *Les houches physics at TeV colliders 2005, standard model and Higgs working group: Summary report*. arXiv:hep-ph/0604120 [hep-ph].
SM and NLO Multileg Working Group, J. Andersen *et al.*, *The SM and NLO Multileg Working Group: Summary report*. arXiv:1003.1241 [hep-ph].

[22] B. Jager, C. Oleari, and D. Zeppenfeld, *Next-to-leading order QCD corrections to* W^+W^- *production via vector-boson fusion*. JHEP **0607** (2006) 015, arXiv:hep-ph/0603177 [hep-ph].

[23] B. Jager, C. Oleari, and D. Zeppenfeld, *Next-to-leading order QCD corrections to Z boson pair production via vector-boson fusion*. Phys.Rev. **D73** (2006) 113006, arXiv:hep-ph/0604200 [hep-ph].

[24] G. Bozzi, B. Jager, C. Oleari, and D. Zeppenfeld, *Next-to-leading order QCD corrections to W^+Z and W^-Z production via vector-boson fusion*. Phys.Rev. **D75** (2007) 073004, arXiv:hep-ph/0701105 [hep-ph].

[25] B. Jager, C. Oleari, and D. Zeppenfeld, *Next-to-leading order QCD corrections to W^+W^+jj and W^-W^-jj production via weak-boson fusion*. Phys.Rev. **D80** (2009) 034022, arXiv:arXiv:0907.0580 [hep-ph].

[26] A. Denner, L. Hosekova, and S. Kallweit, *NLO QCD corrections to W^+W^+jj production in vector-boson fusion at the LHC*. Phys.Rev. **D86** (2012) 114014, arXiv:arXiv:1209.2389 [hep-ph].

[27] F. Campanario, N. Kaiser, and D. Zeppenfeld, *$W\gamma$ production in vector boson fusion at NLO in QCD*. arXiv:arXiv:1309.7259 [hep-ph].

[28] V. Hankele and D. Zeppenfeld, *QCD corrections to hadronic WWZ production with leptonic decays*. Phys.Lett. **B661** (2008) 103–108, arXiv:arXiv:0712.3544 [hep-ph].

[29] F. Campanario, V. Hankele, C. Oleari, S. Prestel, and D. Zeppenfeld, *QCD corrections to charged triple vector boson production with leptonic decay*. Phys.Rev. **D78** (2008) 094012, arXiv:arXiv:0809.0790 [hep-ph].

[30] G. Bozzi, F. Campanario, V. Hankele, and D. Zeppenfeld, *NLO QCD corrections to $W^+W^-\gamma$ and $ZZ\gamma$ production with leptonic decays*. Phys.Rev. **D81** (2010) 094030, arXiv:arXiv:0911.0438 [hep-ph].

[31] G. Bozzi, F. Campanario, M. Rauch, H. Rzehak, and D. Zeppenfeld, *NLO QCD corrections to $W^\pm Z\gamma$ production with leptonic decays*. Phys.Lett. **B696** (2011) 380–385, arXiv:arXiv:1011.2206 [hep-ph].

[32] G. Bozzi, F. Campanario, M. Rauch, and D. Zeppenfeld, *$Z\gamma\gamma$ production with leptonic decays and triple photon production at NLO QCD*. Phys.Rev. **D84** (2011) 074028, arXiv:arXiv:1107.3149 [hep-ph].

[33] G. Bozzi, F. Campanario, M. Rauch, and D. Zeppenfeld, *$W^\pm\gamma\gamma$ production with leptonic decays at NLO QCD*. Phys.Rev. **D83** (2011) 114035, arXiv:arXiv:1103.4613 [hep-ph].

[34] V. Hankele, *NLO QCD corrections to tri-boson production in hadronic collisions*. PhD thesis, 2009. http://digbib.ubka.uni-karlsruhe.de/volltexte/1000010439.

[35] B. Feigl, *Electroweak Processes in the Standard Model and Beyond: Backgrounds to Higgs Physics and Semileptonic Decay Modes*. PhD thesis. http://digbib.ubka.uni-karlsruhe.de/volltexte/1000037298.

[36] A. Lazopoulos, K. Melnikov, and F. Petriello, *QCD corrections to tri-boson production*. Phys.Rev. **D76** (2007) 014001, arXiv:hep-ph/0703273 [hep-ph].

[37] T. Binoth, G. Ossola, C. Papadopoulos, and R. Pittau, *NLO QCD corrections to tri-boson production*. JHEP **0806** (2008) 082, arXiv:arXiv:0804.0350 [hep-ph].

[38] U. Baur, D. Wackeroth, and M. M. Weber, *Radiative corrections to W gamma gamma production at the LHC*. PoS **RADCOR2009** (2010) 067, arXiv:arXiv:1001.2688 [hep-ph].

[39] D. T. Nhung, L. D. Ninh, and M. M. Weber, *NLO corrections to WWZ production at the LHC*. arXiv:arXiv:1307.7403 [hep-ph].

[40] J. Butterworth, G. Dissertori, S. Dittmaier, D. de Florian, N. Glover, *et al.*, *Les Houches 2013: Physics at TeV Colliders: Standard Model Working Group Report*. arXiv:1405.1067 [hep-ph].

[41] T. Melia, K. Melnikov, R. Rontsch, and G. Zanderighi, *Next-to-leading order QCD predictions for W^+W^+jj production at the LHC*. JHEP **1012** (2010) 053, arXiv:arXiv:1007.5313 [hep-ph].

[42] T. Melia, P. Nason, R. Rontsch, and G. Zanderighi, *W^+W^+ plus dijet production in the POWHEGBOX*. Eur.Phys.J. **C71** (2011) 1670, arXiv:arXiv:1102.4846 [hep-ph].

[43] B. Jager and G. Zanderighi, *NLO corrections to electroweak and QCD production of W+W+ plus two jets in the POWHEGBOX*. JHEP **1111** (2011) 055, arXiv:arXiv:1108.0864 [hep-ph].

[44] F. Campanario, M. Kerner, L. D. Ninh, and D. Zeppenfeld, *Next-to-leading order QCD corrections to W^+W^+ and W^-W^- production in association with two jets*. Phys.Rev. **D89** (2014) 054009, arXiv:1311.6738 [hep-ph].

[45] T. Melia, K. Melnikov, R. Rontsch, and G. Zanderighi, *NLO QCD corrections for W^+W^- pair production in association with two jets at hadron colliders*. Phys.Rev. **D83** (2011) 114043, arXiv:arXiv:1104.2327 [hep-ph].

[46] N. Greiner, G. Heinrich, P. Mastrolia, G. Ossola, T. Reiter, *et al.*, *NLO QCD corrections to the production of W^+W^- plus two jets at the LHC*. Phys.Lett. **B713** (2012) 277–283, arXiv:arXiv:1202.6004 [hep-ph].

[47] F. Campanario, M. Kerner, L. D. Ninh, and D. Zeppenfeld, *WZ production in association with two jets at NLO in QCD*. Phys. Rev. Lett. **111** (2013) 052003, arXiv:arXiv:1305.1623 [hep-ph].

[48] F. Campanario, M. Kerner, L. D. Ninh, and D. Zeppenfeld, *Next-to-leading order QCD corrections to $W\gamma$ production in association with two jets*. Eur.Phys.J. **C74** (2014) 2882, arXiv:1402.0505 [hep-ph].

[49] F. Campanario, M. Kerner, L. D. Ninh, and D. Zeppenfeld, *Next-to-leading order QCD corrections to ZZ production in association with two jets*. arXiv:1405.3972 [hep-ph].

[50] T. Gehrmann, N. Greiner, and G. Heinrich, *Precise QCD predictions for the production of a photon pair in association with two jets*. arXiv:arXiv:1308.3660 [hep-ph].

[51] S. Badger, A. Guffanti, and V. Yundin, *Next-to-leading order QCD corrections to di-photon production in association with up to three jets at the Large Hadron Collider*. arXiv:1312.5927 [hep-ph].

[52] G. Cullen, N. Greiner, G. Heinrich, G. Luisoni, P. Mastrolia, *et al.*, *Automated One-Loop Calculations with GoSam*. Eur.Phys.J. **C72** (2012) 1889, arXiv:1111.2034 [hep-ph].
G. Cullen, H. van Deurzen, N. Greiner, G. Heinrich, G. Luisoni, *et al.*, *GoSam-2.0: a tool for automated one-loop calculations within the Standard Model and beyond*. arXiv:1404.7096 [hep-ph].

[53] F. Cascioli, P. Maierhofer, and S. Pozzorini, *Scattering Amplitudes with Open Loops.* Phys.Rev.Lett. **108** (2012) 111601, arXiv:1111.5206 [hep-ph].

[54] J. Alwall, R. Frederix, S. Frixione, V. Hirschi, F. Maltoni, *et al.*, *The automated computation of tree-level and next-to-leading order differential cross sections, and their matching to parton shower simulations.* arXiv:1405.0301 [hep-ph].

[55] T. Gleisberg, S. Hoeche, F. Krauss, M. Schonherr, S. Schumann, *et al.*, *Event generation with SHERPA 1.1.* JHEP **0902** (2009) 007, arXiv:0811.4622 [hep-ph].

[56] K. Arnold, M. Bahr, G. Bozzi, F. Campanario, C. Englert, *et al.*, *VBFNLO: A Parton level Monte Carlo for processes with electroweak bosons.* Comput.Phys.Commun. **180** (2009) 1661–1670, arXiv:arXiv:0811.4559 [hep-ph].

[57] K. Arnold, J. Bellm, G. Bozzi, M. Brieg, F. Campanario, *et al.*, *VBFNLO: A Parton Level Monte Carlo for Processes with Electroweak Bosons – Manual for Version 2.7.0.* arXiv:1107.4038 [hep-ph].

[58] J. Baglio, J. Bellm, F. Campanario, B. Feigl, J. Frank, *et al.*, *Release Note - VBFNLO 2.7.0.* arXiv:1404.3940 [hep-ph].

[59] M. E. Peskin and D. V. Schroeder, *An Introduction To Quantum Field Theory (Frontiers in Physics).* Westview Press, 1995.

[60] F. Mandl and G. Shaw, *Quantum field theory.* Wiley, 2009.

[61] T.-P. Cheng and L.-F. Li, *Gauge theory of elementary particle physics.* Oxford science publications. Clarendon Pr., Oxford, 1984.

[62] J. C. Collins, D. E. Soper, and G. F. Sterman, *Factorization of Hard Processes in QCD.* Adv.Ser.Direct.High Energy Phys. **5** (1988) 1–91, arXiv:hep-ph/0409313 [hep-ph].

[63] V. Gribov and L. Lipatov, *Deep inelastic e p scattering in perturbation theory.* Sov.J.Nucl.Phys. **15** (1972) 438–450.

[64] G. Altarelli and G. Parisi, *Asymptotic Freedom in Parton Language.* Nucl.Phys. **B126** (1977) 298.

[65] Y. L. Dokshitzer, *Calculation of the Structure Functions for Deep Inelastic Scattering and e+ e- Annihilation by Perturbation Theory in Quantum Chromodynamics.* Sov.Phys.JETP **46** (1977) 641–653.

[66] T. Kinoshita, *Mass singularities of Feynman amplitudes.* J.Math.Phys. **3** (1962) 650–677.

[67] T. Lee and M. Nauenberg, *Degenerate Systems and Mass Singularities.* Phys.Rev. **133** (1964) B1549–B1562.

[68] S. Catani and M. Seymour, *A General algorithm for calculating jet cross-sections in NLO QCD.* Nucl.Phys. **B485** (1997) 291–419, arXiv:hep-ph/9605323 [hep-ph].

[69] S. Dittmaier, S. Kallweit, and P. Uwer, *NLO QCD corrections to $pp/p\bar{p} \to WW + jet + X$ including leptonic W-boson decays.* Nucl.Phys. **B826** (2010) 18–70, arXiv:0908.4124 [hep-ph].

[70] D. Jones, *Two Loop Diagrams in Yang-Mills Theory*. Nucl.Phys. **B75** (1974) 531.
W. E. Caswell, *Asymptotic Behavior of Nonabelian Gauge Theories to Two Loop Order*. Phys.Rev.Lett. **33** (1974) 244.

[71] G. P. Lepage, *A New Algorithm for Adaptive Multidimensional Integration*. J.Comput.Phys. **27** (1978) 192.

[72] Z. Kunszt and Z. Trocsanyi, *QCD corrections to photon production in association with hadrons in e+ e- annihilation*. Nucl.Phys. **B394** (1993) 139–168, arXiv:hep-ph/9207232 [hep-ph].

[73] E. N. Glover and A. Morgan, *Measuring the photon fragmentation function at LEP*. Z.Phys. **C62** (1994) 311–322.

[74] **ALEPH Collaboration**, D. Buskulic *et al.*, *First measurement of the quark to photon fragmentation function*. Z.Phys. **C69** (1996) 365–378.

[75] S. Frixione, *Isolated photons in perturbative QCD*. Phys.Lett. **B429** (1998) 369–374, arXiv:hep-ph/9801442 [hep-ph].

[76] K. Hagiwara and D. Zeppenfeld, *Helicity Amplitudes for Heavy Lepton Production in e^+e^- Annihilation*. Nucl.Phys. **B274** (1986) 1–32.
K. Hagiwara and D. Zeppenfeld, *Amplitudes for Multiparton Processes Involving a Current at e^+e^-, $e^\pm p$, and Hadron Colliders*. Nucl.Phys. **B313** (1989) 560.

[77] H. Murayama, I. Watanabe, and K. Hagiwara, *HELAS: HELicity amplitude subroutines for Feynman diagram evaluations*.

[78] P. D. Draggiotis, R. H. Kleiss, and C. G. Papadopoulos, *Multijet production in hadron collisions*. Eur.Phys.J. **C24** (2002) 447–458, arXiv:hep-ph/0202201 [hep-ph].

[79] J. Alwall, P. Demin, S. de Visscher, R. Frederix, M. Herquet, *et al.*, *MadGraph/MadEvent v4: The New Web Generation*. JHEP **0709** (2007) 028, arXiv:0706.2334 [hep-ph].

[80] R. Frederix, T. Gehrmann, and N. Greiner, *Integrated dipoles with MadDipole in the MadGraph framework*. JHEP **1006** (2010) 086, arXiv:1004.2905 [hep-ph].

[81] F. Campanario, C. Englert, M. Rauch, and D. Zeppenfeld, *Precise predictions for $W\gamma\gamma$ +jet production at hadron colliders*. Phys.Lett. **B704** (2011) 515–519, arXiv:arXiv:1106.4009 [hep-ph].

[82] F. Campanario, Q. Li, M. Rauch, and M. Spira, *ZZ+jet production via gluon fusion at the LHC*. JHEP **1306** (2013) 069, arXiv:1211.5429 [hep-ph].

[83] F. Campanario, *Towards $pp \to VVjj$ at NLO QCD: Bosonic contributions to triple vector boson production plus jet*. JHEP **1110** (2011) 070, arXiv:arXiv:1105.0920 [hep-ph].

[84] R. Mertig, M. Bohm, and A. Denner, *FEYN CALC: Computer algebraic calculation of Feynman amplitudes*. Comput.Phys.Commun. **64** (1991) 345–359.

[85] M. S. Chanowitz, M. Furman, and I. Hinchliffe, *The Axial Current in Dimensional Regularization*. Nucl.Phys. **B159** (1979) 225.

[86] G. 't Hooft and M. Veltman, *Regularization and Renormalization of Gauge Fields*. Nucl.Phys. **B44** (1972) 189–213.

[87] Z. Bern and D. A. Kosower, *The Computation of loop amplitudes in gauge theories.* Nucl.Phys. **B379** (1992) 451–561.

[88] A. Signer and D. Stockinger, *Using Dimensional Reduction for Hadronic Collisions.* Nucl.Phys. **B808** (2009) 88–120, arXiv:0807.4424 [hep-ph].

[89] A. Bredenstein, A. Denner, S. Dittmaier, and S. Pozzorini, *NLO QCD corrections to $t\bar{t}b\bar{b}$ production at the LHC: 1. Quark-antiquark annihilation.* JHEP **0808** (2008) 108, arXiv:0807.1248 [hep-ph].

[90] G. Passarino and M. Veltman, *One Loop Corrections for e^+e^- Annihilation Into $\mu^+\mu^-$ in the Weinberg Model.* Nucl.Phys. **B160** (1979) 151.

[91] A. Denner and S. Dittmaier, *Reduction schemes for one-loop tensor integrals.* Nucl.Phys. **B734** (2006) 62–115, arXiv:hep-ph/0509141 [hep-ph].

[92] G. 't Hooft and M. Veltman, *Scalar One Loop Integrals.* Nucl.Phys. **B153** (1979) 365–401.

[93] Z. Bern, L. J. Dixon, and D. A. Kosower, *Dimensionally regulated pentagon integrals.* Nucl.Phys. **B412** (1994) 751–816, arXiv:hep-ph/9306240 [hep-ph].

[94] S. Dittmaier, *Separation of soft and collinear singularities from one loop N point integrals.* Nucl.Phys. **B675** (2003) 447–466, arXiv:hep-ph/0308246 [hep-ph].

[95] D. T. Nhung and L. D. Ninh, *D0C : A code to calculate scalar one-loop four-point integrals with complex masses.* Comput. Phys. Commun. **180** (2009) 2258–2267, arXiv:arXiv:0902.0325 [hep-ph].

[96] A. Denner and S. Dittmaier, *Scalar one-loop 4-point integrals.* Nucl.Phys. **B844** (2011) 199–242, arXiv:arXiv:1005.2076 [hep-ph].

[97] A. Sirlin, *A Class of Useful Identities Involving Correlated Direct Products of γ Matrices.* Nucl.Phys. **B192** (1981) 93.

[98] T. M. Figy, *NLO QCD corrections to the jet activity in Higgs boson production via vector-boson fusion.* PhD thesis, 2006.

[99] C. Englert, *Next-to-Leading Order Corrections to $W\gamma$+jet and WZ+jet Production at Hadron Colliders.* PhD thesis, 2010. http://digbib.ubka.uni-karlsruhe.de/volltexte/1000017450.

[100] T. Hahn, *Generating Feynman diagrams and amplitudes with FeynArts 3.* Comput.Phys.Commun. **140** (2001) 418–431, arXiv:hep-ph/0012260 [hep-ph].

[101] T. Hahn and M. Perez-Victoria, *Automatized one-loop calculations in four and D dimensions.* Comput. Phys. Commun. **118** (1999) 153–165, arXiv:hep-ph/9807565.

[102] Duc Ninh LE, *private communication.*

[103] Z. Nagy and Z. Trocsanyi, *Next-to-leading order calculation of four jet observables in electron positron annihilation.* Phys.Rev. **D59** (1999) 014020, arXiv:hep-ph/9806317 [hep-ph].

[104] Z. Nagy, *Next-to-leading order calculation of three jet observables in hadron hadron collision.* Phys.Rev. **D68** (2003) 094002, arXiv:hep-ph/0307268 [hep-ph].

[105] T. Gleisberg and S. Hoeche, *Comix, a new matrix element generator*. JHEP **0812** (2008) 039, arXiv:0808.3674 [hep-ph].

[106] J. M. Campbell and R. K. Ellis, *Next-to-leading order corrections to W^+ 2 jet and Z^+ 2 jet production at hadron colliders*. Phys.Rev. **D65** (2002) 113007, arXiv:hep-ph/0202176 [hep-ph].

[107] J. M. Campbell, R. K. Ellis, and D. L. Rainwater, *Next-to-leading order QCD predictions for W + 2 jet and Z + 2 jet production at the CERN LHC*. Phys.Rev. **D68** (2003) 094021, arXiv:hep-ph/0308195 [hep-ph].

[108] S. Alioli, P. Nason, C. Oleari, and E. Re, *A general framework for implementing NLO calculations in shower Monte Carlo programs: the POWHEG BOX*. JHEP **1006** (2010) 043, arXiv:arXiv:1002.2581 [hep-ph].

[109] D. L. Rainwater and D. Zeppenfeld, *Observing $H \to W^*W^* \to e^\pm\mu \mp \not{p}_T$ in weak boson fusion with dual forward jet tagging at the CERN LHC*. Phys.Rev. **D60** (1999) 113004, arXiv:hep-ph/9906218 [hep-ph].

[110] V. D. Barger, R. Phillips, and D. Zeppenfeld, *Mini - jet veto: A Tool for the heavy Higgs search at the LHC*. Phys.Lett. **B346** (1995) 106–114, arXiv:hep-ph/9412276 [hep-ph].

[111] M. Kerner, *Zentraler Jet Veto bei der Produktion von WZ + 2 Jets am LHC*. diploma thesis, 2011. http://www.itp.kit.edu/prep/diploma/PSFiles/Diplom_Kerner.pdf.

[112] C. Englert, B. Jager, M. Worek, and D. Zeppenfeld, *Observing Strongly Interacting Vector Boson Systems at the CERN Large Hadron Collider*. Phys.Rev. **D80** (2009) 035027, arXiv:arXiv:0810.4861 [hep-ph].

[113] **ATLAS Collaboration**, G. Aad *et al.*, *Search for supersymmetry at sqrt(s)=8 TeV in final states with jets and two same-sign leptons or three leptons with the ATLAS detector*. arXiv:1404.2500 [hep-ex].

[114] B. Humpert, *ARE THERE MULTI - QUARK INTERACTIONS?* Phys.Lett. **B131** (1983) 461.

[115] A. Kulesza and W. J. Stirling, *Like sign W boson production at the LHC as a probe of double parton scattering*. Phys.Lett. **B475** (2000) 168–175, arXiv:hep-ph/9912232 [hep-ph].

[116] E. Maina, *Multiple Parton Interactions in Z+4j, $W^\pm W^\pm$ + 0/2j and W^+W^- + 2j production at the LHC*. JHEP **0909** (2009) 081, arXiv:0909.1586 [hep-ph].

[117] J. R. Gaunt, C.-H. Kom, A. Kulesza, and W. J. Stirling, *Same-sign W pair production as a probe of double parton scattering at the LHC*. Eur.Phys.J. **C69** (2010) 53–65, arXiv:1003.3953 [hep-ph].

[118] M. Cacciari, G. P. Salam, and G. Soyez, *The Anti-k_T jet clustering algorithm*. JHEP **0804** (2008) 063, arXiv:arXiv:0802.1189 [hep-ph].

[119] A. Martin, W. Stirling, R. Thorne, and G. Watt, *Parton distributions for the LHC*. Eur.Phys.J. **C63** (2009) 189–285, arXiv:arXiv:0901.0002 [hep-ph].

[120] J. Ohnemus and J. Owens, *An Order-α_s calculation of hadronic ZZ production.* Phys.Rev. **D43** (1991) 3626–3639.
J. Ohnemus, *An Order-α_s calculation of hadronic $W^{\pm}Z$ production.* Phys.Rev. **D44** (1991) 3477–3489.
J. Ohnemus, *An Order-α_s calculation of hadronic W^-W^+ production.* Phys.Rev. **D44** (1991) 1403–1414.
B. Mele, P. Nason, and G. Ridolfi, *QCD radiative corrections to Z boson pair production in hadronic collisions.* Nucl.Phys. **B357** (1991) 409–438.
S. Frixione, P. Nason, and G. Ridolfi, *Strong corrections to W Z production at hadron colliders.* Nucl.Phys. **B383** (1992) 3–44.
S. Frixione, *A Next-to-leading order calculation of the cross-section for the production of W^+W^- pairs in hadronic collisions.* Nucl.Phys. **B410** (1993) 280–324.

[121] L. J. Dixon, Z. Kunszt, and A. Signer, *Vector boson pair production in hadronic collisions at order α_s : Lepton correlations and anomalous couplings.* Phys.Rev. **D60** (1999) 114037, arXiv:hep-ph/9907305 [hep-ph].

[122] J. Baglio, L. D. Ninh, and M. M. Weber, *Massive gauge boson pair production at the LHC: a next-to-leading order story.* Phys.Rev. **D88** (2013) 113005, arXiv:1307.4331.

[123] A. Djouadi, M. Spira, and P. Zerwas, *Production of Higgs bosons in proton colliders: QCD corrections.* Phys.Lett. **B264** (1991) 440–446.

[124] S. Dawson, *Radiative corrections to Higgs boson production.* Nucl.Phys. **B359** (1991) 283–300.

[125] S. D. Ellis, Z. Kunszt, and D. E. Soper, *Two jet production in hadron collisions at order α_s^3 in QCD.* Phys.Rev.Lett. **69** (1992) 1496–1499.

[126] **ATLAS Collaboration**, G. Aad *et al.*, *Inclusive search for same-sign dilepton signatures in pp collisions at $\sqrt{s} = 7$ TeV with the ATLAS detector.* JHEP **1110** (2011) 107, arXiv:1108.0366 [hep-ex].

[127] **CMS Collaboration**, C. Collaboration, *Search for supersymmetry in events with same-sign dileptons.*

[128] M. Rubin, G. P. Salam, and S. Sapeta, *Giant QCD K-factors beyond NLO.* JHEP **1009** (2010) 084, arXiv:1006.2144 [hep-ph].

[129] J. R. Andersen, T. Hapola, and J. M. Smillie, *W Plus Multiple Jets at the LHC with High Energy Jets.* JHEP **1209** (2012) 047, arXiv:1206.6763 [hep-ph].

[130] F. Campanario and S. Sapeta, *WZ production beyond NLO for high-pT observables.* Phys.Lett. **B718** (2012) 100–104, arXiv:1209.4595 [hep-ph].

[131] F. Campanario, M. Rauch, and S. Sapeta, *W^+W^- production at high transverse momenta beyond NLO.* Nucl.Phys. **B879** (2014) 65–79, arXiv:1309.7293 [hep-ph].

[132] **New Physics Working Group**, G. Brooijmans *et al.*, *New Physics at the LHC. A Les Houches Report: Physics at TeV Colliders 2009 - New Physics Working Group.* arXiv:1005.1229 [hep-ph].

[133] U. Baur, T. Han, and J. Ohnemus, *QCD corrections to hadronic $W\gamma$ production with nonstandard $WW\gamma$ couplings.* Phys.Rev. **D48** (1993) 5140–5161, arXiv:hep-ph/9305314 [hep-ph].

[134] R. K. Ellis, W. J. Stirling, and B. Webber, *QCD and collider physics*. Cambridge Univ. Press, 2003.

[135] G. Dissertori, I. G. Knowles, and M. Schmelling, *Quantum chromodynamics : high energy experiments and theory*. Clarendon Press, 2003.

[136] D. Binosi and L. Theussl, *JaxoDraw: A Graphical user interface for drawing Feynman diagrams*. Comput.Phys.Commun. **161** (2004) 76–86, arXiv:hep-ph/0309015 [hep-ph].

[137] D. Binosi, J. Collins, C. Kaufhold, and L. Theussl, *JaxoDraw: A Graphical user interface for drawing Feynman diagrams. Version 2.0 release notes*. Comput.Phys.Commun. **180** (2009) 1709–1715, arXiv:0811.4113 [hep-ph].

Acknowledgment

First of all, I want to thank Prof. Dr. Dieter Zeppenfeld for accepting me as a PhD student and giving me the opportunity to work on this interesting topic. I am very grateful for many useful discussions, which allowed me to benefit from his great knowledge of particle physics and collider phenomenology.

I thank Prof. Dr. Matthias Steinhauser for agreeing to be the second referee of this thesis.

I am very grateful to Francisco Campanario and Duc Ninh Le for the fruitful collaboration, numerous explanations and useful discussions. I appreciate Michael Rauch's assent to use the implementation of $gg \to ZZj$ in this work.

For the proofreading of this thesis, I want to thank Francisco Campanario, Duc Ninh Le, Christian Reuschle and Robin Roth.

I also want to thank the members of the ITP for the pleasant atmosphere at the institute. Special thanks go to my officemates Ken Arnold, Francisco Campanario, Ramona Gröber, Christian Reuschle and Juraj Streicher for the friendly atmosphere with many interesting discussions.

The financial support by the "strukturiertes Promotionskolleg in KCETA" as well as by the Graduiertenkolleg 1694 "Elementarteilchenphysik bei höchster Energie und höchster Präzision" is greatly acknowledged.

Finally, I wish to thank my family for their support.